

3D pore-scale simulation of the fluid flow through the electrodes of High Temperature Polymeric Electrolyte Fuel Cell

*Original*

3D pore-scale simulation of the fluid flow through the electrodes of High Temperature Polymeric Electrolyte Fuel Cell / Salomov, Uktam. - (2014). [10.6092/polito/porto/2546336]

*Availability:*

This version is available at: 11583/2546336 since:

*Publisher:*

Politecnico di Torino

*Published*

DOI:10.6092/polito/porto/2546336

*Terms of use:*

Altro tipo di accesso

This article is made available under terms and conditions as specified in the corresponding bibliographic description in the repository

*Publisher copyright*

(Article begins on next page)

# 3D pore-scale simulation of the fluid flow through the electrodes of High Temperature Polymeric Electrolyte Fuel Cell



UKTAM SALOMOV RAHIMOVICH

Department of Energy  
Politecnico di Torino

A thesis submitted for the degree of  
*Doctor in Energetics*

2014

Supervisors: Prof. Pietro Asinari, Dr. Eliodoro Chiavazzo

## Abstract

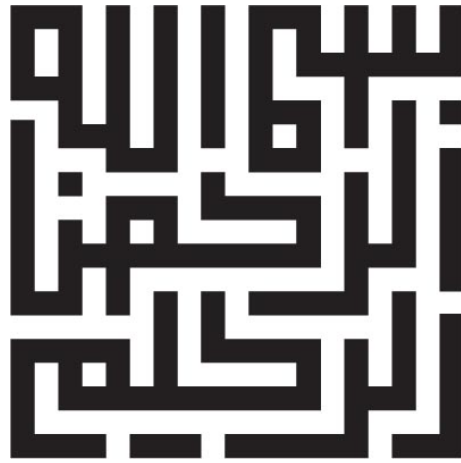
Fuel cells and hydrogen are two key components for building a competitive, secure, and sustainable clean energy economy, due to possibility to convert diverse fuels directly into electrical power without combustion and a carbon-free fuel that can be produced from renewable resources. However, to become competitive in a market, fuel cells should overcome the issues by improvements in durability and performance as well as reductions in manufacturing cost. Recent advances in fuel cell technology has been made by development of the high temperature (HT) polymeric electrolyte membrane (PEM) fuel cells (FC). Owing to combination of the advantages of two types of fuel cells, namely polymeric electrolyte membrane and phosphoric acid, it is considered as one of the best technological solutions.

Further improvements cannot be done without deep understanding of the major causes and underlying physico-chemical phenomena for specific degradation mechanisms of different compartments of HT-PEMFC, especially porous electrodes, which are the most vulnerable part prone to degradation processes, and predicting the impact of these degradation effects. Modeling can provide insight into the mechanisms that lead to irreversible or reversible performance loss and the relation between these mechanisms and the operating conditions, based on the changes in materials properties that can be observed. Moreover, another important issue of modeling is understanding the interaction between different specific membrane degradation mechanisms and their complex and mixed effects due to their simultaneously occurrence in real fuel cell operation, which requires multi-scale analysis of undergoing phenomena.

This work represents a step towards reliable algorithms for reconstructing micro-morphology of electrode materials of high-temperature proton-exchange membrane fuel cells and for performing pore-scale simulations of fluid flow (including rarefaction effects). In particular, we developed a deterministic model for a woven gas diffusion layer (GDL) and the stochastic model for a non-woven GDL and a carbon-supported catalyst layer (CL) based on clusterization of carbon particles. We verified that both developed models accurately recover the experimental values of permeability, without any special ad-hoc tuning. Moreover, we investigated the effect of catalyst particle distributions inside the CL on the degree of clusterization and on the microscopic fluid flow, which is relevant for degradation modeling (e.g. loss of phosphoric acid). The three-dimensional pore-scale simulations of fluid flow for the direct numerical calculation of macroscopic transport parameters, like permeability, were performed by the Lattice Boltzmann Method (LBM).

Within framework of this thesis, we investigate how distribution of catalyst (Pt) particles can affect gas dynamics, electro-chemistry and consequently performance in high temperature proton exchange membrane fuel cells. Optimal distribution of catalyst can be used as a mitigation strategy for phosphoric acid loss and crossover of reagents through membrane. The main idea is that one of the reasons of degradation is the gas dynamic pulling stress at the interface between the catalyst and the membrane. This stress can be highly reduced by tuning the main morphological parameters of the catalyst layer, like distribution of catalyst particles and clusterization. We have performed direct numerical pore-scale simulations of the gas flow through catalyst layer for different distributions of catalyst particles, in order to minimize this stress and hence to improve durability. The results of pore-scale simulation for exponential decay distribution show more than one order of magnitude reduction of the pulling stress, compared to the homogeneous (conventional) distribution.

Moreover, a simplified three-dimensional macroscopic model of the membrane electrode assembly (MEA) with catalyst layer comprised of three sublayers with different catalyst loadings, has been developed to analyze how the proposed mitigation strategy affects the polarization curve and hence the performance. This macroscopic model presents 67% reduction in pulling stress for feasible mitigation strategy, at the price of only 9.3% reduction in efficiency at high current densities.



*To Muhammad and Ibrohim ...*

---

## LIST OF PAPERS

Present thesis to a large degree is based on the following papers, conference contributions of author:

- Uktam R. Salomov, Eliodoro Chiavazzo, Pietro Asinari  
Pore-scale modeling of fluid flow through gas diffusion and catalyst layers for high temperature proton exchange membrane (HT-PEM) fuel cells, *Computers and Mathematics with Applications*, vol. 67, pp. 393-411. - ISSN 0898-1221.
- Uktam R. Salomov, Eliodoro Chiavazzo, Pietro Asinari  
Gas-dynamic and electro-chemical optimization of catalyst layers in high temperature polymeric electrolyte membrane fuel cells, *submitted to Journal of Power Sources*, 2014.
- U. Salomov, P. Asinari  
Multi-scale modelling to boost fuel cell performance: From pore-scale simulations to better efficiency and durability, *In: European Hydrogen Energy Conference*, Seville, Spain, March 2014.
- Y. Nedellec, A. Kreisz, N. Donzel, J. Roziere, D. J. Jones, A. Morin, C. Nayoze, F. Alcaide Monterrubio, M. Smit, P. Asinari, U. Salomov, A. Piu  
Novel materials for a HT-PEMFC stack for operation as automotive range extender, *In: European Hydrogen Energy Conference*, Seville, Spain, March 2014
- Uktam Salomov, Pietro Asinari  
Multi-scale modeling to boost fuel cell performance: From pore-scale simulations to better efficiency and durability, *In: ECoMaTech - European Conference on Materials and Technologies for Sustainable Growth*, Bled, Slovenia, 19th-21st, September 2013.
- Uktam Salomov, Pietro Asinari  
Pore-scale simulation of fluid flow through the electrodes of high temperature PEMFC using Lattice Boltzmann Method. *In: The 10th International*

---

*Conference for Mesoscopic Methods in Engineering and Science (ICMMES 2013)*, Oxford, UK, 22nd-26th, July 2013.



## Acknowledgements

Foremost, I would like to address my sincere gratitude to my supervisor Prof. Pietro Asinari for his never-ending support throughout the whole PhD period, especially in ruling out the misunderstandings at the beginning. For his patience during long discussions, which encouraged popup of the new ideas, sometimes really crazy, for his enthusiasm and positive motivation, and of course enormous knowledge of the study subject. Also, I owe my deepest gratitude to Dr. Eliodoro Chiavazzo, my supplementary supervisor, for scrutinizing the papers as well as this thesis that led to improving them significantly.

I would like to show my greatest appreciation to my colleagues from the Multi-Scale ModeLing Laboratory (SMaLL) group, Matteo, Luigi, Annalisa, as well as the alumni Fabio for an exciting and enjoyable working atmosphere. My great pleasure to name the members of the Synergies of Thermo-chemical and Electro-chemical Power Systems (STEPS) group, prof. Massimo Santarelli, Pierluigi, Andrea, Marta, Gustavo, Domenico, DDavide, PDavide for useful discussions, invaluable comments and daily out-of-work activities. Thanks to dozens of people at the Politecnico di Torino, mentioning them will never be enough to express my gratitude.

My sincere thanks also goes to Dr. Deborah Jones and Dr. Yannig Nedellec for providing me the opportunity of visiting their group at the Institut Charles Gerhardt, Université de Montpellier 2 (UM2).

The financial supports through the Exchange Programm of Turin Polytechnic University in Tashkent, the FP-7 **ARTEMIS** '*Automotive Range extender with high TEMperature Improved pemfc meas and Stacks*' and the PRIN '*Microscopic modeling and degradation analysis*

*of the membrane electrode assembly (MEA) in high temperature PEM fuel cells'* projects are gratefully acknowledged.

Last but not least, my heartfelt appreciation goes to my parents for their continuous moral and practical support, my family, especially my wife for her love and enormous patience during the long periods of my being far away from home.

---

# Contents

<b>List of Figures</b>	<b><a href="#">xi</a></b>
<b>List of Tables</b>	<b><a href="#">xvii</a></b>
<b>Glossary</b>	<b><a href="#">xix</a></b>
<b>1 Introduction</b>	<b><a href="#">1</a></b>
1.1 Polymeric electrolyte membrane fuel cell . . . . .	<a href="#">1</a>
1.2 Fuel cell chemical reactions and components . . . . .	<a href="#">2</a>
1.3 Degradation . . . . .	<a href="#">6</a>
1.4 Modeling . . . . .	<a href="#">8</a>
1.5 Methodology . . . . .	<a href="#">10</a>
1.6 Scope of this thesis . . . . .	<a href="#">11</a>
<b>2 Lattice Boltzmann Method</b>	<b><a href="#">15</a></b>
2.1 Introduction . . . . .	<a href="#">15</a>
2.2 From Boltzmann Equation to Lattice Boltzmann Equation . . . . .	<a href="#">16</a>
2.3 Boundary Conditions . . . . .	<a href="#">21</a>
2.4 Unit conversion . . . . .	<a href="#">23</a>
2.5 Flow through array of body-centered cubic spheres . . . . .	<a href="#">24</a>
2.6 Conclusion . . . . .	<a href="#">29</a>
<b>3 Morphological model</b>	<b><a href="#">31</a></b>
3.1 Introduction . . . . .	<a href="#">31</a>
3.2 Reconstruction of fiber-based gas diffusion layer . . . . .	<a href="#">34</a>
3.2.1 Stochastic non-woven structure . . . . .	<a href="#">34</a>

## CONTENTS

---

3.2.2	Regular woven structure . . . . .	40
3.3	Reconstruction of carbon-supported catalyst layer . . . . .	43
3.4	Direct numerical simulation of permeability . . . . .	47
3.4.1	Results of fluid simulation for gas diffusion layer . . . . .	48
3.4.2	Results of fluid simulation for catalyst layer . . . . .	49
3.5	Gas rarefaction effect . . . . .	50
3.5.1	Flow regimes . . . . .	51
3.5.2	Estimation of maximum gas rarefaction effect on permeability	54
3.6	Conclusion . . . . .	55
<b>4</b>	<b>Degradation of the High Temperature Polymeric Electrolyte Fuel Cells</b>	<b>57</b>
4.1	Introduction . . . . .	57
4.1.1	Degradation of membrane . . . . .	59
4.1.2	Degradation of electrodes . . . . .	60
4.2	Phosphoric acid loss . . . . .	62
4.3	Mitigation . . . . .	64
4.3.1	Effects of platinum particle distribution in catalyst layer .	64
4.3.2	Innovative idea . . . . .	67
4.3.3	Theoretical estimation for pulling stress . . . . .	68
4.4	Conclusion . . . . .	72
<b>5</b>	<b>Simulation setups &amp; results</b>	<b>73</b>
5.1	Three-dimensional pore-scale model of a catalyst layer . . . . .	73
5.2	Three-dimensional macroscopic model of a single membrane electrode assembly . . . . .	76
5.2.1	Electrochemical reactions . . . . .	78
5.2.2	Governing equations . . . . .	79
5.3	Simulation results and discussion . . . . .	81
5.3.1	Results for flow velocity . . . . .	82
5.3.2	Single membrane electrode assembly performance simulation	90
5.4	Conclusion . . . . .	92
<b>6</b>	<b>Conclusions &amp; Perspectives</b>	<b>95</b>

References	99
------------	----

## CONTENTS

---

# List of Figures

1.1	Schematic diagram of PEMFC. . . . .	2
1.2	A polarization curve with the three major overpotential regions. .	4
1.3	Scanning Electron Microscope image of the membrane electrode assembly of state of the art high temperature polymeric electrolyte fuel cell, <i>Celtec – P1000</i> by BASF <sup>®</sup> . This image is provided by the research center ENEA Brasimone in framework of the national PRIN 'Microscopic modeling and degradation analysis of the membrane electrode assembly (MEA) in high temperature PEM fuel cells' project (see also [16]). . . . .	5
1.4	Pie diagram of the cost percentage of different compartments of polymer electrolyte membrane fuel cell with nobel (Pt) metal catalyst. . . . .	6
2.1	Geometrical representation of lattice (a) $D2Q9$ (b) $D3Q19$ . . . . .	19
2.2	Bounce back scheme for $D2Q9$ lattice. Unknown population distribution functions inside a wall are depicted by red color. . . . .	21
2.3	Periodic unit cell of an infinite array of body-centered cubic spheres.	25
2.4	Permeability as a function of porosity given by Eq. (2.26). Inset: The results of different numerical methods for porosity $\varepsilon = 0.32$ . .	28



3.1	Micro-morphology of a HTPEM fuel cell ( <i>Celtec-P1000</i> by BASF <sup>®</sup> ) by Scanning Electron Microscope (SEM) imaging. These images are acquired purposely for the present work in the research center ENEA Brasimone in the framework of the national PRIN 'Microscopic modeling and degradation analysis of the membrane electrode assembly (MEA) in high temperature PEM fuel cells' project (see also [16]). . . . .	32
3.2	SEM images of (a-c) a planar with different magnification level; (d) a vertical; cross section of Freudenberg GDL by Freudenberg <sup>®</sup> Non-Wovens Technical Division, Lowell, MA. These SEM images are obtained in the Institut Charles Gerhardt Universite Montpellier II in the framework of the European FP-7 project 'Automotive Range extender with high TEMperature Improved pemfc meas and Stacks' (ARTEMIS). . . . .	36
3.3	(a) a planar; (b) a vertical; view of the micro-morphology of GDL reconstructed using the proposed algorithm. . . . .	39
3.4	SEM images of (a-c) a vertical with different magnification level; (d) a planar; cross section of AvCarb 1071 woven gas diffusion layer. These images are acquired purposely for the present work in the research center ENEA Brasimone in the framework of the national PRIN 'Microscopic modeling and degradation analysis of the membrane electrode assembly (MEA) in high temperature PEM fuel cells' project (see also [16]). . . . .	40
3.5	Schematic representation of the reconstruction steps for a woven fiber-based gas diffusion layer [16]. . . . .	41
3.6	Geometry of the reconstruction and streamlines of fluid flow through a woven GDL. In order to simplify the visualization, the used parameters, namely $N_A = 6$ , $N_B = 4$ , $N_x = 180$ and $N_y = N_z = 240$ , are coarser than those required by computing permeability [16]. . . . .	44

3.7	Micro-structure of the carbon supported catalyst layer Vulcan XC-72. These SEM images, except (d), are obtained in the Institut Charles Gerhardt Universite Montpellier II in the framework of the European FP-7 project 'Automotive Range extender with high TEMperature Improved pemfc meas and Stacks' (ARTEMIS). . . .	44
3.8	The geometry and flow streamlines through reconstructed CL porous medium: (a)-(b) the results of the straightforward algorithm; (c)-(d) the results of clusterization one for $L_{cluster}^{av} = 350 \text{ nm}$ [16]. . . .	51
4.1	Schematic representation of connection between main degradation processes and fuel cell operating conditions for transportation application. . . . .	59
4.2	Two considered (a-b) locations and (c-d) corresponding deposition distribution of Pt particles inside the catalyst layer. . . . .	65
4.3	(a-b) Pt deposition and flow streamlines (c-d) slices of corresponding flow velocity . . . . .	66
4.4	Considered elementary volume. . . . .	69
4.5	Periodicity. . . . .	70
5.1	Left-hand side: Two representative cubic configurations of the CL with (a) homogeneous and (b) exponential decay catalyst particle distributions. Right-hand side: Probability distribution of catalyst particles along $x, y, z$ -directions. Plots are reported in terms of the following dimensionless coordinates: $x_{cl} = x/l_{CL}$ , $y_{cl} = y/l_{CL}$ and $z_{cl} = z/l_{CL}$ . . . . .	74
5.2	Single MEA geometry representations with the compartment names.	77
5.3	Mesh configuration of three-dimensional single MEA. (a) coarser mesh for the gas channels and the GDLs, while (b) finer mesh for the CLs are required. . . . .	83

- 5.4 Profile of the  $x$ -component velocity averaged over the plane orthogonal to main flow direction ( $x$ ). Symbols represent the result of pore-scale simulations for the homogeneous catalyst particle distribution. The straight line is the theoretical prediction. The abscissa indicates the dimensionless spatial coordinate  $x_{cl} = x/l_{CL}$  across the CL, where the interface GDL/CL is located at  $x_{cl} = 0$ , while the interface CL/membrane is at  $x_{cl} = 1$ . . . . . 84
- 5.5 Left ((a) and (c)): Results of pore-scale simulations for  $\delta p = 3.0 \times 10^{-4} l.u.$  Right ((b) and (d)): Results of macroscopic model simulations with  $V_{cell} = 0.6V$ . (a): Average flow pressure (curved line) and imposed pressure at the catalyst nodes (straight line as dictated by (5.18)). (c): Difference of the above two pressures. (b): Electric and electrolyte potentials across the catalyst layer. (d): Electrode reaction current density inside the catalyst layer. Abscissas indicate the dimensionless spatial coordinate  $x_{cl} = x/l_{CL}$  across the CL, where the interface GDL/CL is located at  $x_{cl} = 0$ , while the interface CL/membrane is at  $x_{cl} = 1$ . . . . . 85
- 5.6  $x$ -component velocity as derived by the macroscopic model at  $V_{cell} = 0.6V$  with homogeneous catalyst loading: (a) on the middle plane of the MEA ( $y = l_{CELL}/2$ ); (b) along the center line ( $z = (h_{RIB} + h_{CH})/2$ ) of the above plane. Inset: zoom of the velocity profile within the CL. . . . . 86
- 5.7 Velocity profiles corresponding to homogeneous and exponential decay catalyst particle distributions. (a): results of the pore-scale model with  $\delta p = 3.0 \times 10^{-4} l.u.$  (b): results of the macroscopic model with a current density  $j = 0.6A/m^2$ . Slopes of those profiles are also reported by straight lines. . . . . 87
- 5.8 A cubic representative configuration of the CL of a HT-PEM fuel cell is reconstructed by the method proposed in Section 3. Fluid flow streamlines through the reconstructed CL porous medium (semi-transparent) corresponding to homogeneous distribution (a) and exponential decay profile (b). Streamline colors indicate the velocity magnitude in dimensionless lattice Boltzmann units. . . . 89

5.9	Polarization curves for three different configurations of catalyst particles distribution. The values of cell voltage at $j = 0.6 \text{ A/m}^2$ current density are presented in Table 5.4. . . . .	92
-----	--	----

## LIST OF FIGURES

---

# List of Tables

1.1	MEA compartments, typical geometrical and transport parameters of HTPEM fuel cell. . . . .	5
2.1	Input parameters and obtained numerical results by ANSYS Fluent <sup>®</sup> , PALABOS, literature [65] and Kozeny-Carman model. The PALABOS results are reported first in dimensionless units (the so-called lattice units <i>l.u.</i> , see [41]) and then in physical units. . . . .	27
2.2	Dependence of permeability on resolution. The results are reported first in dimensionless units (the so-called lattice units <i>l.u.</i> , see [41]) and then in physical units. . . . .	29
3.1	Typical transport parameters of the GDL and CL of a HT-PEM fuel cell from literature. . . . .	33
3.2	Technical data for different GDL by Freudenberg <sup>®</sup> . . . . .	35
3.3	Numerical results of permeability of GDL ( <i>l.u.</i> stands for lattice units, see [41]). . . . .	48
3.4	Sensitivity of permeability on the cluster size of carbon particles in CL ( <i>l.u.</i> stands for lattice units, see [41]). . . . .	50
3.5	Estimation of mean free paths for the gases involved in electrochemical reactions of the HT-PEM. Operating temperature $T = 423\text{ K}$ and pressure $P = 101325\text{ Pa}$ . Data taken from Ref. [90]. . .	53
3.6	Estimate of rarefaction effects for hydrogen gas flow, with mean free path $\lambda = 270\text{ nm}$ (see Table 3.5), through GDL and CL. . . .	55
4.1	Simulation results and comparison. . . . .	67

## LIST OF TABLES

---

5.1	Setup of the simulations for pore-scale modeling. The parameters of Lattice Boltzmann method and the results are reported in dimensionless units (the so-called lattice units l.u., see [41]) . . . .	76
5.2	Parameters of geometry of the macroscopic model of single MEA in Fig. 5.2. . . . .	77
5.3	Physical parameters and operating conditions. . . . .	91
5.4	Results of macroscopic modeling simulation. Cell voltage at $j = 0.6 \text{ A/m}^2$ current density for different cases of catalyst loading distribution. . . . .	93

# Glossary

<b>BB</b>	bounce back
<b>BC</b>	boundary condition
<b>BCC</b>	body-centered cubic
<b>BGK</b>	Bhatnagar-Gross-Krook
<b>CFD</b>	computational fluid dynamics
<b>CL</b>	catalyst layer
<b>FC</b>	fuel cell
<b>GDL</b>	gas diffusion Layer
<b>HOR</b>	hydrogen oxydation reaction
<b>HT</b>	high temperature
<b>HT-PEM</b>	high temperature polymeric electrolyte membrane
<b>HT-PEMFC</b>	high temperature polymeric electrolyte membrane fuel cell
<b>KC</b>	Kozeny-Carman
<b>LBM</b>	lattice Boltzmann method
<b>LGA</b>	Lattice gas automata
<b>LT</b>	low temperature
<b>LTPEMFC</b>	low temperature polymeric electrolyte membrane fuel cell
<b>MEA</b>	membrane electrode assembly
<b>MRT</b>	multiple-relaxation-time
<b>ORR</b>	oxygen reduction reaction
<b>PA</b>	phosphoric acid
<b>PBI</b>	polybenzimidazole
<b>PEFC</b>	polymeric electrolyte fuel cell
<b>PEM</b>	proton-exchange membrane/polymeric electrolyte membrane
<b>PEMFC</b>	proton-exchange membrane fuel cell
<b>Pt</b>	platinum
<b>TPB</b>	three-phase-boundary





# 1

## Introduction

*“Begin at the beginning, the King  
said gravely, “and go on till you  
come to the end: then stop.”*

---

— Lewis Carroll, Alice in  
Wonderland

### 1.1 Polymeric electrolyte membrane fuel cell

Fuel cells have been the subject of a large amount of research owing to consider them as an environmentally friendly, clean energy source. Especially, fuel cells based on proton-exchange membranes (PEM) and fueled by hydrogen and air have many attractive features, including high power density, rapid start-up and high efficiency [1]. Moreover, the wide range of possible applications including small-scale power sources, automobiles, homes and portable devices makes this kind system very fascinating from commercial point of view.

A next generation of PEMFCs at elevated temperature (above 100 °C) has been designed to solve the problems of the low temperature (LT) counterpart, by system simplification, reduction of the production cost, and improvement of the efficiency [2, 3, 4]. As a result, high tolerance of platinum based catalyst to fuel CO impurity (up to 2% at 180°C in the absence of humidification [5, 6]) has been achieved for the high temperature (HT) PEMFCs. Moreover, chemically coupled with acids membranes (polymer electrolyte) show enhanced ionic conductivity [7].

## 1. INTRODUCTION

---

To this end, significant amount of investigations on phosphoric-acid (PA)-doped polybenzimidazole(PBI)-based HT-PEMFCs membranes have been carried out with regards to the membrane conductivity and heat resistance [8, 9]. In [10, 11] authors addressed to the power generation capability issue. It was established that the highest fuel cell performance can be obtained at the operating temperature close to 200 °C [12]. Durability exceeding ten thousands has been reported by several research groups [13, 14] which might be considered to be closest to commercialization.

### 1.2 Fuel cell chemical reactions and components

Fuel cells are the electrochemical devices which convert chemical energy to electrical energy. A typical schematic diagram of a polymer electrolyte membrane fuel cell together with two main electrochemical reactions during fuel cell operation, hydrogen oxidation (HOR) in anode catalyst layer and oxygen reduction (ORR) in cathode catalyst layer, are illustrated in Fig. 1.1. Hydrogen-rich fuel,

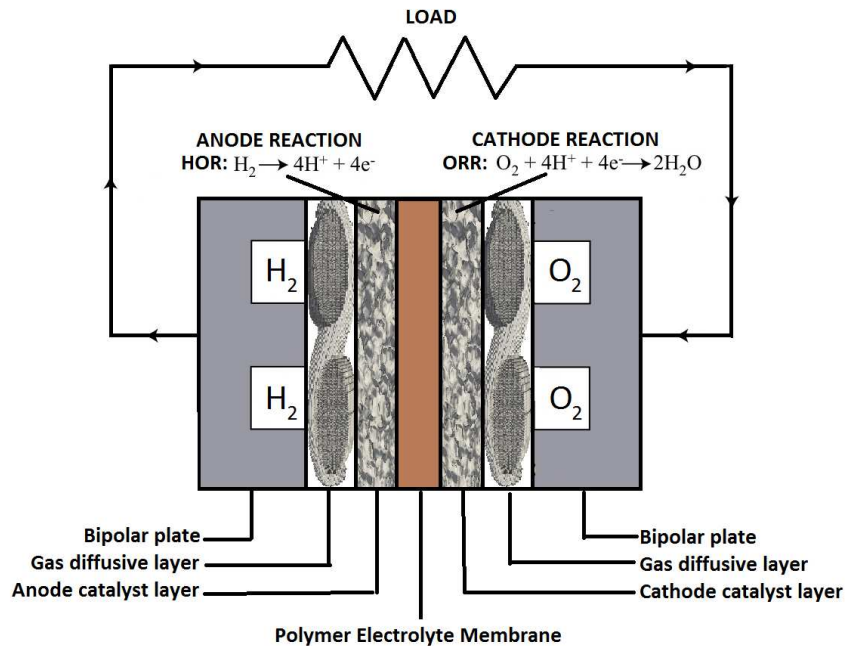
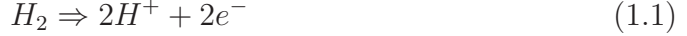


Figure 1.1: Schematic diagram of PEMFC.

basically hydrogen, is fed in to the anode channel (voids of bipolar plates (BP)), where part of this travels across the gas diffusion layer (GDL) and reach reaction sites at the cathalyst layer (CL). At the anode catalyst layer hydrogen oxidation reaction occurs according to:



Electrons produced within this reaction migrate across the cell through following pathway: carbon support particles embedded in the anode catalyst layer, carbon fibers of GDLs, current collector, external circuit or load, cathode catalyst layer. By contrary, produced protons migrate shorter path, across the membrane from the anode towards the cathode catalyst layer.

On the other hand, the cathode channels are fed by air. At the cathode, oxygen reacts together with the protons produced at cathode side and forms water according to:



Hence, the overall reaction or whole cell reaction is summation of two half-cell reactions occurring separately at the electrodes.

The performance delivered by the fuel cell is the current times the residual cell voltage. The efficiency of the electrochemical energy conversion is directly related to the cell potential. At the rest or open circuit voltage (OCV) condition this potential is maximum and equal to the equilibrium potential, about  $E_{th} = 1.2V$  for  $H_2/O_2$  system (dotted line in Fig. 1.2). During the operation the fuel cell produces current leading to decrease of this potential from the equilibrium potential, so-called the overpotential  $\eta$ .

A polarization curve is the most popular technique used for characterization of overall fuel cell performance, which represents a plot of cell potential versus current density under fixed operating conditions. Normally, it can be reproduced by gradually increasing current and obtaining the result for cell voltage or vice-versa. Generally, this polarization curve can be divided into three main regions as depicted in Fig. 1.2. The first region, an abrupt drop in potential, corresponds to the kinetic losses due to sluggish kinetics of the ORR at cathode side. It is also known as an activation polarization at low current densities. As the current is increased up to moderate values, Ohmic losses become a factor in linearly lowering

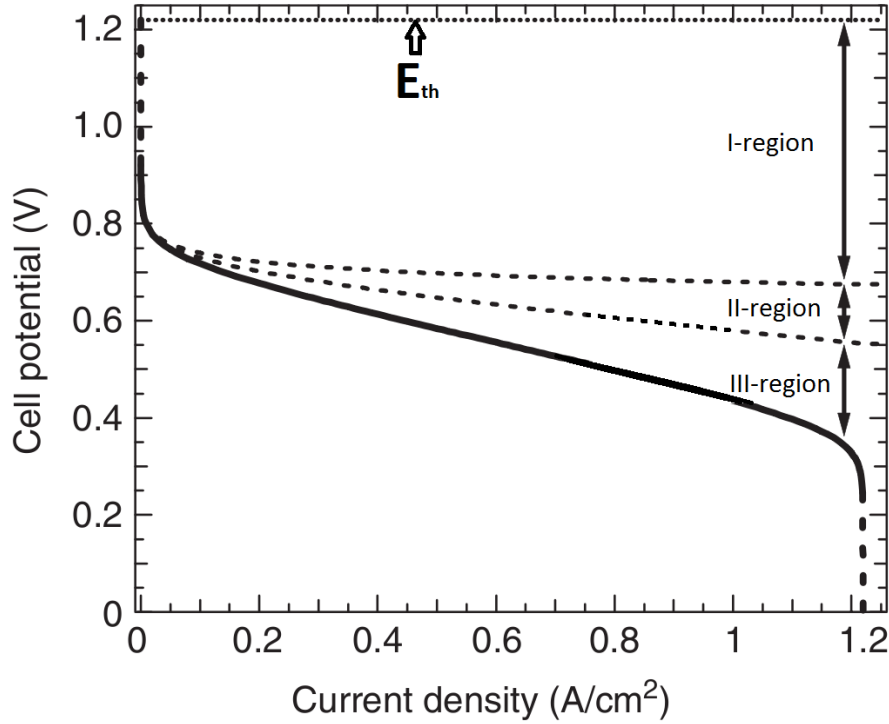


**Figure 1.2:** A polarization curve with the three major overpotential regions.

the overall cell potential (II-region). These Ohmic losses are mainly from ionic conductivity decrease in the polymer membrane and the electrodes. Due to high electronic conductivity of BP electronic losses is thought to be negligible. The third region accounts high current density, where mass transport overpotential becomes significant. At this value of current density fuel cell potential quickly tends to zero voltage.

One of the typical high temperature polymeric electrolyte fuel cells, state of the art *Celtec-P1000* manufactured by BASF<sup>®</sup>, is considered within this thesis. Its key components, so-called membrane-electrode assembly (MEA), is depicted in Fig. 1.3. A membrane electrode assembly is made as follows (according to Ref. [15]): On top of a carbon fiber-based (woven or non-woven) gas diffusion layer (for example, a woven AvCarb<sup>®</sup> 1071 or non-woven Toray Graphite Paper, TGP-120, BASF<sup>®</sup> Fuel Cell, Inc.), a micro-porous layer is deposited, consisting of Vulcan XC-72R Carbon Black (Cabot Corp.) and polytetrafluoroethylene (Teflon Emulsion Solution, Electrochem Inc.). Moreover, a catalytic layer is also

deposited, composed of Platinum (Pt) catalyst on carbon (C) support (Pt on Vulcan XC-72R Carbon Black, ETEK-Inc.). The system consists of an impermeable (for the gases) electrolyte at the center, with two very thin regions at the upper and bottom sides of the electrolyte, sandwiched between the electrolyte and the electrodes. These regions are the carbon supported Pt catalyst layers, which hold together the membrane and two (anode and cathode) woven gas diffusion layers. The most significant geometrical parameters of the system are given in Table 1.1.

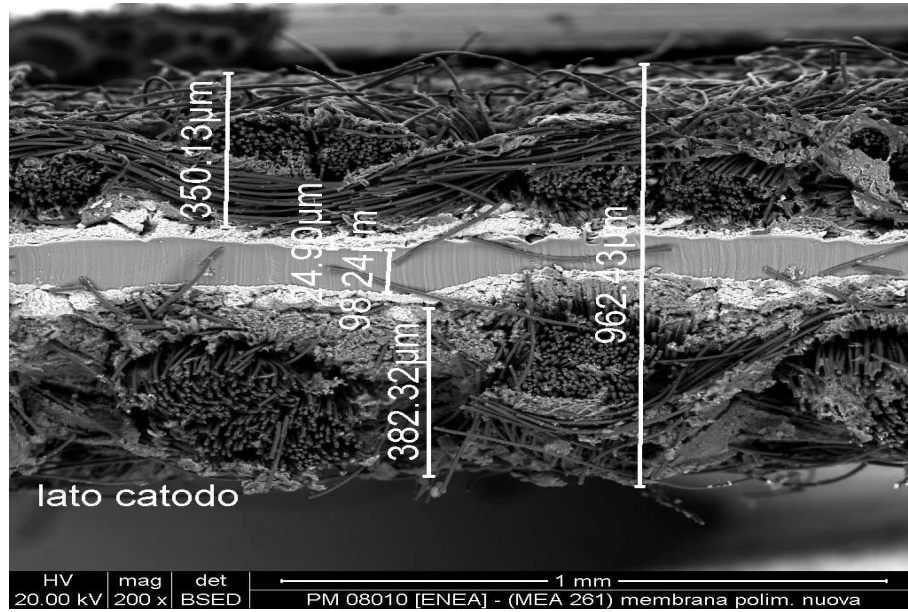


**Figure 1.3:** Scanning Electron Microscope image of the membrane electrode assembly of state of the art high temperature polymeric electrolyte fuel cell, *Celtec – P1000* by BASF®. This image is provided by the research center ENEA Brasimone in framework of the national PRIN 'Microscopic modeling and degradation analysis of the membrane electrode assembly (MEA) in high temperature PEM fuel cells' project (see also [16]).

**Table 1.1:** MEA compartments, typical geometrical and transport parameters of HTPEM fuel cell.

MEA compartment	Thickness	Porosity/Permeability
GDL	100 – 400 $\mu m$	$0.5-0.6/10^{-12} m^2$
CL	2 – 20 $\mu m$	$0.4-0.5/10^{-13} m^2$
Membrane	20 – 100 $\mu m$	-/-

### 1.3 Degradation

Among the major technological issues limiting the widespread adoption and successful commercialization of polymer-electrolyte fuel cells, especially for automotive applications, are those of lifetime or durability, under various operating conditions, and cost. In Fig. 1.4 the pie diagram of weight on the whole cost

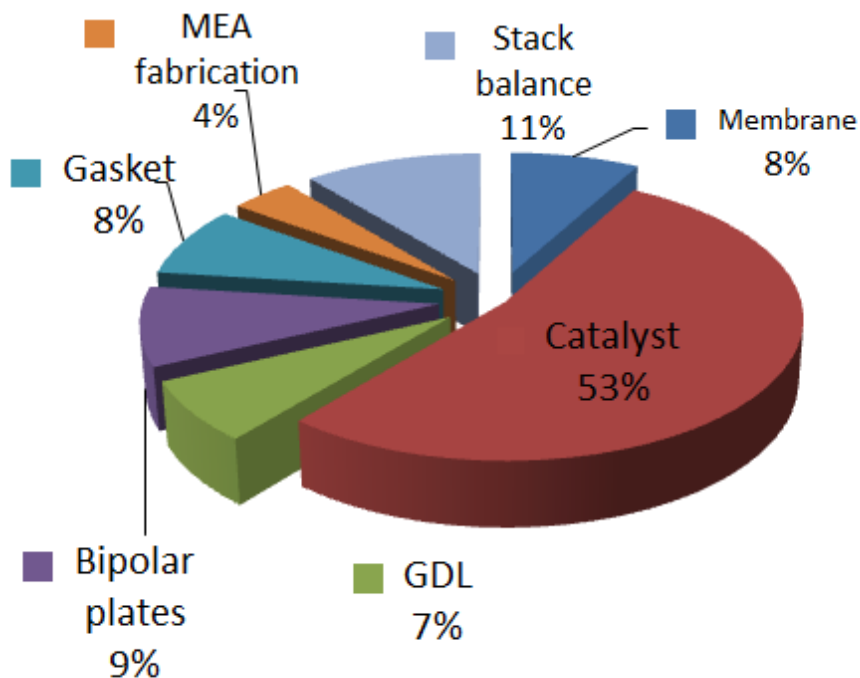


**Figure 1.4:** Pie diagram of the cost percentage of different compartments of polymer electrolyte membrane fuel cell with nobel (Pt) metal catalyst.

of different fuel cell compartments is shown. As can be seen, more than 60% of the cost comes from the electrodes of PEMFC due to high price of nobel metal (platinum) used as a catalyst. It should be noted that the electrodes are the most vulnerable fuel cell parts prone to the degradation processes. Especially for automotive applications, the degradation phenomena of the membrane electrode assembly (MEA) plays a key role [17]. The number of installed units around the world continues to increase and dominates the pre-markets, but the present lifetime requirements for fuel cells cannot be guaranteed. This fact stimulates research for a more comprehensive knowledge of the material aging mechanisms.

Although, all parts of a hydrogen fuel cell are subject to degradation processes, the membrane electrode assembly (MEA) is commonly considered as the heart of the system. Generally, MEA consists with the following compartments: electrodes (gas diffusive layers (GDL), catalyst layers (CL)) and membrane. Especially, the degradation of the noble metal catalysts in the MEAs at the so-called three-phase-boundary (TPB) [18, 19, 20] is a key factor directly influencing the durability of the fuel cells. There are two main degradation modes related to the membrane, which are (a) membrane thinning leading to a possible pinhole formation and (b) increased fuel crossover and loss of fuel efficiency by acid evaporation [21]. It was shown that phosphoric acid loss from the membrane is insignificant at 160 °C [21, 22]. Excessive compression of MEA causes membrane creep and thinning manifested by gas crossover increase and by the decrease of the membrane resistance.

Unfortunately, the failure mechanism of membranes in the PEM fuel cell is not well understood [1]. First of all, at higher operating temperature, membrane dehydration and the subsequent decrease in proton conductivity is a significant issue. Membrane dehydration results in shrinking, cracking [23] and finally in a loss of mechanical stability with increasing temperature. Moreover, an extensive morphological relaxation occurs above the glass transition temperature of a polymer (130-160 °C for a dry membrane and 80-100 °C for a hydrated membrane), which may have an adverse effect on the properties of membranes [24]. Finally, during fuel cell operation, hydroxyl radicals are responsible for chemical attack of the membrane, which initiates the degradation process [25, 26]. In the degradation of the electrodes, the issue of chemical and morphological instabilities of the catalyst layer is of greater concern at high temperatures [1]. Firstly, corrosion of the carbon support in the cathode may occur if the cathode is held at relatively high oxidation potentials because of the generation of oxygen atoms at the catalyst [27]. Secondly, the morphology of the catalyst may be affected by the agglomeration of the platinum and the increase in particle size during operation [28, 29]. The optimum particle size for oxygen reduction reaction activity is 3-5 nm [29]. Due to the increase of platinum particle size over time, the reaction rate of oxygen reduction gradually decreases, and platinum utilization is reduced. Platinum is also observed to dissolve and re-deposit during long-term operation



[30]. Two mechanisms have been proposed for platinum dissolution [30], but it is not clear yet which one is more effective and how they interact during the operation.

### 1.4 Modeling

Insight into the mechanisms which lead to a reversible or irreversible loss of cell performance and the interaction of these mechanisms with the operating conditions is required. This should be based on the observation of the changes in materials properties. The impact on fuel cell performance is required, before either fuel cell materials can be optimized further with respect to their durability or systems controls and operating procedures can be optimized to prevent the most detrimental conditions. Modeling of different degradation aspects can help to highlight above stressed points by understanding the key reasons and fundamental physical phenomena for particular degradation mechanisms and by predicting the impact of these degradation effects. Another important issue of modeling is understanding the interaction between different specific membrane degradation mechanisms and their complex and mixed effects due to their simultaneously occurrence in real fuel cell operation. This requires multi-scale analysis of undergoing phenomena. This has motivated several recent studies on modeling of PEMFC degradation using data of long-term testing as well as rapid aging testing. It should be noted that modeling has been restricted mainly to the LTPEMFC. However these investigations are of great interest also for high temperature PEMFCs, due to the fact that many degradation mechanisms are actually inherited from the low temperature counterpart [17].

Clearly the previous analysis points out that there is a lack of fundamental understanding of the degradation phenomena of both electrolyte membrane and electrodes for high temperature PEM fuel cells. Numerical modeling may be helpful in comparing different degradation phenomena and in quantifying the effects in terms of global device performance. One feature which is common to most of the degradation phenomena (in particular, corrosion of carbon support and catalyst agglomeration) is the change in the local morphology of the material, driven by chemical reactions and/or mechanical stresses. Modifications in the

micro-morphology produce (a) *direct effects* on mass transport by changing the local porosity and permeability and (b) *indirect effects* by changing the distribution/effectiveness of reaction catalytic sites. The first step for understanding degradation consists in setting up a morphological model of the virgin micro-structure before operation, as a reference condition to compare any degradation with.

Tremendous work has been done over the past few years to visualize GDL and CL using tomography and a number of papers have been published in this area [31, 32, 33]. However, collecting a specific three dimensional morphology is different from developing a general morphological model. A specific three dimensional morphology by tomography allows one to compute precise fluid flow through it and to find macroscopic transport coefficients. However, it does allow one to extrapolate the specific results towards different materials. On the other hand, a morphological model correlates the transport coefficients with the global microscopic structure, but it also (a) explains how different features of the microscopic structure (characteristic lengths, distributions, shapes, orientations, clustering, etc.) determine independently the transport coefficients and (b) suggests design strategies to improve transport coefficients. Hence a morphological model allows one to generate many virtual structures (all compatible with experimental data with regards to some features) in order to find out a design strategy beyond experimental measurements. For example, some PEM electrodes (and in particular the gas diffusion layers) consist of fibers which have been coated with a conductive carbon fill, leading to a highly anisotropic material without any regular micro-structure [34]. On the other hand, fiber-based woven gas diffusion layers for high temperature PEM fuel cells are characterized by some degrees of regularity in the micro-structure and in the orientation of fibers. Regular materials offer better options for optimization but they are also more sensible to degradation phenomena. Hence, before developing any degradation model, the sensitivity of the macroscopic transport coefficients on the assumed micro-structure must be clarified. Moreover, concerning the catalyst layer, we used the morphological model to investigate different distributions of platinum and the consequent mass flow rate, which may affect degradation by phosphoric acid loss.

## 1. INTRODUCTION

---

Few commercial packages are already available to generate both woven and carbon-paper GDLs. One remarkable example is given by GeoDict software [35], initially developed by Fraunhofer ITMW. Besides the woven and non-woven fiber-based structures, GeoDict can generate a wide range of different morphologies including regular-grid, sphere packing, open- and closed-cell foams, sintered ceramic materials and their possible combinations.

### 1.5 Methodology

Pore-scale modeling of fluid flow through electrodes has received intensive research over the past few years [36]. In particular, pseudo-kinetic (also called mesoscopic) approaches are considered efficient computational alternatives to other numerical methods. Pseudo-kinetic approaches based on the Lattice Boltzmann Method (LBM) have become very popular for simulating fluid flows [37, 38, 39, 40, 41, 42] in a variety of applications such as laminar, turbulent, thermal and multiphase flows, and even beyond hydrodynamics, according to some authors [43]. Reasons for this success are attractive implementation, promising handling of complex geometries and suitability for parallel realization. Owing to its excellent numerical stability and constitutive versatility, LBM can play an essential role as a simulation tool for understanding advanced materials and processes [44]. Unlike conventional Navier-Stokes solvers, lattice Boltzmann methods consider flows as to be composed by a collection of pseudo-particles that are represented by a velocity distribution function [41]. These fluid particles reside and interact on the grid nodes. System dynamics and complexity emerge by the repeated application of local rules for the motion, collision and redistribution of these coarse-grained pseudo-particles. LBM is capable to tackle particularly those problems which are ubiquitous characteristics of flows in the world of materials science and engineering [44], including porous media with changing morphology. The lattice Boltzmann method has already proved to be an effective tool in analyzing the porous materials of fuel cells, in particular with regards to the effective permeability. This approach has been already applied to analyze the electrodes of PEM fuel cells [34, 45] and high temperature solid oxide fuel cells (SOFC) [46]. Moreover, pseudo-particles moving on regular grids can easily deal with changing

morphology. To this end, it is sufficient to enable the access of pseudo-particles to new portions of the computational domain or, vice-versa, prohibit their entrance into some other computational regions (e.g. those occupied by obstacles). A recent review over the applications of LBM and other pore-scale models in fuel cells was given in Mukherjee et al. [47], which emphasizes the capability of these pore-scale models toward gaining insight into underlying two-phase dynamics and intricate structure-transport-performance interplay in the PEM fuel cell CL and GDL. To this end, in Chapter 2 a detail description of the adopted methodology (including boundary conditions) is presented.

In this thesis, we focus on direct numerical simulation of the fluid flow through two fundamental regions of HTPEM electrodes, namely a non-woven and woven fiber-based gas diffusion layer (GDL) and a catalyst layer (CL). We believe that focusing on fundamental modeling of materials for HT-PEM fuel cells may promote the development of this technology, as already happened for other types (e.g. solid oxide fuel cells). Moreover, HT-PEM fuel cells usually involve materials with regular micro-structure, where morphological models can be tuned in order to recover the macroscopic transport properties. These validated morphological models can be used in order to feed macroscopic models by material-depending parameters [48], to guide the material production process and to understand degradation phenomena.

## 1.6 Scope of this thesis

The main inducement of this thesis comprises of the investigation of the influence of gas dynamics on the electrochemical performance and durability of the high temperature polymer electrolyte fuel cell (PEFC). This thesis focuses on the electrodes, i.e. gas diffusion and catalyst layers. Ternary transport phenomena are responsible for achieving enhanced performance, those are the transport of reagents through the pore voids system, the transport of electrons via the network of carbon support of catalyst and the transport of protons via the polymer ionomer linkage. In this perspective, pore-scale morphological model of the electrodes plays crucial role providing tunable parameters which allow keeping a precise balance of these ternary phenomena by ensuring as good as possible

## 1. INTRODUCTION

---

a percolation of the gas, solid and ionomer phases, as large as possible an interface area between the catalyst layer and the polymer membrane, and finally as shorter as possible the distance between electrochemical active surface area and the nearest polymer-pore interface. There are three main trends to improve overall performance of the high temperature PBI-based phosphoric acid doped PEM fuel cell corresponding to three regions of polarization curve:

- (i) increase operating temperature to reduce sluggishness of kinetics at low current density region;
- (ii) decrease Ohmic resistance of catalyst layer and polymer membrane by increasing phosphoric acid doping;
- (iii) development of different types of carbon supported catalyst with improved mass transport behavior to mitigate mass transport overpotential at high current density region.

On the other hand, acidic environment at elevated working temperature creates harsh condition to start-up of the degradation processes of electrodes of fuel cell.

Deep understanding of the mass transport properties of the electrodes is an important task not only for improvement of current electrodes, but also for providing pathway for the design of new materials. Thus, the scope of the study within this thesis is to understand how mass transport processes in electrodes affect the performance of HTPEMFC; how different parameters of morphological model of the electrodes, like the clusterization or agglomeration size, the catalyst distribution change the flow field inside the porous electrodes and finally what is the influence of these parameters on lifetime issue. These goals are reached by dealing with the following practical tasks:

- ◇ development of reliable morphological models of the electrodes;
- ◇ investigation of the effects of different parameter of the proposed morphological model on mass transport properties;
- ◇ introduction of different ideas of mitigation of specific degradation processes of PBI-based PA-doped HTPEMFC;

- ◇ application of the invented mitigation strategy to check feasibility;
- ◇ study of the influence of the proposed mitigation idea on the performance of fuel cell.

## 1. INTRODUCTION

---

## 2

# Lattice Boltzmann Method

## 2.1 Introduction

This chapter reports the introduction of numerical tools for 3-dimensional pore-scale modeling of the flow through the electrodes of HTPEMFC used in thesis. Namely, details of Lattice Boltzmann method, such as model of collisional model, lattice type and implemented boundary conditions are considered. Moreover, introduced numerical machinery is applied to compute permeability for specific system.

The Lattice Boltzmann Method (LBM) was derived historically as an improvement of the Lattice Gas Automata (LGA) [41] and it can be derived from kinetic theory of gases, under some proper simplifying assumptions [42]. It should be emphasized that, in spite of these origins, as far as the present thesis is concerned, this method is used as a computational solver of the continuum-based equations for solving the pore-scale fluid flow through porous media.

In this thesis, LBM is preferred to other computational fluid dynamics (CFD) solvers, because of two advantages which are relevant to the present application. The first one is a reasonable handling of complex geometry of porous media, which is consistent with the main objectives of this work, where we need to consider the detailed structure of two layers of high temperature PEM (HTPEM), namely gas diffusion layer (GDL) and carbon supported catalyst layer (CL). The second advantage is a good parallelization potential, owing to an explicit formulation of the evolution operator  $\mathcal{E}$  in terms of the discrete distribution function  $f(\mathbf{r}, t)$ ,



## 2. LATTICE BOLTZMANN METHOD

---

which can be interpreted in terms of Strang splitting [49]:

$$f(\mathbf{r} + \xi, t + 1) = \mathcal{E}f(\mathbf{r}, t) = \mathcal{S}\mathcal{C}f(\mathbf{r}, t), \quad (2.1)$$

consisting of a fully local collision operation  $\mathcal{C}$  and a streaming operator  $\mathcal{S}$ , involving only the neighboring nodes.

### 2.2 From Boltzmann Equation to Lattice Boltzmann Equation

Initially, the basic idea of introducing lattice Boltzmann technique was to bridge the gap between micro-scale and macro-scale by considering a distribution function, which represents the property of the collection of particles. This scale is called meso-scale. A statistical properties of a system with huge amount of particles can be expressed by distribution function  $f(\mathbf{r}, \xi, t)$  being the probability for particles at time  $t$  positioned between  $\mathbf{r}$  and  $\mathbf{r} + d\mathbf{r}$  with velocities between  $\xi$  and  $\xi + d\xi$ .

Due to interparticle collisions there is a nonzero net difference of the numbers of particles entering and leaving the phase space interval  $d\mathbf{r}d\xi$ :

$$\frac{df(\mathbf{r}, \xi, t)}{dt} \equiv \frac{\partial f}{\partial t} + \xi \cdot \nabla f + \frac{\mathbf{F}}{m} \cdot \nabla_{\xi} f = \mathcal{C} \quad (2.2)$$

where  $\mathbf{F}$  is an external force. This equation (2.2) is commonly known as the Boltzmann equation.

The macroscopic quantities could be expressed as hydrodynamic moments of  $f(\mathbf{r}, \xi, t)$  as:

$$\begin{aligned} \rho &= \int m f(\mathbf{r}, \xi, t) d\xi \\ \rho \mathbf{u} &= \int m \xi f(\mathbf{r}, \xi, t) d\xi \\ \rho \theta &= \frac{1}{2} \int m (\mathbf{u} - \xi)^2 f(\mathbf{r}, \xi, t) d\xi \end{aligned} \quad (2.3)$$

It should be noted that in general collision operator has a very complex nature, consequently solution of the Boltzmann equation is really hard task. As it has been established in Ref. [50] the approximation of the collision operator with

simple two body collision operator does not introduce significant error to the outcome of the solution.

The simplest choice for the collision operator  $\mathcal{C}$  corresponds to the most popular Bhatnagar-Gross-Krook (BGK), developed in kinetic theory [51], and successfully applied in the LBM context as well [40]. Moreover, the BGK model can be further simplified by considering isothermal conditions, constant relaxation time and formulating it only for the lattice velocities, namely

$$\mathcal{C} = -\frac{1}{\tau} (f(\mathbf{r}, \xi, t) - f^{eq}(\mathbf{r}, \xi, t)) \quad (2.4)$$

where  $\xi$  denotes velocity,  $\tau$  is the relaxation time, while  $f^{eq}$  is the equilibrium population function, which can be obtained from the local Maxwell-Boltzmann distribution function (see for example [42]) by Taylor expansion.

To derive Lattice Boltzmann equation, there are three basic steps required. First, one should consider only low Mach number expansion for the equilibrium distribution function. Then the velocity space  $\xi$  has to be discretized to find minimum required  $n$  number of discrete velocities  $\{\xi_n\}$ . Finally, physical space  $\mathbf{r}$  has to be discretized accordingly. More precisely, in Eq. (2.2) with negligible external forces and normalized the mass,  $m$ , to 1, one replaces velocity  $\xi$  to a set of vectors  $\xi_i$ , which allows compressing the notation from  $f(\mathbf{r}, \xi, t)$  into  $f_i(\mathbf{r}, t)$ . Bearing in mind that the time step  $dt = 1$  one finally achieves a general form of Lattice Boltzmann equation:

$$f_i(\mathbf{r} + \xi, t + 1) - f_i(\mathbf{r}, t) = \frac{1}{\tau} (f_i^{eq}(\mathbf{r}, t) - f_i(\mathbf{r}, t)) \quad (2.5)$$

In this case, i.e. in a discrete form, all integrals in Eq. (2.4) should be replaced by sum.

Generally, single time step of the LBM equation (2.5) could be split into two sub-steps:

- Collision sub-step ( $\mathcal{C}$ ). The distributions in each node of Cartesian grid are updated using only local information in this node:

$$f'_i(\mathbf{r}, t + 1) = f_i(\mathbf{r}, t) + \frac{1}{\tau} (f_i^{eq}(\mathbf{r}, t) - f_i(\mathbf{r}, t)) \quad (2.6)$$

## 2. LATTICE BOLTZMANN METHOD

---

- Streaming sub-step ( $\mathcal{S}$ ). The updated values of the distributions are propagated along the  $i$ -directions:

$$f_i(\mathbf{r} + \xi, t + 1) = f'_i(\mathbf{r}, t + 1) \quad (2.7)$$

It should be stressed out that non-local streaming term,  $\mathcal{S}$ , is linear, while nonlinear collision term,  $\mathcal{C}$ , is local [41]. Owing to this the LBM has many advantages. It easily handles complex domains, treats multi-phase and multi-component flows without a necessity to trace the interfaces between different phases. Furthermore, it can be naturally adapted to parallel processes computing.

Cartesian square grid in physical space together with a finite set of discrete velocities in the velocity space is a lattice. At each lattice node, it is assumed that the fictitious particles (distribution function) reside. After collision a part of these particles moves along a finite set of specified directions to the neighboring nodes. The definition of lattice depends on the spatial dimension of the problem, the number of velocity directions and the link rule with neighbor nodes. Normally, it has  $DdQq$  type notation, where  $d$  is the dimension, while  $q$  refers to the number of directions or linkages. Noticeably, not every lattice is appropriate for use in the lattice Boltzmann method. There are the following conditions that a set of lattice vectors have to fulfill to recover the Navier-Stokes equation in incompressible limit:

$$\begin{aligned} \sum_i W_i &= 1 \\ \sum_i W_i \xi_{i\alpha} &= 0 \\ \sum_i W_i \xi_{i\alpha} \xi_{i\beta} &= c_s^2 \delta_{\alpha\beta} \\ \sum_i W_i \xi_{i\alpha} \xi_{i\beta} \xi_{i\gamma} &= 0 \\ \sum_i W_i \xi_{i\alpha} \xi_{i\beta} \xi_{i\gamma} \xi_{i\delta} &= c_s^4 (\delta_{\alpha\beta} \delta_{\gamma\delta} + \delta_{\alpha\gamma} \delta_{\beta\delta} + \delta_{\alpha\delta} \delta_{\beta\gamma}) \end{aligned} \quad (2.8)$$

where the Greek subscripts indicate spatial directions,  $W_i$ ,  $\delta_{\alpha\beta}$  and  $c_s$  are the lattice weights coefficients, the delta-Kronecker symbol and speed of sound, respectively. It has been found that in 2D case, a suitable lattice is  $D2Q9$ , presented

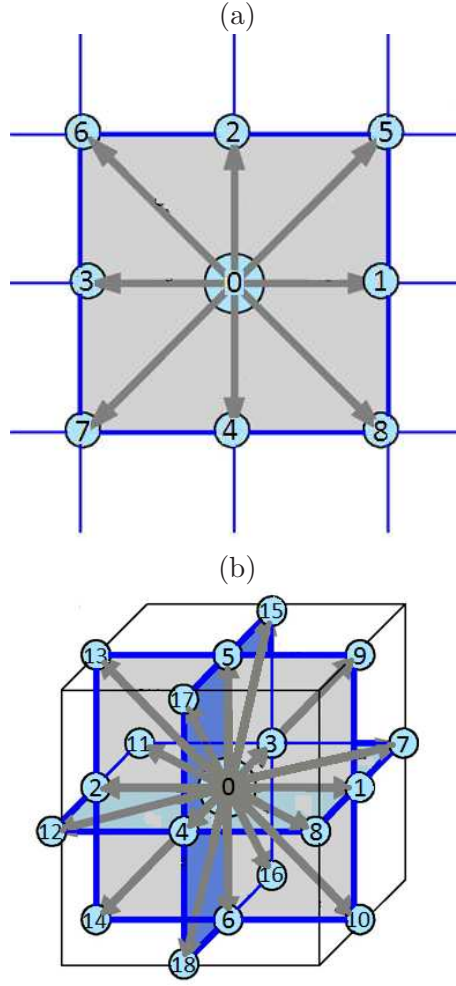


**Figure 2.1:** Geometrical representation of lattice (a)  $D2Q9$  (b)  $D3Q19$ .

in Fig. 2.1 (a), with

$$\xi_i = \begin{cases} (0, 0) & i = 0; \\ (\pm 1, 0), (0, \pm 1) & i = 1, 2, 3, 4; \\ (\pm 1, \pm 1) & i = 5, 6, 7, 8; \end{cases} \quad (2.9)$$

and lattice weight coefficients

$$W_i = \begin{cases} 4/9 & i = 0; \\ 1/9 & i = 1, 2, 3, 4; \\ 1/36 & i = 5, 6, 7, 8; \end{cases} \quad (2.10)$$

For 3D applications, it is  $D3Q19$  lattice, presented in Fig. 2.1 (b), with the set

## 2. LATTICE BOLTZMANN METHOD

---

of velocities and the weight coefficients for this lattice, respectively:

$$\xi_i = \begin{cases} (0, 0, 0) & i = 0; \\ (\pm 1, 0, 0), (0, \pm 1, 0), (0, 0, \pm 1) & i = 1 - 6; \\ (\pm 1, \pm 1, 0), (\pm 1, 0, \pm 1), (0, \pm 1, \pm 1) & i = 7 - 18; \end{cases} \quad (2.11)$$

$$W_i = \begin{cases} 1/3 & i = 0; \\ 1/18 & i = 1 - 6; \\ 1/36 & i = 7 - 18; \end{cases} \quad (2.12)$$

It can be shown that the lattice Boltzmann equations (2.5) recover Navier-Stokes equations in the asymptotic limit. This derivation can be done using the Chapman-Enskog expansion [52] or the Hilbert expansion, also called asymptotic analysis, which has the merit to make particularly evident the effects due to different scaling assumptions, i.e. how lattice velocity is set according to the grid spacing on different grids [53]. It should be emphasised that the parallel between the mesoscopic Lattice Boltzmann and the macroscopic Finite Difference methods is discussed in details in Ref. [54].

In this case, the equation of state of the fluid is:

$$p = \rho c_s^2 \quad (2.13)$$

and with the expression for the kinematic viscosity:

$$\nu = c_s^2 \left( \tau - \frac{1}{2} \right) \quad (2.14)$$

Equilibrium discrete distribution functions, i.e. equilibria, for the  $D3Q19$  model read as follows:

$$f_i^{eq} = W_i \rho \left( 1 + \frac{1}{c_s^2} (\xi_i \cdot \mathbf{u}) + \frac{1}{2c_s^4} (\xi_i \cdot \mathbf{u})^2 - \frac{1}{2c_s^2} (u^2) \right), \quad (2.15)$$

where  $W_i$  and  $\xi_i$  are the weight factors and particle velocities, respectively, with  $c_s = 1/\sqrt{3}$  being the speed of sound.

It should be noted that within the scope of this thesis  $D3Q19$  lattice has been exceptionally used for all 3-D pore-scale simulations.



## 2. LATTICE BOLTZMANN METHOD

---

- Wall

The key concept behind different BC in Lattice Boltzmann method is following. The value of the distribution function describes the state of lattice node at the boundary of the numerical domain is expected to come from a region outside of computational domain, which are unknown. These functions could be reconstructed from boundary constrains, the macroscopic observables (velocity, pressure, temperature, density and etc) at the boundaries of the numerical domain. For any boundary node  $\mathbf{r}_w$  and direction  $i$  such that the node  $\mathbf{r}_w + \xi_i$  does not exist because it is outside the computational domain, the bounce-back rule is the following:

$$f_{BB(i)}(\mathbf{r}_w, t + 1) = f_i^*(\mathbf{r}_w, t), \quad (2.16)$$

where  $BB(i)$  is the lattice index identifying the lattice velocity  $\xi_{BB(i)}$  which is opposite to  $\xi_i$ , namely  $\xi_{BB(i)} = -\xi_i$ , and  $f_i^*$  is the post-collision discrete distribution function, namely  $f_i^* = f_i + (f_i^{eq} - f_i) / \tau$ . For instance, in case of  $D2Q9$  lattice, presented in Fig. 2.2, unknown distribution functions  $f_4, f_7, f_8$  are replaced by opposite known distributions  $f_2, f_5, f_6$ , respectively. It is worth to emphasis that the standard bounce-back BC reproduce macroscopic no-slip wall boundary condition with first-order accuracy in time and space [55]. Higher accuracy has been achieved considering the wall-fluid interface to be located half-way between the wall and the fluid lattice nodes [56]. Further improvement is given by generalizing the previous expression such that the wall location can be freely tuned [57].

The bounce back rule is classified as 'non-wetting' class of boundary condition, where boundary nodes are not considered as a part of the fluid. The boundary conditions proposed by Inamuro [58], Zou-He [59], regularized [60] are examples of 'wet nodes' class of boundary condition. Particularly, in Zou-He BC aforementioned bounce-back rule applied to non-equilibrium distribution functions. In such a way numerical accuracy has been improved in 2D case, while at high Reynolds numbers stability of simulation is pure. By contrast, the regularized boundary condition is very stable at higher Reynolds number, but less accurate at small Reynolds number.

In this work, bounce back boundary condition has been used for the interface nodes between fluid and solid, except the nodes where catalyst particles

(source/sink terms) are deposited. In latter case, outflow boundary condition with fixed pressure value is implemented. Periodic boundary condition is applied at all lateral sides of computational domain. At the inlet, inflow boundary condition with specifying pressure (density) is adapted.

## 2.4 Unit conversion

This section addresses the issues of physical scaling, namely how to relate parameters of Lattice Boltzmann simulation to those of the real physics. At the first glance, it is seems very trivial task to map physical (kinetic or thermodynamic) parameters of an fluid into LB one in terms of lattice units of mass, length and time. For instance, in case of the mass unit it is an arbitrary scaling factor. Other units require careful consideration of physics and stability issue of LB simulation due to their link with the lattice constant and simulation time-step. Consideration of physics means the decision of what physics has to be resolved, because in general, as all conventional CFD solver, LB simulation cannot fully resolve the hierarchy of equations correspond to the real flows of complex fluids. Without going further onto discussion of conversion issues, below the expressions for main kinetic parameters, used in this thesis, are presented.

The first quantity of interest is flow velocity. The conversion from LB unit to physical unit for flow velocity is:

$$u^{phys} = u^{LB} \frac{dx}{dt}, \quad (2.17)$$

where superscripts  $^{phys}$  and  $^{LB}$  denote physical and LB units, respectively, whereas  $dx, dt$  are the length of lattice, simulation time-step in physical units. Here, it should be note that in LB lattice length is set to be unity  $dx^{LB} = 1$  as well as mass  $\rho^{LB} = 1$ . In the case of diffusive scaling the expression for  $dt$  is following:

$$dt = \frac{\nu^{LB}}{\nu^{phys}} dx^2, \quad (2.18)$$

where  $\nu^{LB} = c_s^2 \left( \tau - \frac{1}{2} \right)$  Lattice Boltzmann viscosity presented in Eq. (2.14) with  $c_s^2 = 1/3$  being velocity of sound in Lattice Boltzmann units.



## 2. LATTICE BOLTZMANN METHOD

---

Taking advantage of this, the expression for conversion of units for velocity stands:

$$u^{phys} = u^{LB} \frac{\nu^{phys}}{c_s^2 \left(\tau - \frac{1}{2}\right) dx}. \quad (2.19)$$

Similarly conversion for pressure is:

$$\Delta p^{phys} = \Delta p^{LB} \left(\frac{dx}{dt}\right)^2 \rho_0^{phys} = \Delta p^{LB} \left(\frac{\nu^{phys}}{\nu^{LB} dx}\right)^2 \rho^{phys}. \quad (2.20)$$

Putting these two equations, Eq. (2.19) and Eq. (2.20) into Darcy's equation (see next section for more details) yields to the relation of scaling factor for one of the most important macroscopic transport parameters, namely permeability  $k^{phys}$ :

$$k^{phys} = -\frac{\rho^{phys} \nu^{phys} u^{phys}}{\nabla p^{phys}} = k^{LB} (dx)^2 \quad (2.21)$$

It should be noted that precisely this relation is applied for calculation of the real physical value of permeability using the results of pore-scale Lattice Boltzmann simulation throughout this thesis.

### 2.5 Flow through array of body-centered cubic spheres

In this Section the machinery, i.e. Lattice Boltzmann method, introduced within the previous sections is applied for benchmark problem to calculate the hydraulic permeability associated with multiple ordered packs of identical spheres in a cubic domain. In particular, body-centered cubic spheres (BCC) is considered [55] as shown in Fig. 2.3. A pressure gradient is applied along  $x$ -direction (see Fig. 2.3 for details) and the resulting steady-state averaged superficial velocity is used for computing the permeability values, according to the Darcy's law.

Flow simulations with ordered packing of regular obstacles were performed to check the consistency of numerical predictions of permeability, obtained by different fluid dynamics softwares (PALABOS [61] and ANSYS Fluent<sup>®</sup> [62]) and analytic expressions from the literature. For validation purposes, the convenience of simulating ordered packs of spheres is twofold. First of all, exact analytic expressions are available. Secondly, adoption of periodic boundary conditions allows one to reduce the computational demand (in comparison with packs made

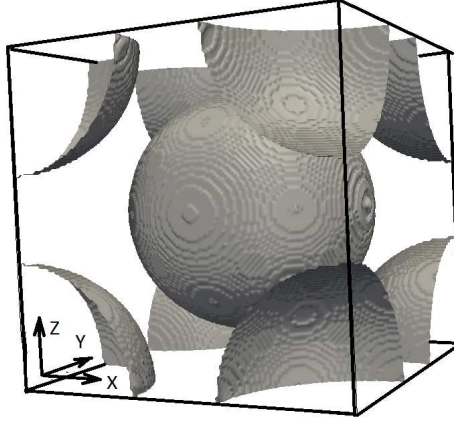


**Figure 2.3:** Periodic unit cell of an infinite array of body-centered cubic spheres.

of randomly placed spheres [34], where larger computational domains are typically required).

Permeability  $k$  is a constant factor appearing in the Darcy's law [63], which relates the pressure gradient  $\nabla p$  across a porous medium to the volume averaged velocity  $u$ , i.e.,

$$u = -\frac{k\nabla p}{\mu}, \quad (2.22)$$

where  $\mu$  denotes viscosity. The volume averaged velocity, also called discharge per unit area, is not the velocity which fluid particles traveling through the pores is experiencing. In order to find out the latter quantity, the volume averaged velocity must be divided by the porosity to account for the fact that only a fraction of the total formation volume is available for flow.

Numerical results were compared to values as predicted by the analytic expressions (see [64, 65]). Prediction of permeability of porous media with periodic structures dates back to the theoretical works of Hasimoto [66], and later on, to the work of Sangani and Acrivos [64], which performed analytic and numerical studies of periodic arrays of spheres for different configurations. According to these models, the permeability can be computed as

$$k_S = \frac{R^2}{6\pi d_k} \left( \frac{L}{R} \right)^3, \quad (2.23)$$

## 2. LATTICE BOLTZMANN METHOD

---

where  $L$  is the edge of the periodic cell,  $R$  is the radius of the sphere and  $d_k$  is a dimensionless drag coefficient. The dimensionless drag coefficient  $d_k$  is determined by geometric parameters of the porous media, and can be represented by a power series of  $\gamma$  as follows

$$d_k = \sum_{n=0}^{30} q_n \gamma^n, \quad (2.24)$$

where the coefficients  $q_i$  are tabulated [64]. The dependence of the parameter  $\gamma$  on porosity  $\varepsilon$  takes into account the considered configuration, i.e. the spheres arrangement. For body-centered cubic (BCC) configuration, the dependence reads

$$\gamma = \left( \frac{8(1-\varepsilon)}{\sqrt{3}\pi} \right)^{1/3}. \quad (2.25)$$

It should be noted that this analytical model is accurate in the limits of low and high porosity. More specifically, analytic expression given by Hasimoto [66] is not valid for  $\gamma \leq 0.2$ , and in work by Sangani [64] authors improved this using the same method as Hasimoto, but adding extra terms in the velocity expression, with a wider validity range:  $0 < \gamma < 0.85$ . For high densities they obtained the lubrication type approximations for narrow gaps [67].

Another popular relation was proposed by Kozeny [68] and later modified by Carman [69]. The resulting equation is known as the Kozeny-Carman (KC) equation. Authors considered a porous material as an assembly of capillary tubes for which the equation of Navier-Stokes can be used. This yields the permeability  $k$  as a function of porosity  $\varepsilon$ , specific surface, and a factor accounting for the shape and tortuosity of channels. Since its first appearance in [69], this equation has taken several forms, including the following one (Eq. (2.26)) that is commonly used for porous media with spherical particles [65]:

$$k_{KC} = \frac{D^2}{150} \frac{\varepsilon^3}{(1-\varepsilon)^2}, \quad (2.26)$$

where  $D$  is the sphere diameter.

We notice that the estimates of permeability as predicted by Eq. (2.23) on (2.26) show a good agreement only for a small range of porosity, namely  $\varepsilon \in [0.7; 0.82]$ .

The convergence of permeability for ordered arrays of spheres has been analyzed as a function of mesh resolution. We have simulated a flow through idealized three-dimensional porous structures composed of ordered arrays of spheres with BCC packing configuration, by setting fixed pressure boundaries at inlet and outlet (along  $x$ -direction in Fig. 2.3). Sphere surfaces were treated as no-slip wall boundaries using the bounce-back boundary conditions (see previous Section). In this configuration, we considered a cubic unit cell with periodic boundary conditions along both  $y$ - and  $z$ -direction. Following [65], we adopted an edge of the periodic computational box with  $L = 1.917 \text{ cm} = 1.917 \times 10^{-2} \text{ m}$  and porosity  $\varepsilon = 0.32$ .

**Table 2.1:** Input parameters and obtained numerical results by ANSYS Fluent<sup>®</sup>, PALABOS, literature [65] and Kozeny-Carman model. The PALABOS results are reported first in dimensionless units (the so-called lattice units  $l.u.$ , see [41]) and then in physical units.

Parameters	
Porosity	0.32
$R/L$ ratio	0.433
Sphere diameter $D$	0.0166 $m$
Edge of computational box $L$	0.01917 $m$
ANSYS Fluent <sup>®</sup>	
Dynamic viscosity	0.001 $kg/(m \times s)$
Pressure gradient $\nabla p$	0.245 $Pa/m$
Average pore velocity	$0.7970 \times 10^{-04} \text{ m/s}$
Surface velocity	$0.3276 \times 10^{-04} \text{ m/s}$
Mass flow rate	$0.1192 \times 10^{-04} \text{ kg/s}$
Permeability-FLUENT	$1.337 \times 10^{-07} \text{ m}^2$
PALABOS	
Resolution	$512 \times 512 \times 512$
Lattice viscosity $\nu$	$1/6 \text{ l.u.}$
Lattice pressure gradient	$9.78474 \times 10^{-08} \text{ l.u.}$
Lattice average velocity	$5.32578 \times 10^{-05} \text{ l.u.}$
Lattice permeability	$90.7158 \text{ l.u.}$
Permeability-PALABOS	$1.2757 \times 10^{-07} \text{ m}^2$
OTHERS	
Permeability [65]	$1.240 \times 10^{-07} \text{ m}^2$
Permeability Eq. (2.26)	$1.302 \times 10^{-07} \text{ m}^2$

In order to validate the solver that is used in the rest of the thesis, i.e. LBM

## 2. LATTICE BOLTZMANN METHOD

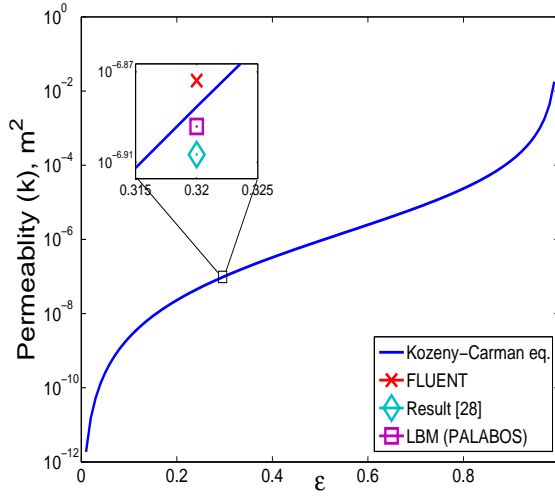


**Figure 2.4:** Permeability as a function of porosity given by Eq. (2.26). Inset: The results of different numerical methods for porosity  $\varepsilon = 0.32$ .

solver with  $D3Q19$  lattice implemented in PALABOS [61], different comparisons were carried out. In Table 2.1 the input parameters imposed in our simulations, as well as the obtained results, are presented. Values for permeability obtained by PALABOS were compared with (a) other LBM simulations [65], (b) results obtained by commercial software ANSYS Fluent<sup>®</sup> [62] and (c) analytic predictions by Kozeny-Carman equation (see Eq. (2.26)). In particular, the PALABOS results, as common in the LBM literature, are expressed first in dimensionless units (so-called lattice units  $l.u.$ , see [41]) and then in physical units by means of proper scaling factors. For the sake of clarity, all these data are shown in Fig. 2.4 (inset), where good agreement is found. In LBM simulations by PALABOS, the relaxation parameter has been chosen as  $\omega = 1.0$   $l.u.$  and the kinematic viscosity  $\nu = 1/6$   $l.u.$  in order to minimize the effect of viscosity on permeability (see in particular Fig. 4 of Ref. [55]). This choice allows to obtain the maximum accuracy by means of the simplified BGK collisional model and to avoid the use of more complex collisional models, like the multiple-relaxation-time (MRT) model (see [70] and [34] for applications to PEM fuel cells).

In Table 2.2 the dependence of permeability on the numerical resolution, i.e. number of computational node for discretizing the box edge, is reported. Results

**Table 2.2:** Dependence of permeability on resolution. The results are reported first in dimensionless units (the so-called lattice units  $l.u.$ , see [41]) and then in physical units.

Resolution	$64 \times 64 \times 64$
Lattice average velocity	$3.68895 \times 10^{-05} l.u.$
Lattice pressure gradient	$7.93651 \times 10^{-06} l.u.$
Lattice permeability	$0.77468 l.u.$
Actual permeability	$0.697212 \times 10^{-07} m^2$
Resolution	$128 \times 128 \times 128$
Lattice average velocity	$1.04201 \times 10^{-5} l.u.$
Lattice pressure gradient	$3.93701 \times 10^{-06} l.u.$
Lattice permeability	$4.41116 l.u.$
Actual permeability	$0.992511 \times 10^{-07} m^2$
Resolution	$256 \times 256 \times 256$
Lattice average velocity	$4.91507 \times 10^{-06} l.u.$
Lattice pressure gradient	$3.92157 \times 10^{-08} l.u.$
Lattice permeability	$20.889 l.u.$
Actual permeability	$1.175006 \times 10^{-07} m^2$
Resolution	$512 \times 512 \times 512$
Lattice average velocity	$5.32578 \times 10^{-05} l.u.$
Lattice pressure gradient	$9.78474 \times 10^{-08} l.u.$
Lattice permeability	$90.7158 l.u.$
Actual permeability	$1.275691 \times 10^{-07} m^2$

clearly show a considerable dependency of permeability for coarser meshes, while a plateau is observed starting from a  $256^3$  resolution. Hence the  $512^3$  resolution can be considered accurate enough to get mesh-independent results.

Simulations were performed using a DELL Precision<sup>®</sup> T7500 Linux workstation with CPU Due Intel<sup>®</sup> Xeon<sup>®</sup> X5650 (six cores, clock rate 2.66 GHz, 12 MB cache) and 48 GB (6×8GB) of DDR3 memory (1333 MHz), with OS Red Hat Enterprise Linux version 6.3.

## 2.6 Conclusion

The main goal of present chapter is to introduce the numerical tools used for 3-dimensional pore-scale simulations in thesis. Lattice Boltzmann method with the simplest collision operator, i.e. Bhatnagar-Gross-Krook (BGK) with  $D3Q19$  lattice is exceptionally used for all direct numerical simulations. Within the scope of this thesis, bounce back boundary condition is implemented at the interface

## 2. LATTICE BOLTZMANN METHOD

---

nodes between fluid and solid, except the nodes where catalyst particles (sink terms) are deposited. Moreover, in order to validate the solver that is used in the rest of the thesis the introduced numerical machinery is applied to compute permeability for specific system, which shows a good agreement with other conventional techniques. Although, Lattice Boltzmann models are considered to be very promising scheme for the analysis of reactive mixtures in porous medium (see Ref. [71, 72]), the pore-scale simulations, in this thesis, are restricted to the single-phase non-reactive flow consideration.

## 3

# Morphological model

### 3.1 Introduction

This chapter is devoted to the development of morphological models for the main study subject, namely electrodes of HTPEMFC. This micro-morphological model starts with elaboration of reliable algorithm of reconstruction of both gas diffusion and catalyst layers. Furthermore, additional tunable parameters of morphological model for catalyst layer, like clusterization or agglomeration size, distribution of catalyst etc, are invented. Finally, at the end of this chapter rarefaction effects is taken into account by properly post-processing the numerical results.

The modeling activity starts collecting all available data of the micro-morphology and the macroscopic transport parameters. Particularly, for this thesis, the microstructure data is taken from the Scanning Electron Microscope (SEM) micro-morphology images of the HT-PEM fuel cell reported in Fig. 3.1, which are original and purposely obtained for this goal. The considered system consists of an impermeable (for the gases) electrolyte at the center (Fig. 3.1 (a) and (c)), with two very thin regions at the upper and bottom sides of the electrolyte, sandwiched between the electrolyte and the electrodes. These regions are the carbon supported Pt catalyst layers (Fig. 3.1 (d)), which hold together the membrane and two (anode and cathode) woven gas diffusion layers (Fig. 3.1 (a) and (b)). On the other hand, the most significant geometrical and macroscopic transport parameters of the system can be collected from literature and given in Table 3.1. Two options are typically possible when dealing with modeling of complex



### 3. MORPHOLOGICAL MODEL

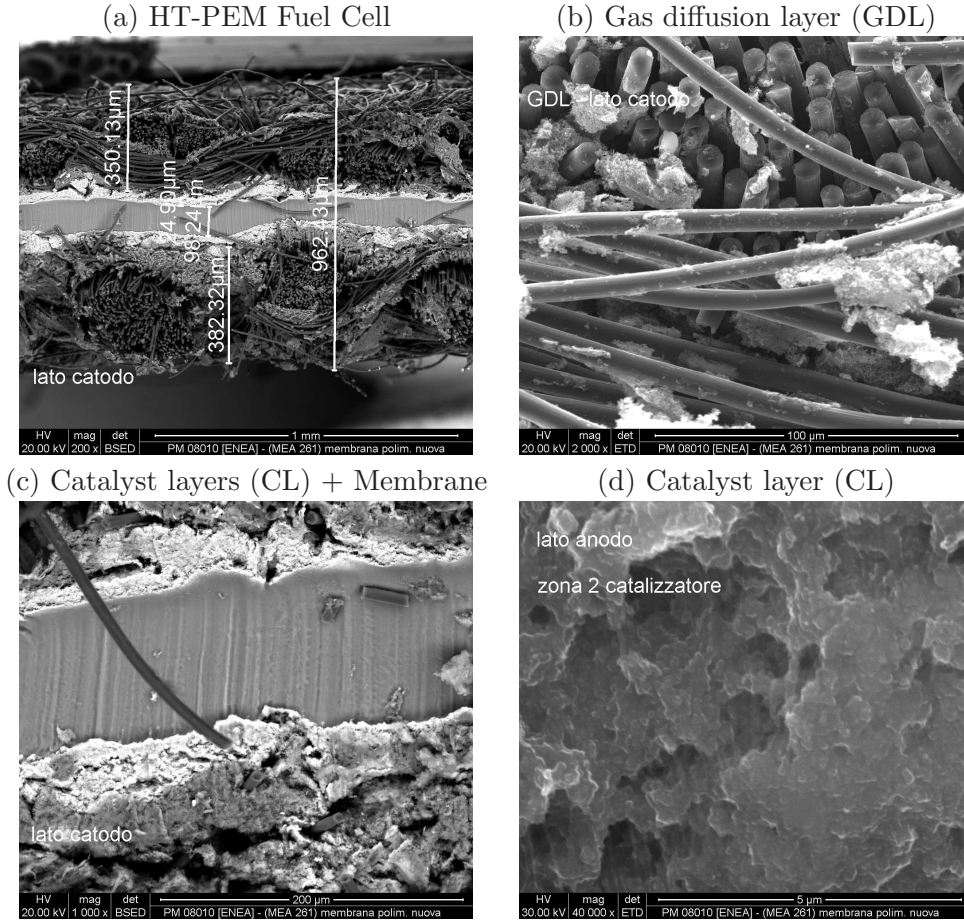


**Figure 3.1:** Micro-morphology of a HTPEM fuel cell (*Celtec – P1000* by BASF®) by Scanning Electron Microscope (SEM) imaging. These images are acquired purposely for the present work in the research center ENEA Brasimone in the framework of the national PRIN 'Microscopic modeling and degradation analysis of the membrane electrode assembly (MEA) in high temperature PEM fuel cells' project (see also [16]).

media. One option is to obtain directly 3D information. The advent of dual-beam focused ion beam scanning electron microscopy (FIB-SEM) has greatly facilitated this process by providing high-quality volumetric data [73]. However, image analysis techniques remain nowadays the most popular because of the low cost of equipments and instrumentations, which have already large-diffusion [74].

In this thesis, the focus is made on the latter approach, which is based on post-processing 2D SEM images in order to get the most meaningful topological information. The considered materials are characterized by a regular micro-structure

**Table 3.1:** Typical transport parameters of the GDL and CL of a HT-PEM fuel cell from literature.

Parameter	Value	Reference
$l_{GDL}$	$400 \mu m$	Siegel [75]
$\varepsilon_{GDL}$ (BASF Celtec-P 1000)	0.7	Kvesic [76]
$k_{GDL}$ (BASF Celtec-P 1000)	$10^{-12} m^2$	Kvesic [76]
$\varepsilon_{GDL}$ (BASF Celtec-P 2000)	0.78	Siegel [75]
$k_{GDL}$ (BASF Celtec-P 2000)	$5 \times 10^{-13} m^2$	Siegel [75]
$l_{CL,a}$	$30 \mu m$	Siegel [75]
$l_{CL,c}$	$40 \mu m$	Siegel [75]
Carbon support particle size	$30 - 40 nm$	Antolini [77]
$\varepsilon_{CL}$	$0.5 - 0.6$	Lobato [15]
$k_{CL}$ (BASF Celtec-P 2000)	$1 \times 10^{-13} m^2$	Siegel [75]

(in particular fiber-based woven GDL), which makes possible the development of morphological models with only few parameters.

We have performed pore-scale morphological reconstructions of the microscopic topology of the system using information given in Table 3.1 and micro-morphology images (Fig. 3.1). This has been done in order to define realistic paths for the pore-scale fluid flow. To this purpose, a digital map of the whole geometry is collected in a one dimensional array, whose elements correspond to the mesh nodes. Three possible values are assigned to the array elements, 0 for fluid, 2 for solid and 1 for boundaries between solid and fluid. Tracing the interface between solid and fluid nodes is useful for applying boundary conditions (e.g. the bounce-back rule discussed in the previous Section 2). The importance of this tracing appears when one deals with catalyst layer. Namely, in order to mimic realistically catalyst layer, one needs to consider distribution of catalyst particles across porous electrode.

The one dimensional array can be reported mathematically by the following definition

$$\mathcal{M}_{i_x, i_y, i_z} = \begin{cases} 0 & (i_x, i_y, i_z) \in fluid \\ 1 & (i_x, i_y, i_z) \in fluid \cap solid \\ 2 & (i_x, i_y, i_z) \in solid \end{cases} \quad (3.1)$$

To this end, in the following two sections, the details on how to generate the arrays  $\mathcal{M}_{GDL}$  and  $\mathcal{M}_{CL}$  for GDL and CL, respectively, which represent the geometries of reconstructed porous media, are reported. It should be noted that

### 3. MORPHOLOGICAL MODEL

---

topology reconstruction of the different layers (GDL and CL) has to be considered separately, due to the considerable disparity in reconstruction algorithms and characteristic scales of their geometry.

#### 3.2 Reconstruction of fiber-based gas diffusion layer

Gas diffusive layer (GDL) is one of the key components of polymeric electrolyte membrane (PEM) fuel cells. GDL generally made of carbonaceous material fibers and has twofold functionality: first, gas reactants and products transportation to or from reaction layer through pores, consequently its microstructure has a significant influence on mass transport; secondly, the carbon fibers manage the transport of electrons. These facts allow one considerably improve not only whole performance, but also stability of PEM FC by optimizing micromorphology of GDL. The latter is closely related to degradation phenomena. Beside these transport characteristics, GDL has to possess low electronic resistance and proper hydrophobic characteristics.

In the framework of this thesis, two types of the fiber-based gas diffusion layers are considered. The first one is specific GDL produced by Freudenberg<sup>®</sup> [78] company which micro-morphology is non-woven stochastic structure. By contrast, the second type of GDL is woven carbon cloth by AvCarb<sup>®</sup> [79] used in Celtec by BASF<sup>®</sup> has quite regular structure. These two types of GDL of a proton exchange membrane fuel cell (PEMFC) commonly classified depending on orientation of fibers: regular woven (curvilinear clusters of non-crossed fibers) and stochastic non-woven (linear and curvilinear fibers with chaotic orientation).

##### 3.2.1 Stochastic non-woven structure

The typical examples of non-woven GDL are commercially available Freudenberg Plain H2315, SGL 25 BC with 5% polytetrafluoroethylene (PTFE), and TGP-H-060 with 7% PTFE, while for woven GDL is AvCarb<sup>®</sup> used in Celtec by BASF<sup>®</sup>. The main technical characteristics of different GDL types, which are interesting for PEM application, are presented in Table 3.2. In the framework of this thesis, we deal with the benchmark MEAs of Danish Power System. They are using Freudenberg GDL and manufacture their own catalytic layer. There

**Table 3.2:** Technical data for different GDL by Freudenberg<sup>®</sup>.

Name	H2315I6	H2315C4	H2415I2C3
Hydrophobic treatment	yes	no	yes
Micro-porous layer	no	yes	yes
Thickness@0.025MPa (Internal) in $\mu m$	210	255	290
Area weight (DIN EN ISO 29073-1) in $g/m^2$	115	135	150
Porosity	0.75	0.75	0.75
Fiber diameter ( $\mu m$ )	9.5	7	9.5
TP electrical resistance@0.6MPa (Internal) ( $m\Omega \times cm^2$ )	10	10	12
IP electrical resistance (Internal) in $\Omega$	0.8	0.8	0.6
Air permeability acc. to Gurley (ISO 5636-5) in $s$	-	50	35
IP air permeability (Internal) in $\mu m^2$	2.0	2.1	1.8
Tensile strength (DIN EN ISO 29073-3) in $N/50 mm$	80	60	110

is no micro-porous layer (MPL) included with the samples tested. The surface morphology of the GDL samples was examined with a JEOL JSM-6400LV scanning electron microscope (SEM). Figure 3.2 shows SEM images of two main cross sections of a GDL sample.

The first step to a reconstruction of a GDL micro-morphology is to make systematic study of these SEM images and the images were collected in the secondary electron mode at 20  $keV$  with different magnifications. Notice that additional information which helps modeling could also be obtained on the liquid  $H_3PO_4$  adsorption on catalyst particles by immersion calorimetry experiments and on pore distribution of porous media by  $Hg$  porosimetry.

A rough analysis of the SEM images of different cross sections of a GDL sample in Figure 3.2 gives us ideas about basic modeling assumptions. The main assumption is that the considered fiber-based material can be decomposed into stochastically independent thin layers with a thickness equal to one fiber diameter (see Figure 3.2 (d)). Moreover, we can make another assumption that the fibers can be mutually interpenetrating curved tubes, which are horizontally oriented within each thin layer. The latter assumption can be proven looking at vertical cross section visualized in Figure 3.2 (c-d).

Hence, to reconstruct the micro-morphology of a fiber-based non-woven GDL the following assumptions are made:

- (a) A GDL is the parallel decomposition of many non-interconnected thin layers;
- (b) The thickness of each layer is equal to the diameter of fiber;

### 3. MORPHOLOGICAL MODEL

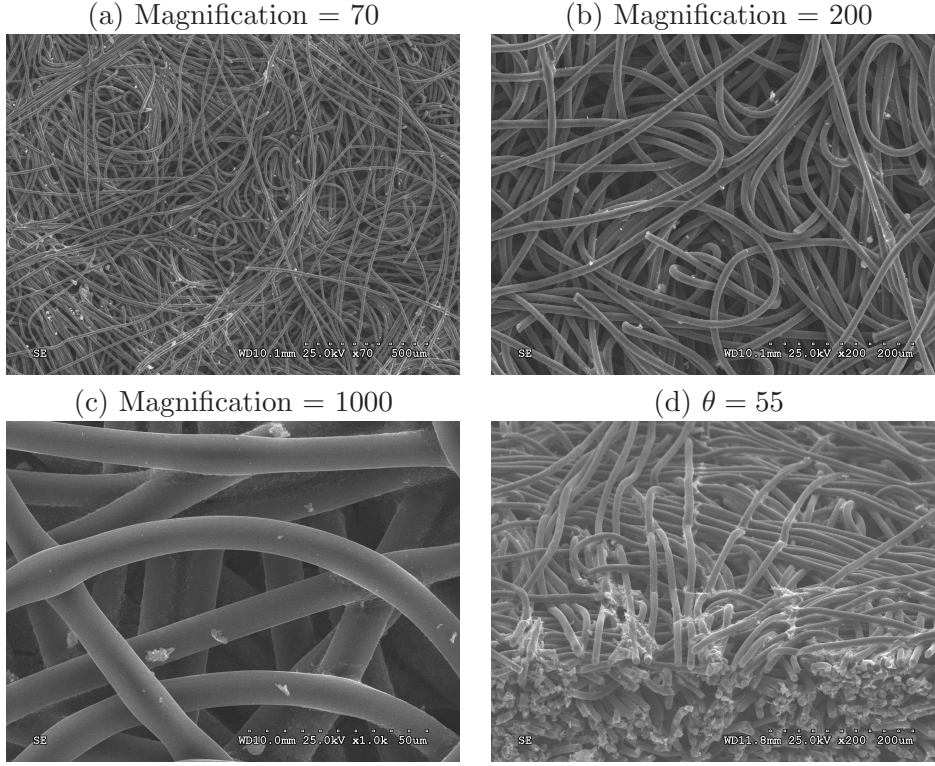


**Figure 3.2:** SEM images of (a-c) a planar with different magnification level; (d) a vertical; cross section of Freudenberg GDL by Freudenberg® Non-Wovens Technical Division, Lowell, MA. These SEM images are obtained in the Institut Charles Gerhardt Universite Montpellier II in the framework of the European FP-7 project 'Automotive Range extender with high TEMperature Improved pemfc meas and Stacks' (ARTEMIS).

- (c) Layers are independent each others;
- (d) Thin layers comprise with mutually interpenetrating fibers;
- (e) Fibers can be modeled as a tube with polynomial directrix;
- (f) Tubes are oriented in the horizontal plane of single thin layer;
- (g) Tubes made on a series of straight cylinders leaded by polynomial directrix.

A digital map of the whole geometry has been collected in a one dimensional array  $\mathcal{M}$ , whose elements correspond to the mesh nodes. Three possible values are assigned to the array elements, 0 for fluid, 2 for fiber and 1 for boundaries between fiber and fluid. Tracing the interface between solid and fluid nodes is useful for



applying boundary conditions, namely the bounce-back boundary condition. The one dimensional array can be reported mathematically by the following definition:

$$\mathcal{M} = \begin{cases} 0 & (i_x, i_y, i_z) \in fluid \\ 1 & (i_x, i_y, i_z) \in fluid \cap solid \\ 2 & (i_x, i_y, i_z) \in solid \end{cases} \quad (3.2)$$

For the sake of simplicity, the direction of decomposition coincides with  $z$ -axes, while fibers of a single layer are in  $xy$ -plane. Description of this algorithm is organized from bottom to top, starting with construction of a single cylinder, which is the simplest constitutive part of curvilinear tube up to decomposition of all single layers of a porous GDL.

Let's begin with reconstruction of a single fiber. A single fiber is modeled as a curvilinear tube with a polynomial directrix (assumption (e)), which has the following form:

$$f(t) = \sum_{i=1}^n \alpha_i t^i \quad (3.3)$$

To find function of directrix, first we generate  $N_{rp}$  number of random points inside a given domain  $x \in [1, n_x]$  and  $y \in [1, n_y]$  and fit this data by polynomial fitting. This procedure gives us the coefficients  $\alpha_n$  of polynomial function, Eq. (3.3), which maximal degree  $N_{power}$  is also randomly generated. Notice that here  $N_{power} \in [2, n_{max}]$  an integer range is considered,  $N_{power} = 2$  standing for the straight line, while  $n_{max} < N_{rp}$  condition has been fulfilled.

To this intent, MATLAB<sup>®</sup> and Statistics Toolbox software has been used. Namely, **polyfit** function has been used for finding the coefficients of polynomial for given data and maximal degree by the least-square algorithm, whereas **polyval** function has computed data of function using the coefficients found by **polyfit**. It should be noted that the first and the last points of the randomly generated data are placed on the boundary of considered domain.

Having found the function of directrix, it is immediately possible to start reconstructing a single fiber. For simplicity it is assumed that a tube is built by a series of straight cylindrical fractions (assumption (g)) of two neighboring points  $(x_i, y_i)$  and  $(x_{i+1}, y_{i+1})$  in trajectory along the given directrix. In order to ensure smoothness of curvature of a fiber the number of the constitutive fractions has

### 3. MORPHOLOGICAL MODEL

---

to be large enough. In particular case,  $n_x = n_y = 256$  has been taken, which is enough to achieve this goal.

Defining the value of digital map  $\mathcal{M} = 2$  inside a tube, we generate a cylindrical fraction of it. This could be done in threefold. The first step is generation of cylinder coordinates with given length and radius. The length of a cylindrical fraction can be found as

$$l_{i,i+1} = \sqrt{(x_i - x_{i+1})^2 + (y_i - y_{i+1})^2}$$

Thus all points fulfilled the following condition (equation of a cylinder)  $\mathcal{M} = 2$  value should defined:

$$y^2 + z^2 \leq R^2, \quad (3.4)$$

where  $R$  is the radius of fiber. The second step is rotation of fraction around  $z$ -axes, where the rotational angle is

$$\theta_z = \tan^{-1} \left( \frac{y_i - y_{i+1}}{x_i - x_{i+1}} \right)$$

The rotational transformation of coordinates around  $z$ -axes has following form:

$$\begin{pmatrix} x' \\ y' \\ z' \end{pmatrix} = R(\theta_z) \times \begin{pmatrix} x \\ y \\ z \end{pmatrix} = \begin{pmatrix} \cos \theta_z & -\sin \theta_z & 0 \\ \sin \theta_z & \cos \theta_z & 0 \\ 0 & 0 & 1 \end{pmatrix} \begin{pmatrix} x \\ y \\ z \end{pmatrix} \quad (3.5)$$

The final step is parallel displacement of a cylindrical fraction to the appropriate place in a tube:

$$\begin{pmatrix} x'' \\ y'' \\ z'' \end{pmatrix} = \begin{pmatrix} x' + x_i \\ y' + y_i \\ z' \end{pmatrix} \quad (3.6)$$

Latter can be combined into the following transformation of coordinates:

$$\begin{pmatrix} x'' \\ y'' \\ z'' \end{pmatrix} = \begin{pmatrix} x \cos \theta_z - y \sin \theta_z + x_i \\ x \sin \theta_z + y \cos \theta_z + y_i \\ z \end{pmatrix} \quad (3.7)$$

It should be noted that to avoid redundant computation it has to be considered only cylinders inside of computational domain  $x \in [1, n_x]$  and  $y \in [1, n_y]$ . However, there are still the cases where one of the neighboring points is inside, while another outside the domain. In such cases, the outside point should be replaced

by appropriate point on the boundary, namely for example if  $x_i < x_{min} \equiv 1$  ( $x_i > x_{max} \equiv n_x$ ), we replace  $x_i = 1$  ( $x_i = n_x$ ).

Thereby, one has an approach to generate a cylindrical fraction of a tube, by repeating of which one can finish reconstruction of a single fiber. Taking advantages of this approach one can switch from a single fiber reconstruction to thin layers. The manufacturer of the non-woven fiber-based GDL (Freudenberg Non-Wovens Technical Division, Lowell, MA) provides the value of porosity (see Table 3.2) that  $\varepsilon = 0.75$ . Hence, this information can be used for estimation of how many curvilinear fibers has to be generated on each thin layer (assumption (c)), where each fiber is generated independently and may interpenetrate other fibers (assumption (d)). The generation of a single fiber is repeated until the ratio of fibers volume to total volume of a single thin layer reaches value  $1 - \varepsilon$ , certainly with some accuracy  $\varepsilon_{error}$ . In Figure 3.3 the result of the reconstruction

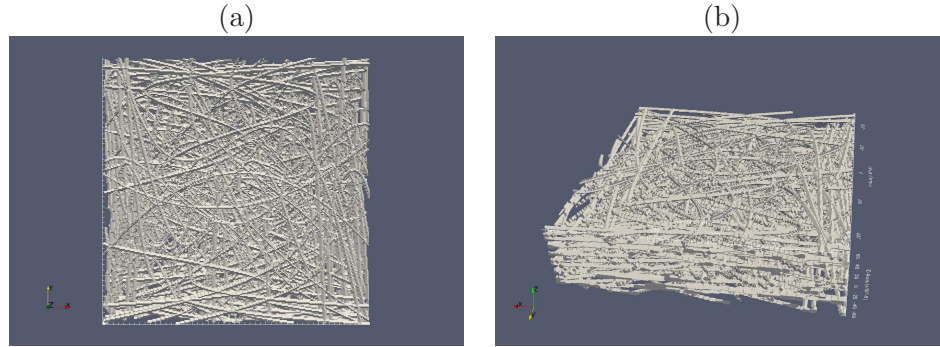


**Figure 3.3:** (a) a planar; (b) a vertical; view of the micro-morphology of GDL reconstructed using the proposed algorithm.

simulation based on the proposed algorithm is shown. It can be seen by rough visual comparison with the real SEM in Figure 3.2 that the simulated micro-morphology quite nicely mimics all distinguish features of real one. However, more realistic validation of the results of our algorithm could be done by comparing structural characteristics computed from the 3D image gained by synchrotron tomography. Hence, a proof of reliability of the proposed algorithm is to show that transport-relevant structural properties of the stochastic model match those of the real synchrotron image quite well.



### 3. MORPHOLOGICAL MODEL

#### 3.2.2 Regular woven structure

Let us start with reconstruction of a woven gas diffusion layer, similar to the one depicted in Fig. 3.4, whose characteristic cell consists of four orthogonal bundles of fibers. The typical examples of woven GDL are commercially available AvCarb<sup>®</sup>, which is used for building of Celtec MEA by BASF<sup>®</sup>. By analogy

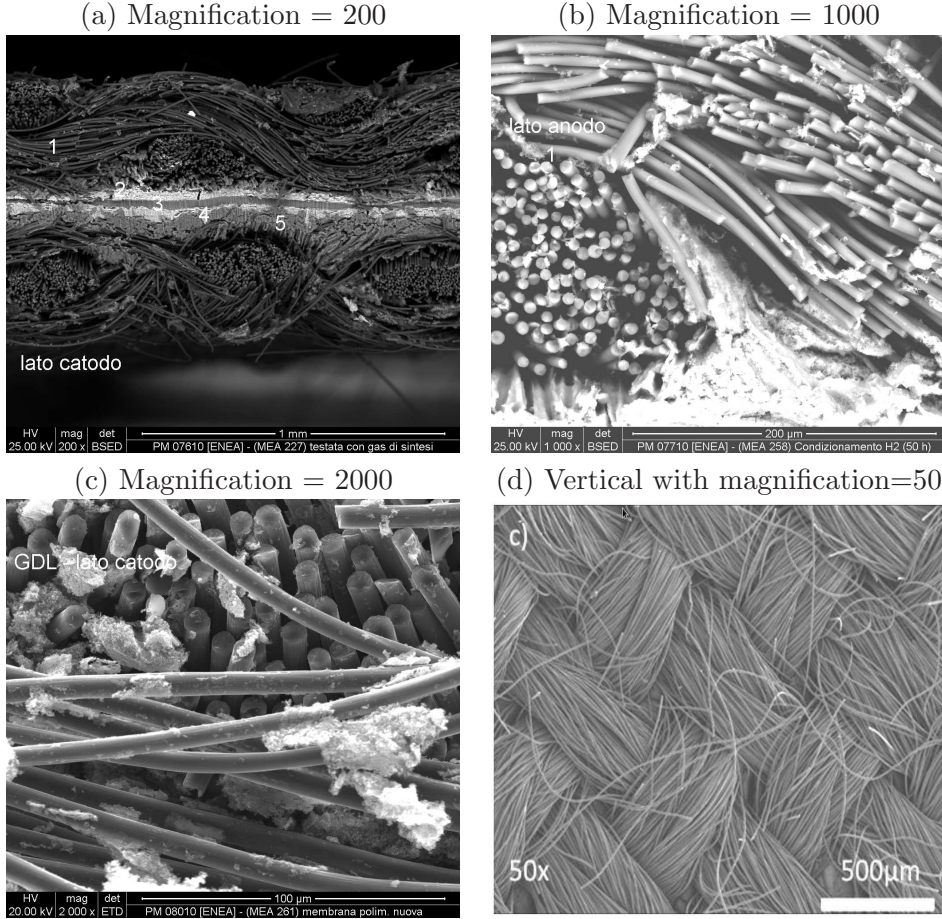


**Figure 3.4:** SEM images of (a-c) a vertical with different magnification level; (d) a planar; cross section of AvCarb 1071 woven gas diffusion layer. These images are acquired purposely for the present work in the research center ENEA Brasimone in the framework of the national PRIN 'Microscopic modeling and degradation analysis of the membrane electrode assembly (MEA) in high temperature PEM fuel cells' project (see also [16]).

with the previous Section 3.2.1, the first step to a reconstruction of a GDL micro-morphology is to make systematic study of these SEM images and the images were collected in the secondary electron mode at 20 keV with different magnifications

(Fig. 3.4 (a-c)). An analysis of the SEM images of different cross sections of a GDL sample gives us ideas of the reliable reconstruction about basic modeling assumptions, which are as follows:

- (i) Fibers of the GDL are grouped into two pairs of mutually orthogonal bundles;
- (ii) A cross-section of a bundle is an ellipse with  $L_A$  and  $L_B$ , being semi-major and minor axes, respectively;
- (iii) Fibers are homogeneously distributed in a bundle;
- (iv) A fiber is modeled as a cylinder with sinusoidal directrix.

For sake of simplicity, we have considered the  $x$ -direction as the main flow direction, consequently  $yz$ -plan is a woven plane (see Fig. 3.5 for details). The

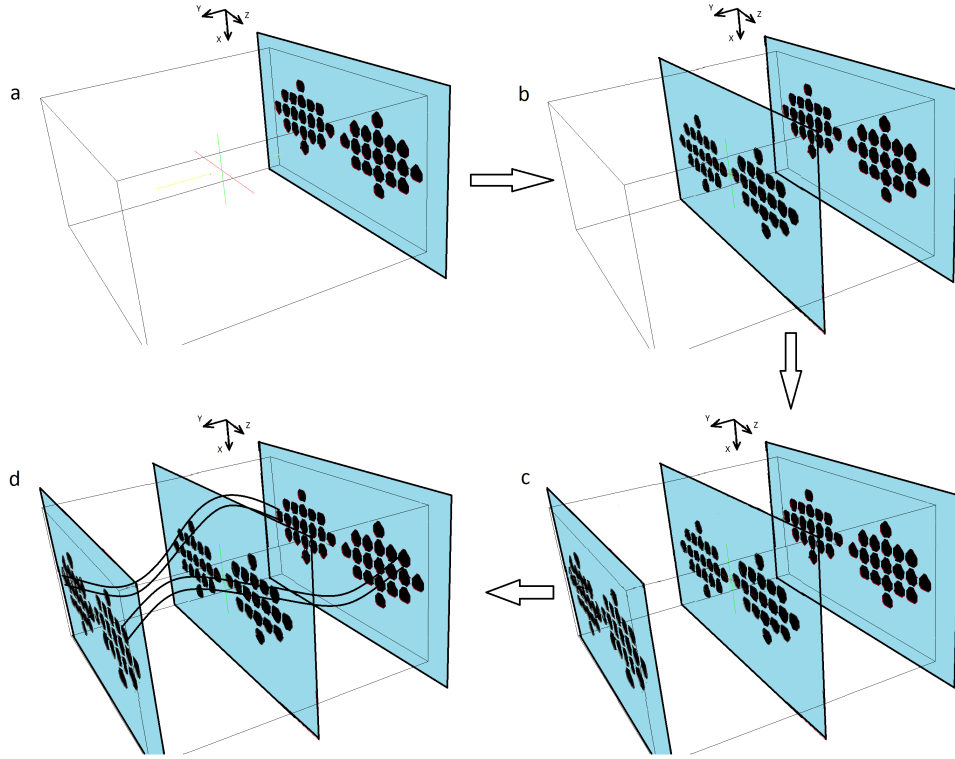


**Figure 3.5:** Schematic representation of the reconstruction steps for a woven fiber-based gas diffusion layer [16].

### 3. MORPHOLOGICAL MODEL

---

suggested reconstruction procedure starts with the estimate of the average distance  $d$  between two nearest neighbor fibers within a bundle and the radius of fibers  $r$ . These parameters can be obtained by analyzing the images in Fig. 3.1 and using simple geometric relations, namely

$$d = \frac{1}{2} \left( \frac{L_A}{N_A} + \frac{L_B}{N_B} \right) - 2r, \quad (3.8)$$

$$r = \left( \frac{(L_A N_B + L_B N_A)^2}{4\pi N_A^2 N_B^2} \frac{4(N_A - 1)(N_B - 1)}{4(N_A - 1)(N_B - 1) - N_t} - \frac{L_A L_B}{4(N_A - 1)(N_B - 1) - N_t} \right)^{1/2}, \quad (3.9)$$

where  $N_A$ ,  $N_B$  and  $N_t$  are number of fibers along semi-major axes, semi-minor axes and total number of fibers in an elliptic bundle, respectively. An example of reconstructed woven GDL is reported in Fig. 3.6. For the values of  $N_A = 18$ ,  $N_B = 12$ ,  $L_A \approx L_z/4 = 240 \mu m$ ,  $L_B \approx L_x/4 = l_{GDL}/4 = 100 \mu m$  (taken by analyzing Fig. 3.4 (a-d)), we have obtained  $d = 3.7 \mu m$  and  $r = 3.5 \mu m$ . Hence, for the sake of simplicity,  $d \approx r$  has been assumed in the following calculations. The above few parameters are enough for reconstructing 3D micro-morphology of GDL, because the latter clearly shows some degree of regularity. Due to orthogonality (see the above assumption (i)), 3D reconstruction can be easily done by generating first fibers along  $y$ -direction and consequently generating, in a similar way, the orthogonal fibers along the  $z$ -direction. Concerning the  $y$ -fibers, let us generate first (a) one 2D slice ( $xz$  planes in Fig. 3.5 (a)) at the generic side of the computational box, (b) one 2D slice at the middle and (c) one 2D slice at the opposite side. All remaining slides are created by changing the coordinates of the centers of fiber sections along sinusoidal directrix during the final step (d). Hence let us define the 3D reconstruction algorithm of a woven GDL porous medium according to the following steps:

- Creation of an elliptic bundle of circular fiber sections with a given radius;
- Creation of a 2D slice by merging two elliptic bundles (Fig. 3.5 (a));
- Creation of all 2D slices (including those depicted in Fig. 3.5 (b) and (c)) by shifting the centers of fiber sections along sinusoidal directrix (Fig. 3.5 (d)).

Notice that inside each slice there are two directrices, which are shifted by half wave length;

- Creation of the orthogonal fibers in a similar way and assembly of the reconstructed 3D micro-structure.

Finally, the resulting porosity  $\varepsilon$  of the reconstructed geometry has been compared to the reference values [75, 76]. To this end,  $\varepsilon$  can be calculated as a ratio between the volume occupied by fluid  $V_f$  and the total volume  $V_d$  of the computational domain:

$$\varepsilon = \frac{V_f}{V_d} = \frac{V_d - V_e}{V_d}, \quad (3.10)$$

where  $V_e$  is the volume occupied by obstacles. The total volume of the computational domain is  $V_d = L_x L_y L_z$ , while the volume of fibers in GDL can be calculated using the following expression:

$$V_e = N_b N_t V_{se} = N_b N_t \pi r^2 \int_0^{L_x} \sqrt{1 + f'(x)^2} dx, \quad (3.11)$$

where  $N_b$  and  $N_t$  are the number of bundles in the considered woven geometry and the number of fibers in a single bundle, respectively. According to the assumption (iv),  $f(x) = \sin x$ . As a result, porosity of the reconstructed 3D porous medium is  $\varepsilon = 0.6892$ , for the following set of parameters  $N_b = 4$ ,  $N_t = 400$ ,  $N_y = N_z = 1112$  and  $N_x = 432$ , which is close to the experimental value of  $\varepsilon_{GDL} = 0.7$  (see Table 3.1).

### 3.3 Reconstruction of carbon-supported catalyst layer

The reconstruction procedure of the catalyst layer micro-morphology is different from the one of GDL due to the lack of regularity of such porous medium. In Table 3.1, major parameters of carbon support of catalyst can be found, such as length of the catalyst layer  $l_{CL} = 30 \mu m$  and the average size of carbon particles around  $D_{cp} = 30 - 40 nm$  (these data can also be estimated by analyzing Fig. 3.7 (d) about Vulcan XC-72 in Ref. [80]). Here, we focus on algorithms which can accurately describe the CL morphology (see Fig. 3.7 (a-d)) for a given porosity parameter  $\varepsilon_{CL} = 0.5 - 0.6$  (as reported in the Table 3.1). The first straightforward approach consisted in randomly placing spheres with a fixed radius in

### 3. MORPHOLOGICAL MODEL

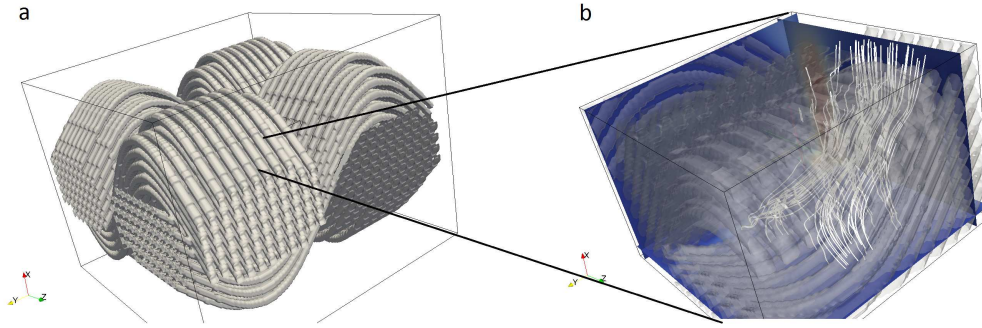


**Figure 3.6:** Geometry of the reconstruction and streamlines of fluid flow through a woven GDL. In order to simplify the visualization, the used parameters, namely  $N_A = 6$ ,  $N_B = 4$ ,  $N_x = 180$  and  $N_y = N_z = 240$ , are coarser than those required by computing permeability [16].

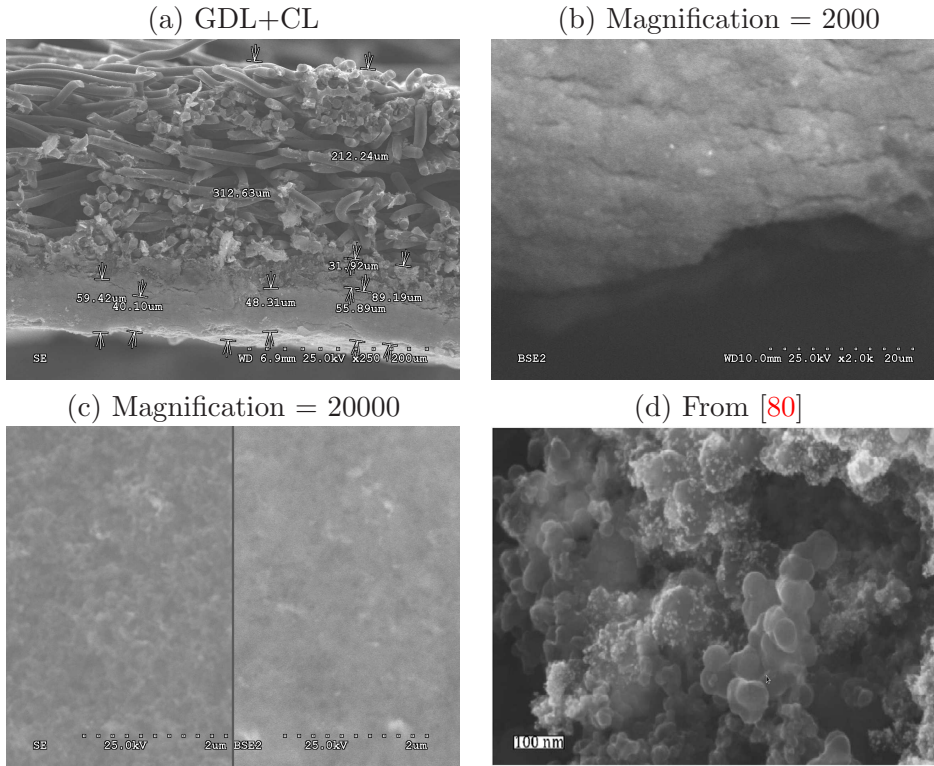


**Figure 3.7:** Micro-structure of the carbon supported catalyst layer Vulcan XC-72. These SEM images, except (d), are obtained in the Institut Charles Gerhardt Universite Montpellier II in the framework of the European FP-7 project 'Automotive Range extender with high TEMperature Improved pemfc meas and Stacks' (ARTEMIS).



the computational domain. To this end, the number of particles  $N_{cp}$  has to be estimated as a function of porosity. In particular, percolation theory [81] predicts that:

$$\varepsilon_{CL} = e^{-nV_{cp}}, \quad (3.12)$$

where  $n$  is the volume concentration of carbon support particles (i.e. spheres), and  $V_{cp}$  the volume of each particle. In our simulation, the computational domain is a cube with edge  $L_x = L_y = L_z = L$  and volume  $V = L^3$ , whereas the volume of a single carbon support particle is  $V_{cp} = \frac{4}{3}\pi R_{cp}^3$  with  $n = N_{cp}/V$  and

$$N_{cp} = \frac{3\ln(1/\varepsilon_{CL})}{4\pi} \left(\frac{L}{R}\right)^3. \quad (3.13)$$

We find out that the above straightforward approach, in the subsequent direct numerical simulations (see Section 3.4), produces a value of permeability of  $k_{single} = 1.07451 \times 10^{-16} m^2$ , namely three orders of magnitude smaller than the real value of permeability  $k_{CL} = 1 \times 10^{-13} m^2$  (see Table 3.1).

The source of a such mismatch lies in the incorrect reconstruction of the catalyst layer. This also confirms that finding a suitable model for micro-morphology is far from trivial. In fact, as it can be seen from the real micro-morphology (see Fig. 3.7 (d)), the assumption of homogeneously distributed particles within the carbon supported catalyst layer is not realistic. A more accurate inspection of real micro-morphology reveals a structure where carbon particles are clustered into groups with some characteristic size  $L_{cluster}^{av}$ . The above mismatch induced us to re-design the algorithm of CL reconstruction, taking into account clusterization of carbon support particles, as well. To this end, CL is assumed to be formed by randomly generated 3D clusters of ellipsoidal shape, containing spherical carbon support particles. For the sake of completeness, below we summarize the adopted assumptions in the modified reconstruction algorithm:

- (i) A simple cluster is an ellipsoid containing spherical carbon support particles;
- (ii) Irregularity of the shape of each cluster is provided by random generation of semi-axes  $A$  and  $B$  of the ellipsoid, while the third semi-axis  $C$  is calculated preserving a fixed average cluster volume;

### 3. MORPHOLOGICAL MODEL

---

- (iii) Each cluster is filled by random deposition of spherical carbon particles inside it;
- (iv) Random orientation of the ellipsoid is obtained by random rotations around the three coordinate axes.

The new algorithm for reconstructing the CL geometry, taking into account all above assumptions, is presented below:

- Random generation of ellipsoid center coordinates  $(x_0^c, y_0^c, z_0^c)$ ;
- Random generation of  $N_{cp}$  coordinates of the centers of spherical carbon particles  $(x_0^i, y_0^i, z_0^i)$  around  $(x_0^c, y_0^c, z_0^c)$ . The number of carbon particles within a single cluster  $N_{cp}$  can be calculated by:

$$N_{cp} \approx \frac{ABC}{R_{cp}^3},$$

where  $R_{cp}$  is an average size of carbon particles. It should be noted that, in order to fulfill assumption (i), only carbon particles whose center satisfies the following inequality are counted:

$$\frac{(x_0^i - x_0^c)^2}{A^2} + \frac{(y_0^i - y_0^c)^2}{B^2} + \frac{(z_0^i - z_0^c)^2}{C^2} \leq 1;$$

- Repetition of above two steps  $N_{cluster}$  times, which can be found using percolation theory and assumption (iii), namely

$$N_{cluster} = \frac{3 \ln(1/\varepsilon_{CL})}{4\pi} \left( \frac{L}{L_{cluster}^{av}} \right)^3. \quad (3.14)$$

The previous refinement of the morphological model of a catalyst layer, based on the degree of clustering, definitely improved the match with experimental permeability (see in details Section 3.4). However, it led to overestimation of real clusterization, which was further improved by redistributing Pt catalyst inside CL (Subsection 4.3.1).

### 3.4 Direct numerical simulation of permeability

For all the following fluid flow simulations, the BGK collisional operator in the LBM solver has been used (see Chapter 2). However, it should be emphasized that this approach, in spite of its simplicity, has some drawbacks, such as the dependence of permeability on relaxation frequencies [55]. In the paper by Pan et al. [55], these effects have been analyzed in detail and it was found that relaxation frequency in the BGK-LBM approach considerably affects the computed permeability. In particular, an increase of relaxation time leads to an approximately linear increase of permeability for the same geometrical configuration of porous medium, which is clearly unphysical. However, this effect almost vanishes for the value of relaxation time  $\tau = 1 l.u.$  (lattice units). This encouraged us to choose the latter value of viscosity in order to increase the accuracy of our computations, instead of considering a more complex collision model as the multiple-relaxation-time (MRT) model [34, 55, 70].

We have applied periodic boundary condition in the  $y$ - and  $z$ -direction, while, along the  $x$ -direction, inlet and outlet pressure difference was applied by imposing  $p_{inlet}$  and  $p_{outlet}$  respectively (see Fig. 3.6). Bounce-back boundary condition has been considered to model no-slip wall boundaries between fluid and solid obstacle (fibers or particles). Permeability  $k$  of porous medium has been computed according to its conventional definition imposing constant pressures at the opposite sides of porous media and using the Darcy's law, namely

$$k = \frac{\rho u v}{\partial p / \partial x}. \quad (3.15)$$

Recalling that the Darcy's law is valid only for laminar flows, we repeated the simulations for excluding any dependence of the computed permeability on the imposed pressure differences and consequently on the mean flow velocity. Therefore, we run each simulation several times at different pressure differences:  $\Delta p = p_{inlet} - p_{outlet} \in [0.0001, 0.0005, 0.005] l.u.$ . For all these values, we obtained the same permeability, which proves that basic assumptions underlying the Darcy's law are indeed valid.



### 3. MORPHOLOGICAL MODEL

#### 3.4.1 Results of fluid simulation for gas diffusion layer

Firstly we have computed the fluid flow through both non-woven and woven fiber-based gas diffusion layer of the HT-PEM, reconstructed as described in the previous Section, in order to evaluate permeability. In the direction orthogonal to the main flow, periodic boundary conditions are applied. Hence, the computational domain consists of one periodic elementary cell of the non-woven or woven structure. All geometrical features of the porous medium (namely radius of cross-section of electrodes  $r$ , distance between neighbor electrodes  $d$ , edges of computational domain  $L_x$ ,  $L_y$ ,  $L_z$ , mesh spacing  $\Delta x$ ) have been re-parametrized by a dimensionless resolution parameter  $n_r$ . In particular, for non-woven GDL we have assumed  $L_y = L_z = 64 n_r \Delta x$  and  $L_x = 32 n_r \Delta x$  and  $r = n_r \Delta x$ , while for woven GDL  $L_y = L_z = 278 n_r \Delta x$  and  $L_x = 108 n_r \Delta x$  and  $r = d = n_r \Delta x$ . Here, it should be noted that for woven GDL the condition  $n_r \geq 3$  is required to have (at least) one fluid node between two neighboring fibers in a bundle. In particular, the following simulation is carried out with  $n_r = 4$  and  $N_t = 400$ . The numerical results for pore-scale fluid flow through the reconstructed GDL are given in Table 3.3. The computed value of permeability, namely  $k_{GDL} = 0.443638 \times 10^{-12} m^2$  and  $k_{GDL} = 2.0991 \times 10^{-12} m^2$ , is in good agreement with the experimental values (see Tables 3.1 and 3.2). It is important to point out that no special tuning was applied in order to achieve these results.

**Table 3.3:** Numerical results of permeability of GDL (*l.u.* stands for lattice units, see [41]).

Non-woven GDL	
Resolution	$256 \times 128 \times 256$
Lattice average velocity	$7.9780 \times 10^{-07} l.u.$
Lattice pressure gradient	$1.5873 \times 10^{-07} l.u.$
Lattice length	$1.75 \times 10^{-06} m$
Actual permeability	$2.0991 \times 10^{-12} m^2$
Woven GDL	
Resolution	$432 \times 1112 \times 1112$
Lattice average velocity	$3.60172 \times 10^{-07} l.u.$
Lattice pressure gradient	$1.16009 \times 10^{-07} l.u.$
Lattice length	$9.259 \times 10^{-07} m$
Actual permeability	$0.443638 \times 10^{-12} m^2$

We notice that a DELL Precision<sup>®</sup> T7500 Linux workstation was not suitable to perform simulation in this case. In fact, in a 32 bit floating-point representation, the single computational node with a  $D3Q19$  lattice requires 76 ( $19 \times 32/8$ ) bytes. The requirement  $n_r \geq 3$  implies at least  $324 \times 834 \times 834 \times 76 \approx 16\text{GB}$  of RAM. Therefore, this simulation has been performed by a small Transtec<sup>®</sup> HPC cluster with 72 total virtual cores, 144 GB total RAM, 5.5 TB total disk capacity (3.0 TB failure free), double networking by both Infiniband and GBit. This cluster has 8 computational nodes with following properties: 2 Quad-core Intel Xeon, 2.33 GHz processors, corresponding to 8 virtual cores; 16 GB RAM, leading to 2 GB/core ratio; 250 GB SATA hard drive, 7200 rpm. The previous simulation for computing permeability with  $n_r = 4$  required the full computational power of the cluster. Detail information about the efficiency of Palabos code for different architecture and number of cores is presented in Refs [82, 83].

#### 3.4.2 Results of fluid simulation for catalyst layer

In this case, a more sophisticated reconstruction of micro-morphology has been developed. The additional computational requirement was fully compensated by relatively less demanding flow simulation. In Table 3.4, the sensitivity of permeability on the cluster size of carbon particles is reported. For all simulations, we used a cubic computational box made of  $N \times N \times N$  nodes and porosity  $\varepsilon_{CL} = 0.5$ . Random deposition of carbon particles, performed using the first straightforward approach (see previous Section about reconstruction), leads to permeability, which is approximately three orders of magnitude smaller than the real value. On the other hand, following the refined approach, clusterization provides a considerable improvement in predicting the real permeability, as far as the optimal value  $L_{cluster}^{av} = 1500\text{ nm}$  is used. Noticeably, this value of clusterization is too high, according to very recent experimental results [33]. The reason is due to the assumption that all catalyst particles deposited on the bottom of CL, which we made for calculation of permeability using conventional approach. While in reality catalyst particles are widespread in CL and the distribution of them considerably affects to mass flow rate (see Subsection 4.3.1).

In Fig. 3.8, the reconstructed geometry and the flow streamlines through the CL porous medium are reported, using both straightforward approach (results

### 3. MORPHOLOGICAL MODEL

**Table 3.4:** Sensitivity of permeability on the cluster size of carbon particles in CL (*l.u.* stands for lattice units, see [41]).

Resolution	$200 \times 200 \times 200$
Average size of cluster	$40 \text{ nm}$
Lattice average velocity	$1.60371 \times 10^{-05} \text{ l.u.}$
Lattice pressure gradient	$2.51256 \times 10^{-06} \text{ l.u.}$
Lattice length	$1.0 \times 10^{-08} \text{ m}$
Actual permeability	$1.07451 \times 10^{-16} \text{ m}^2$
Resolution	$200 \times 200 \times 200$
Average size of cluster	$400 \text{ nm}$
Lattice average velocity	$7.16111 \times 10^{-04} \text{ l.u.}$
Lattice pressure gradient	$2.51256 \times 10^{-06} \text{ l.u.}$
Lattice length	$1.0 \times 10^{-08} \text{ m}$
Actual permeability	$0.47502 \times 10^{-14} \text{ m}^2$
Resolution	$400 \times 400 \times 400$
Average size of cluster	$1500 \text{ nm}$
Lattice average velocity	$1.26456 \times 10^{-04} \text{ l.u.}$
Lattice pressure gradient	$1.25313 \times 10^{-06} \text{ l.u.}$
Lattice length	$5.0 \times 10^{-08} \text{ m}$
Actual permeability	$0.420467 \times 10^{-13} \text{ m}^2$

(a) and (b)) and refined approach taking into account clusterization (results (c) and (d)). A magnification of fluid flow simulation based on the first approach (see Fig. 3.8 (b)) is intended to make more visible the fluid paths: fluid flow is dispersed in the porous medium and hence it is highly reduced because of drag resistance. On the other hand, in the refined approach (see Fig. 3.8 (d)), because carbon clusters are impermeable for fluid, the fluid flow can take advantage of the interstices among clusters.

### 3.5 Gas rarefaction effect

In the previous sections, the continuum-based equations, i.e. incompressible Navier-Stokes equations, were used for solving the pore-scale fluid flow through porous media. However some of the pores have a characteristic size which is comparable with the mean free path of the gas  $\lambda$ , i.e. the average distance traveled by a gas particle between two subsequent collisions. Fluid flow with length scales of the order of the mean free path of fluid particles is characterized by

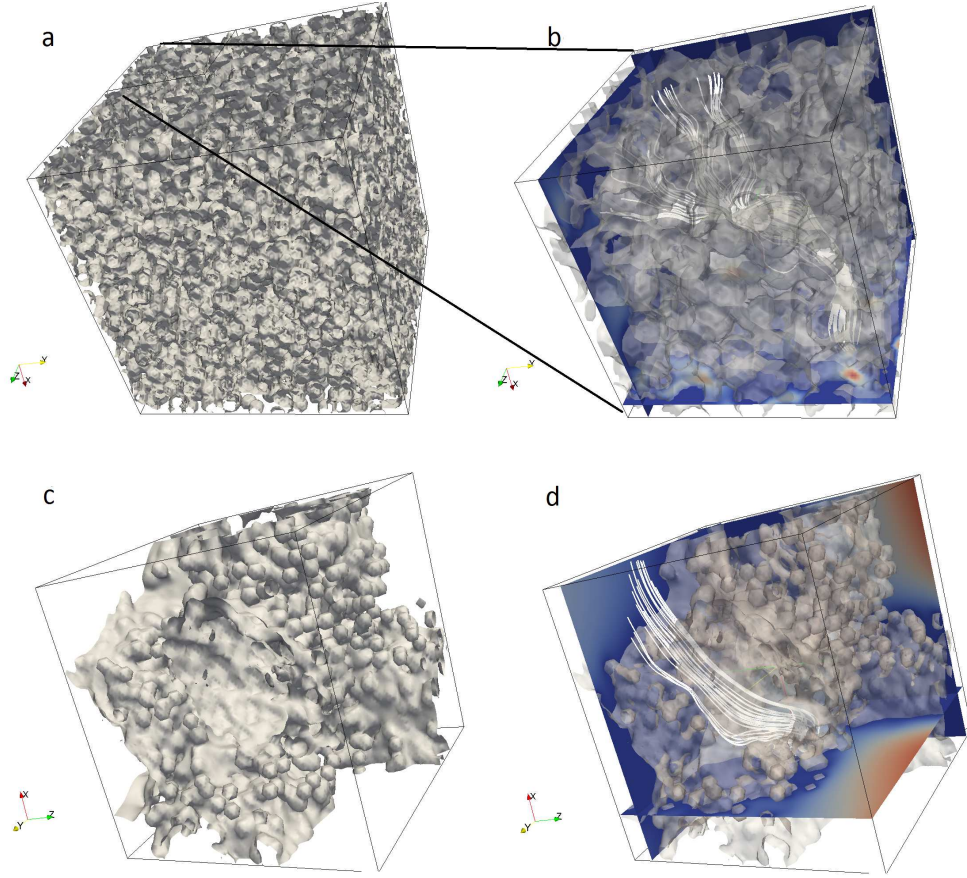


**Figure 3.8:** The geometry and flow streamlines through reconstructed CL porous medium: (a)-(b) the results of the straightforward algorithm; (c)-(d) the results of clusterization one for  $L_{cluster}^{av} = 350 \text{ nm}$  [16].

rarefaction effects which are not properly described by standard hydrodynamics based on continuum equations [86]. Hence, in this section, we investigate on possible rarefaction effects, in order to find out if they may eventually modify in a substantial way the previous permeability estimates and consequently the reliability of reconstructed morphological models.

### 3.5.1 Flow regimes

The fundamental dimensionless number for describing the rarefaction effects is the Knudsen number  $Kn$  [86, 87], defined as the ratio between the mean free path of the gas  $\lambda$  and a macroscopic length  $L_{char}$  describing the flow, e.g. a channel

### 3. MORPHOLOGICAL MODEL

---

width or the diameter of an object exposed to the flow, namely

$$Kn = \frac{\lambda}{L_{char}}. \quad (3.16)$$

The Navier-Stokes equations are applicable only for flows at sufficiently small Knudsen numbers and fail in the description to flows at Knudsen numbers  $Kn > 0.01$  [50, 86, 88]. In particular, depending on the Knudsen number, there are many flow regimes: Continuum flow ( $Kn < 0.01$ ); Slip-flow ( $0.01 < Kn < 0.1$ ); Transient flow ( $0.1 < Kn < 3$ ); Free molecular flow ( $Kn > 3$ ).

In order to estimate the Knudsen number in our simulations, we have to calculate both the mean free paths for the gases involved in electrochemical reactions of the HT-PEM and the characteristic lengths of the considered porous media, i.e. GDL and CL. For the sake of simplicity, let us consider separately the mean free paths of the single components of the reactive mixture in the ideal case, namely hydrogen, oxygen and water vapor. This simplifying assumption will be enough for finding out the relevant order of magnitude. According to the standard theory of ideal gases [89], the mean free path can be computed as

$$\lambda = \frac{1}{\sqrt{2}\pi d^2 n}, \quad (3.17)$$

where  $n$  is the number of molecules per unit volume and  $d$  is the molecular diameter. Moreover, the kinematic viscosity  $\nu$  can be computed by the Maxwell's formula [89], namely

$$\nu = \frac{2}{3\pi d^2 n} \sqrt{\frac{kT}{\pi m}}, \quad (3.18)$$

where  $k = 1.3087 \times 10^{-23} \text{ J/K}$  is the Boltzmann constant,  $T$  is the operating temperature and  $m$  is the mass of the molecule. Combining the previous formulas yields

$$\lambda = \nu \frac{3}{2\sqrt{2}} \sqrt{\frac{\pi m}{kT}}. \quad (3.19)$$

Taking data about transport coefficients from NIST database [90] and using the previous formula given by Eq. (3.19), it is possible to estimate the mean free paths for the gases involved in electrochemical reactions of the HT-PEM, as reported in Table 3.5. The mean free paths under operating conditions of temperature  $T = 423 \text{ K}$  and pressure  $P = 101325 \text{ Pa}$  are  $159 \text{ nm}$ ,  $270 \text{ nm}$  and  $113 \text{ nm}$  for

**Table 3.5:** Estimation of mean free paths for the gases involved in electrochemical reactions of the HT-PEM. Operating temperature  $T = 423 \text{ K}$  and pressure  $P = 101325 \text{ Pa}$ . Data taken from Ref. [90].

	Oxygen	Hydrogen	Water (vapor)
Molecular weight	$0.032 \text{ kg/mol}$	$0.002 \text{ kg/mol}$	$0.018 \text{ kg/mol}$
Molecular mass	$5.314 \times 10^{-26} \text{ kg}$	$3.321 \times 10^{-27} \text{ kg}$	$2.989 \times 10^{-26} \text{ kg}$
Dynamic viscosity	$2.67 \times 10^{-05} \text{ Pa s}$	$1.13 \times 10^{-05} \text{ Pa s}$	$1.42 \times 10^{-05} \text{ Pa s}$
Density	$0.973 \text{ kg/m}^3$	$0.061 \text{ kg/m}^3$	$0.547 \text{ kg/m}^3$
Kinematic viscosity	$2.75 \times 10^{-05} \text{ m}^2/\text{s}$	$1.86 \times 10^{-04} \text{ m}^2/\text{s}$	$2.60 \times 10^{-05} \text{ m}^2/\text{s}$
Mean free path $\lambda$	$159 \text{ nm}$	$270 \text{ nm}$	$113 \text{ nm}$

oxygen, hydrogen and water (vapor), respectively. In the following calculations, the mean free path of hydrogen will be used in order to check the sensitivity of the computed permeabilities with regards to the highest Knudsen number.

Concerning the characteristic lengths of the considered porous media, we propose the following simplified procedure. The pressure gradient through a straight capillary is given by the standard Hagen-Poiseuille equation [63], namely

$$\left. \frac{\partial P}{\partial x} \right|_{HP} = -\frac{32\mu u}{L_{char}^2}, \quad (3.20)$$

where, in this case,  $L_{char}$  is the capillary diameter. The previous formula can be generalized in case of porous media [91] in the following way

$$\frac{\partial P}{\partial x} = \left. \frac{\partial P}{\partial x} \right|_{HP} \frac{h'/h}{\varepsilon} = -\frac{32\mu u}{L_{char}^2} \frac{h'/h}{\varepsilon}, \quad (3.21)$$

where  $h$  is the straight path (minimum length) through the porous medium and  $h'$  the actual path. Sometimes the ratio  $h'/h$  is called tortuosity in the literature on porous media [91]. A typical value of  $h'/h = 5/2$  is often encountered dealing with fuel cells and this is in good agreement with direct numerical simulations of fluid flow in fuel cell electrodes [46]. Assuming  $h'/h = 5/2$  and combining the previous equation with the Darcy's law given by Eq. (2.22) yields

$$L_{char} = \sqrt{\frac{80k}{\varepsilon}}, \quad (3.22)$$

where  $k$  is the permeability of the porous medium computed with no-slip boundary conditions, i.e. without rarefaction effects.

### 3. MORPHOLOGICAL MODEL

---

#### 3.5.2 Estimation of maximum gas rarefaction effect on permeability

In order to calculate how rarefaction affects the permeability, we use the results of a previous study about pressure-driven flow through a microchannel [92]. In Ref. [92], the two-dimensional isothermal flow in case of low Mach number  $Ma \ll 1$  and moderate Knudsen number  $Kn \leq 0.15$  is analyzed by using the Navier-Stokes equations with a first-order slip-velocity boundary condition. In particular, by means of a perturbation expansion in the height-to-length ratio of the channel and using the ideal gas equation of state, the zeroth-order analytic solution for the stream-wise mass flow rate is derived. In the original Ref. [92], the stream-wise mass flow rate is expressed in terms of the two-dimensional Knudsen number  $Kn_H = \lambda/H$  where  $H$  is the channel height. The channel height  $H$  is actually half of the hydraulic diameter, which is the proper characteristic quantity for describing both two- and three-dimensional flows, i.e.  $H = L_{char}/2$ . Consequently  $Kn_H = 2Kn$  where  $Kn = \lambda/L_{char}$  as usual in the present paper. Taking into account this generalization for three-dimensional flows and recalling Eq. (2.22), the original formula for the stream-wise mass flow rate can be used for deriving an expression of permeability correction as a function of  $Kn$ , namely

$$\frac{k_{slip}}{k_{no-slip}} = 1 + \frac{24 \sigma Kn}{1 + \mathcal{P}}, \quad (3.23)$$

where  $k_{slip}$  is the permeability taking into account the rarefaction effects,  $k_{no-slip}$  is the permeability computed as in the previous subsections,  $\sigma$  is the momentum accommodation coefficient, which depends on the properties of porous medium (for engineering calculation usually  $\sigma = 1$ ) and  $\mathcal{P}$  is the ratio between inlet and outlet pressure, i.e.  $P_{inlet}/P_{outlet} \geq 1$ . In deriving both numerical results for a woven GDL, reported in Table 3.3, and those for CL, reported in Table 3.4, a pressure ratio equal to  $\mathcal{P} = 1.0005$  was used.

The previous expression represents the last ingredient for taking into account the rarefaction effects. The proposed simplified procedure is the following: By Eq. (3.22), the characteristic length  $L_{char}$  is derived for a given porous medium with an already computed no-slip permeability; Consequently the Knudsen number  $Kn = \lambda/L_{char}$  is computed; Finally, by Eq. (3.23), the permeability correction, i.e.  $k_{slip}/k_{no-slip}$ , is computed and allows one to derive the refined estimate of permeability, accounting for rarefaction effects. In Table 3.6 an estimate



of the rarefaction effects on the calculation of permeability for both GDL and CL is presented for hydrogen (having the highest Knudsen number, as reported in Table 3.5). Clearly, according to these precautionary estimates, the rarefac-

**Table 3.6:** Estimate of rarefaction effects for hydrogen gas flow, with mean free path  $\lambda = 270\text{ nm}$  (see Table 3.5), through GDL and CL.

Layer	$\varepsilon$	$k_{no-slip}$	$L_{char}$	$Kn$	$k_{slip}/k_{no-slip}$
GDL	0.7	$0.443638 \times 10^{-12} m^2$	$7.12 \times 10^{-6} m$	0.038	1.455
CL	0.5	$0.420467 \times 10^{-13} m^2$	$2.59 \times 10^{-6} m$	0.104	2.249

tion effects are not negligible in general for the present porous media. These estimates are the highest expected deviations from the results reported in the previous subsections. However it is worth the effort to point out that, even in the worst case, i.e. a permeability increase of a factor of two for CL, the latter is still quite smaller than the dependency of predicted permeability on the underlying morphological model. In fact, in Table 3.4, changing the average size of cluster from  $400\text{ nm}$  to  $1500\text{ nm}$  leads to an increase of the permeability of one order of magnitude (five times the previous maximum rarefaction effect). Moreover, taking  $k_{no-slip} = 0.420467 \times 10^{-13} m^2$  from the last row of Table 3.4 and multiplying it by  $k_{slip}/k_{no-slip} = 2.249$  leads to an effective permeability of  $k_{slip} = 0.945567 \times 10^{-13} m^2$ , which is pretty close to  $1 \times 10^{-13} m^2$  reported in Table 3.1. Hence the developed morphological models can be considered robust against rarefaction effects.

### 3.6 Conclusion

In this chapter the morphological models for the electrodes of HTPMFEC are developed. Reliable algorithms are proposed to reconstruct complex micro-morphology. Two kinds state-of-the-art fiber-based gas diffusion layers with regular (woven) and stochastic (non-woven) behaviors are considered. More sophisticated morphological model with additional tunable parameters of such as clusterization or agglomeration size, distribution of catalyst etc, is developed for carbon supported catalyst layer. It should be emphasized, the results of reconstruction using both the approach proposed in this chapter (see the figures) and GeoDict



### 3. MORPHOLOGICAL MODEL

---

(see Figure 2 (a) in Ref. [84]) are in good qualitative agreement. However, even though some basic ideas of GeoDict reconstruction are reported in literature [85], it is not always possible to collect enough details in order to perform a complete comparison with other methods. Moreover, there is no GeoDict specific module for reconstruction of the catalyst layer, which is our main focus here. In particular, an open and a flexible algorithm for CL reconstruction, as the one proposed in this thesis, can be easily extended by considering also catalyst particles and their optimized distribution. The latter issue is essential for mitigating specific degradation mechanisms and improving cell performances.

Gas rarefaction effects on the value of permeability are considered by properly post-processing the numerical results, which are found to be not negligible in general for the porous electrodes of HTPEMFC. It is found that the highest influence of rarefaction could be expected for hydrogen the catalyst layer.

The morphological model proposed in this chapter allows one to explain how macroscopic transport coefficients are sensitive to different features of microstructure, like carbon support clustering and catalyst distribution. The latter point is very relevant also for analyzing three dimensional morphology by tomography. In fact, computing permeability of tomography microstructure by assuming catalyst on the bottom side would lead to inaccurate results, in spite of the accuracy on the geometry. This proves that any input data about morphology must be interpreted by a morphological model.

To this end, these morphological models of the electrodes are used in the next chapter 4 to explain sensitivity of macroscopic transport coefficients on different features of microstructure, and also to apply the designing strategies in order to increase PEMFC performance and to mitigate degradation phenomena by improving mass transport processes.

## 4

# Degradation of the High Temperature Polymeric Electrolyte Fuel Cells

## 4.1 Introduction

The morphological models proposed in the previous chapter 3 allows one to explain not only sensitivity of macroscopic transport coefficients on different features of microstructure, but also may be useful for designing strategies in order to increase PEMFC performance and to mitigate degradation phenomena by improving mass transport processes. Taking advantage of this, in this chapter, a new design strategy of carbon supported catalyst layer with improved confinement of phosphoric acid inside the fuel cell membrane electrode assembly is introduced. Chapter starts with the literature review of major degradation processes of a fuel cell based on proton exchange membrane. The special focus is made on the specific degradation of high temperature PBI-based PA-doped fuel cell, this is phosphoric acid depletion from catalyst layer and membrane. In addition, a theoretical estimation of the effect of this strategy on the mitigation of fuel cell degradation due to phosphoric acid loss is done.

As it is well known, one of the main issues limiting the widespread adoption and successful commercialization of polymer-electrolyte fuel cells, especially for automotive applications, are those of lifetime or durability, under various operating conditions, and cost. Although the number of installed units around the world continues to increase and dominates the pre-markets, the present lifetime

#### 4. DEGRADATION OF THE HIGH TEMPERATURE POLYMERIC ELECTROLYTE FUEL CELLS

---

requirements for fuel cells cannot be guaranteed. This fact stimulates research for a more comprehensive knowledge of the material aging mechanisms.

Insight into the mechanisms which lead to a reversible or irreversible loss of cell performance and the interaction of these mechanisms with the operating conditions is required. This should be based on the observation of the changes in materials properties. The impact on fuel cell performance is required, before either fuel cell materials can be optimized further with respect to their durability or systems controls and operating procedures can be optimized to prevent the most detrimental conditions. Modeling of different degradation aspects can help to highlight above stressed points by understanding the key reasons and fundamental physical phenomena for particular degradation mechanisms and by predicting the impact of these degradation effects. Another important issue of modeling is understanding the interaction between different specific membrane degradation mechanisms and their complex and mixed effects due to their simultaneously occurrence in real fuel cell operation. This requires multi-scale analysis of undergoing phenomena. This has motivated several recent studies on modeling of PEMFC degradation using data of long-term testing as well as rapid aging testing. It should be noted that modeling has been restricted mainly to the LTPEMFC. However these investigations are of great interest also for high temperature PEMFCs, due to the fact that many degradation mechanisms are actually inherited from the low temperature counterpart [17].

Although, all parts of a hydrogen fuel cell are subject to degradation processes, the membrane electrode assembly is commonly considered as the heart of the system and most vulnerable to degradation processes. Generally, MEA consists with the following compartments: electrodes (gas diffusive layers (GDL), catalyst layers (CL)) and membrane. Especially, the degradation of the noble metal catalysts in the MEAs at the so-called three-phase-boundary (TPB) [18, 19, 20] is a key factor directly influencing the durability of the fuel cells. Fig. 4.1 shows the links between degradation processes and operating conditions for transport application. As can be seen, there are actually two major degradations, namely carbon corrosion and phosphoric acid depletion. These two degradations are considered in details below.

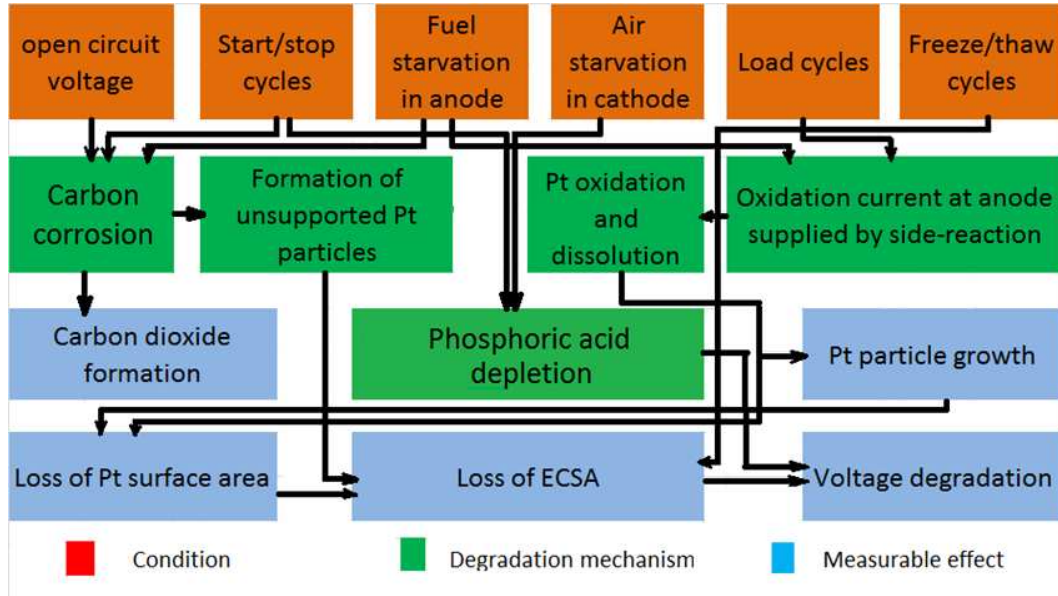


**Figure 4.1:** Schematic representation of connection between main degradation processes and fuel cell operating conditions for transportation application.

#### 4.1.1 Degradation of membrane

There are two main degradation modes related to the membrane, which are (a) membrane thinning leading to a possible pinhole formation and (b) increased fuel crossover and loss of fuel efficiency by acid evaporation [21]. It was shown that phosphoric acid loss from the membrane is insignificant at 160 °C [21, 22]. Excessive compression of MEA causes membrane creep and thinning manifested by gas crossover increase and by the decrease of the membrane resistance. Probably the most modeled failure process is pinhole formation in membrane due to membrane degradation by chemical attack of peroxide [93, 94, 95]. Indeed, there are two pathways for the generation of free radical species from hydrogen peroxide. Firstly, generation at the cathode due to the electrochemical two-electron reduction of oxygen [96], and secondly, generation at the anode owing to chemical combination of crossover oxygen and hydrogen at the anode [97, 98, 99]. Several groups [100, 101] worked to find a link between crossover of reagents and membrane degradation. Namely, authors studied the effect of the presence of platinum on degradation of ionomer membranes in hydrogen/air mixtures. Few stochastic degradation models have been proposed in Ref. [102] to predict deterioration

of different fuel cell properties by time regardless details of degradation modes. Some attempts have been made to model the chemical degradation processes using semi-empirical transient approach [100, 103]. It includes an equation for the residual ionomer mass in the cathode catalyst layer, which was assumed to be directly proportional to the rate of hydrogen crossover, predicated on the assumption that radical species are produced at the cathode catalyst layer/membrane interface. The thickness of the membrane was assumed to decrease as a linear function of the residual ionomer mass, which impacted on the calculation of the uniform hydrogen crossover flux. However, the influence of the operating conditions could not be accounted for in this simple model.

### 4.1.2 Degradation of electrodes

There are several degradation mechanisms of the high temperature MEA electrodes. The loss of catalyst metal (platinum) electrochemically active surface area (ECSA) by particle size growth is considered to be a major cause of the decay in the FC performance. The mechanisms thought to lead to this loss are:

- i) Carbon support corrosion leading to loss of nanoparticle electrical contact [104];
- ii) Particle migration and coalescence (leading to coarsening) [104, 105];
- iii) Particle dissolution and re-precipitation off support (leading to mass loss);
- iv) Particle dissolution and re-precipitation on support (leading to coarsening) [106].

It is also possible that coarsening could occur through diffusion of platinum atoms on the carbon support.

In terms of modeling, some efforts have been done on the dissolution mechanism of platinum [107, 108] and on platinum migration using dilute solution equations. The mathematical model presented in Ref. [109] incorporates the kinetic expressions for platinum oxidation and dissolution into a transient, one-dimensional model of the cross section of a PEM fuel cell consists with following regions: anode gas-diffusion medium, anode catalyst layer, membrane, cathode

catalyst layer, and cathode gas-diffusion medium. Porous-electrode theory is used to model the anode and cathode catalyst layers. The details of sintering, ripening and the reaction of platinum with hydrogen were ignored. Platinum ion transport by the bulk flow of liquid water was assumed to be negligible. A refinement of this model has been done in Ref. [110], where particle size distribution and crossover hydrogen are explicitly included. The oxidation model has been extensively modified, and a model for particle surface tension as a function of oxide coverage has been included.

In fact, the dissolution process of platinum particles is exacerbated or even initiated by another major degradation process during fuel cell operation, namely carbon support corrosion, which is a potential-dependent electrochemical process [111, 112, 113]. Corrosion of carbon support at the cathode catalyst results in electrical isolation of the catalyst particles, migration on the surface of the support material and agglomeration via Ostwald ripening mechanism [112]. Meanwhile, it increases the hydrophilicity of the cathodic catalyst layer, accompanying with the electrolyte flooding which leads to an increase of the cathode mass transport overpotentials. The mass transport overpotential is responsible for diffusive transport of the reactants to the electrode surface from bulk electrolyte and reverse transport of products. As a result, the oxygen reduction reaction kinetics decreases in the cathode. Concomitant with the corrosion of the carbon, thinning of the catalyst layer and loss of its void volume can be observed [114]. In the worst case, complete degradation of carbon support might finally affect structural integrity of the cathode catalyst layer. Noticeable, carbon corrosion process is a function of not only temperature and local potential, but also water partial pressure [17, 112, 115].

Probably the first attempt on modeling of this process has been done in paper [116] proposing a one-dimensional static model for the calculation of the potential profiles when the anode is partially exposed to air. Authors have proposed a reverse-current decay mechanism in which carbon corrosion occurs due to inadequate fuel quantities and possible crossover during startup and shut-down. A numerical finite element method is used for find a solution of a Poisson equation coupled with a conservation equation of the electric charges and a classic Butler-Volmer description of the global hydrogen oxidation reaction (HOR)

and oxygen reduction reaction (ORR). Meyers and Darling [117] have proposed a similar model, which describes how a maldistribution of hydrogen across the fuel electrode can induce both oxygen permeation from the cathode to the anode and cathode carbon corrosion in the fuel starved region. Implications of this reverse current mechanism are explored by simulating a cell with a nonuniform distribution of hydrogen along the fuel channel in both steady-state and transient operation. The mathematical model is a one-dimensional (1D) representation taking into account the reactants transported in the channels and the Butler-Volmer equations. It should be stressed out that above mentioned models describe how operating conditions affect carbon corrosion, but do not describe the impact of carbon corrosion on instantaneous performance. The instantaneous feedback between performance and aging is not taken into account. Furthermore, the role of the catalyst in the carbon corrosion is not explored (platinum and carbon are treated as a individual single phases). These lacks on investigation has been partially covered in Ref. [104]. The proposed mechanistic model couples carbon corrosion with MEA electrocatalysis, which describes instantaneous cell performance. Additionally, the effects of operating conditions and catalyst layer parameters on lifetime of fuel cell have been estimated. Particularly, it was found that in the presence of oxygen in anode compartment due to crossover or fuel starvation the thickness of cathode catalyst layer decreases. One of the main results of this work is the existence of a maximal durability for a given external load.

## 4.2 Phosphoric acid loss

In contrast to the above mentioned degradations, loss of phosphoric acid from membrane and electrodes is a peculiar degradation phenomenon of high temperature PBI-based phosphoric acid doped PEMFC. The acidic environment of the fuel cell, combined with the humidity level and temperature, creates a harsh environment for the components of the fuel cell. PA loss is thought to be one of the major mechanisms of degradation, especially in high current density and elevated temperature ( $> 160^{\circ}\text{C}$ ) [2], through different mechanisms. Basically, these

are the following mechanisms through which PA loss may occur: capillary transport, diffusion, membrane compression, evaporation and leaching by condensed water during shutdown and cold start. Yu et al. [22] conducted steady-state operation tests (with constant current density  $0.2\text{ A/cm}^2$ ) and dynamic durability tests (load, thermal, and shutdown/start-up cycling tests, with operational conditions which may be found in real applications) where the fuel cell potential and phosphoric acid loss were recorded over thousands of hours. It was found that higher acid loss rate corresponds to the cathode side of MEA, due to the formation of liquid water, and subsequent an extra mechanism of PA loss, namely acid leaching. A significant increase in the PA loss rates and the voltage degradation were observed at the elevated temperatures (180 and 190°C) and high load conditions. It was concluded that degradation due to phosphoric acid loss appears to be a minor factor of fuel cell failure, compared with degradation caused by catalyst activity loss, during the first hours of continuous operation. However, after the first period, the platinum particles size tended to stabilize and the effect of phosphoric acid loss started to emerge [118].

Deep insight into this degradation mechanism, leading to irreversible or reversible performance loss and the relation with other degradation mechanisms and the operating conditions, comes through pore-scale modeling of the mass transport phenomena, which provides the detailed information available at the microscopic scale. The morphological model presented in [16] was developed as the first step towards modeling of such degradation mechanisms at pore scale. This morphological model does allow one to extrapolate the specific results towards different materials. On the other hand, a morphological model correlates the transport coefficients with the global microscopic structure, but it also (a) explains how different features of the microscopic structure (characteristic lengths, distributions, shapes, orientations, clustering, etc.) determine independently the transport coefficients and (b) suggests design strategies to improve transport coefficients. Hence a morphological model allows one to generate many virtual structures (all compatible with experimental data with regards to some features) in order to find out a design strategy beyond experimental measurements. Here we aim to extend further this model towards understanding degradation phenomena.



### 4.3 Mitigation

#### 4.3.1 Effects of platinum particle distribution in catalyst layer

In this section, we explore some catalyst layer configurations by tuning the distribution of the catalyst Pt particles. The goal is twofold. First of all, the assumption of placing all catalyst Pt particles at the interface between CL and membrane is not realistic (even though imposing constant pressures at the opposite sides of porous media is the standard way to compute permeability according to its conventional definition). The reason is that conventional definition of permeability (see Eq. (3.15)) does not rigorously apply to CL, where electrochemical reactions happen inside the layer itself. The conventional definition may lead to an underestimation of the effective pressure gradient and consequently an overestimation of the particle clustering, in order to recover the same experimental permeability (as in Section 3.3). This is why, in the calculations a particle clustering is found to be higher than what it should be, according to some very recent tomography data [33]. More specifically, it should be noted that Darcy's law for permeability calculation assumes that all sink nodes (Pt particles) are deposited at the domain bottom side. However, in real systems, catalyst particles are spread homogeneously inside catalyst layer, where the electrochemical reactions take place. Hence the real partial pressure gradient due to electrochemical reactions is actually smaller than the simulated one. In this section, the sensitivity of numerical results on this assumption is explored. Secondly, the catalyst particle distribution should be optimized in order to improve the performance of the PEMFCs and also to mitigate degradation mechanisms (e.g. loss of phosphoric acid). Optimal functionalization of catalyst layer can be achieved by proper tuning mass transport properties of CL microstructure with regards to transport of reactant (hydrogen, oxygen) and product gases (water vapour). In this stage, the role of the proposed morphological model is essential. From the morphological point of view, it is important to have small platinum particles with large surface area, finely dispersed on the catalyst support surface (typically carbon powders). Large amount of work has been done during last years to decrease the platinum loading on the catalyst layer, using advanced catalyst deposition techniques or

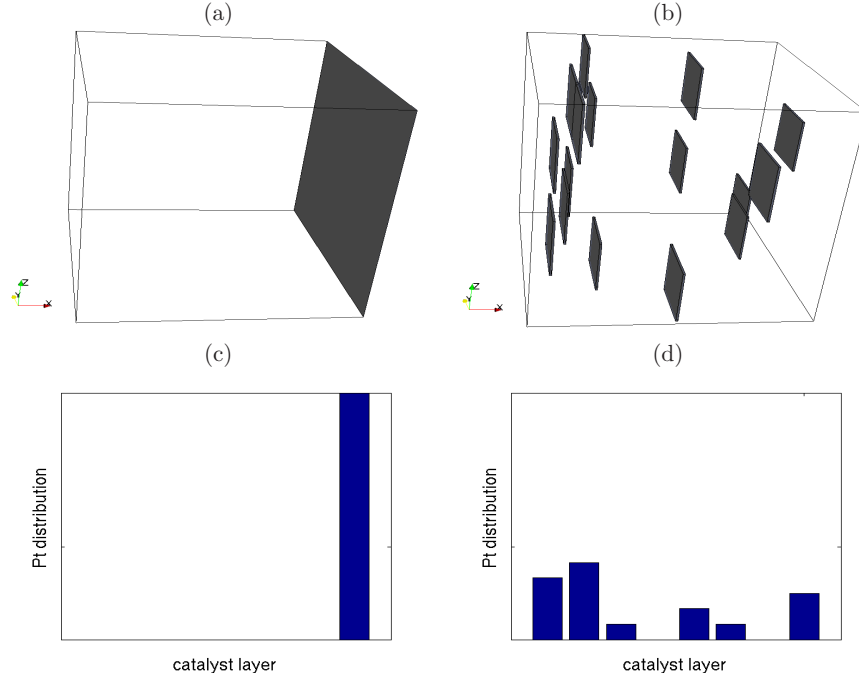


**Figure 4.2:** Two considered (a-b) locations and (c-d) corresponding deposition distribution of Pt particles inside the catalyst layer.

promoting platinum alloys with other metals, e.g. Pt-Ru, Pt-Sn, Pt-Cr. However mainly the fraction of Pt particles on the carbon support of PBI-based high temperature PEMFC has been considered so far. Thus, electrodes with different platinum percentages on the carbon support, but with the same PBI content normalized with respect to the C/PBI weight ratio ( $C/PBI = 20$ ), have been treated and optimal weight ratio has been found [15].

The influence of Pt deposition on the mass flow rate through the same porous medium is investigated in this section. We slightly extended the previous model for reconstruction of CL microstructure by introducing a new discrete value in Eq. (3.1) for one dimensional array describing the geometry. For example, let us assume  $\mathcal{M} = 3$  for Pt catalyst particles in catalyst layer, namely

$$\mathcal{M}_{i_x, i_y, i_z} = \begin{cases} 0 & (i_x, i_y, i_z) \in fluid \\ 1 & (i_x, i_y, i_z) \in fluid \cap solid \\ 2 & (i_x, i_y, i_z) \in solid \\ 3 & (i_x, i_y, i_z) \in catalyst\ particles \end{cases} \quad (4.1)$$

For comparison, we considered two simulation setups illustrated in Fig. 4.2 (a)

#### 4. DEGRADATION OF THE HIGH TEMPERATURE POLYMERIC ELECTROLYTE FUEL CELLS

---

and (b), where the same amount of catalyst particles is used, but by different distributions reported in Fig. 4.2 (c) and (d). In particular, the former distribution is the conventional one used to compute permeability by Darcy's law, while the latter has been obtained by redistributing platinum particles inside the catalyst layer.

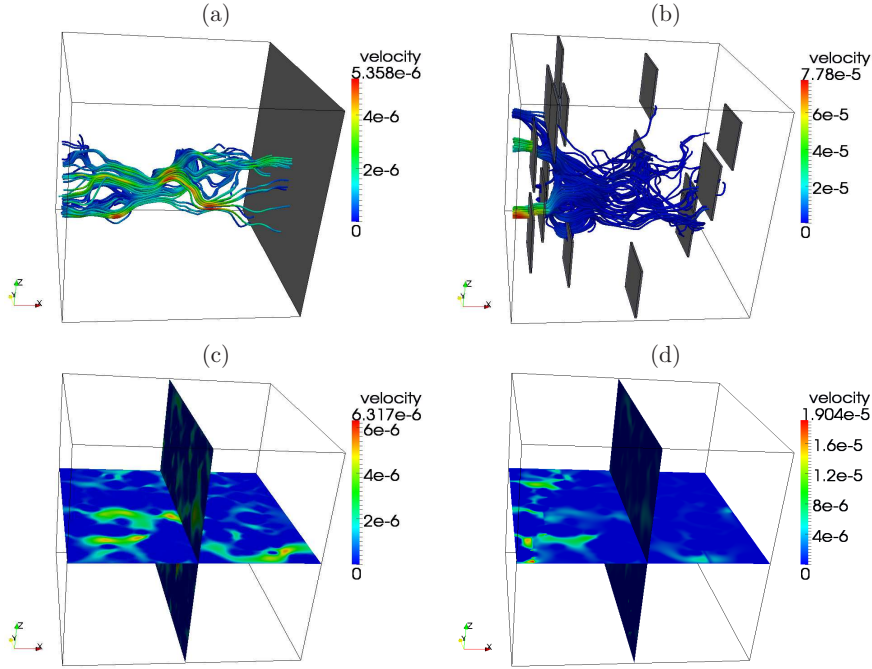


**Figure 4.3:** (a-b) Pt deposition and flow streamlines (c-d) slices of corresponding flow velocity

Pore-scale simulations using BGK lattice Boltzmann method were performed for catalyst layers with clusterization equal to  $L_{av} = 1500nm$  and with the previous Pt deposition distributions. It should be noted, for the all simulation the imposed pressure value at catalyst nodes was taken very small in order to be sure that flow is indeed laminar. In Table 4.1, the parameters of porous medium, computational domain, lattice Boltzmann method and the mass flow rate at the inlet are reported. As it can be seen from the table, we have approximately an order of magnitude increase in flow rate by redistributing Pt particles. Mean velocity and flow rate change (see Fig. 4.3 (c-d)), but also fluid flow streamlines change (see Fig. 4.3 (a-b)). This means that there are quantitative changes (scale

factor), but also qualitative changes in the flow field. Thus, redistribution of catalyst particles inside the microstructure leads to considerable increase of mass flow rate and it provides an additional tunable parameter of the morphological model.

**Table 4.1:** Simulation results and comparison.

Name	Non-distributed	Distributed
Average size of clusters	1500 <i>nm</i>	1500 <i>nm</i>
Relaxation frequency	1.1 <i>l.u.</i>	1.1 <i>l.u.</i>
Lattice viscosity	0.136364 <i>l.u.</i>	0.136364 <i>l.u.</i>
$\Delta P$	$1.0 \times 10^{-5}$ <i>l.u.</i>	$1.0 \times 10^{-5}$ <i>l.u.</i>
Domain size	$128 \times 128 \times 128$	$128 \times 128 \times 128$
Flow rate	$3.06678 \times 10^{-7}$ <i>l.u.</i>	$2.22284 \times 10^{-6}$ <i>l.u.</i>

#### 4.3.2 Innovative idea

In the previous section, we investigate how a parameter of a morphological model, namely distribution of catalyst (platinum) particles, can affect gas dynamics, electro-chemistry and consequently performance in high temperature proton exchange membrane (HT-PEM) fuel cells. These results allow one to propose useful designing strategies in order to increase PEMFC performance and to mitigate degradation phenomena, like the phosphoric acid loss and the crossover of reagents through membrane, by improving mass transport processes.

The main idea behind the mitigation strategy is to design the optimal flow field through the catalyst layer by different setups of morphological parameters, like distribution of catalyst particles, clusterization and so on. Because the velocity gradient  $\partial u_x / \partial x$  orthogonal to the interface is directly related to the pulling stress acting  $\tau_x$  on the phosphoric acid inside the membrane, we force it to be equal to zero at the interface between the catalyst layer and the membrane. Thus, the primary quantity of interest as a result of simulations is velocity  $\mathbf{u}$  component along fluid flow direction, owing to proportionality of pulling stress  $\tau$  acting to phosphoric acid by gases to the velocity gradient. As larger is this stress the force acting to phosphoric acid becomes larger, consequently larger is  $j_{PA}$ , phosphoric acid loss, through diffusion and capillary transport mechanisms. In other words,

#### 4. DEGRADATION OF THE HIGH TEMPERATURE POLYMERIC ELECTROLYTE FUEL CELLS

---

there is direct relation between degradation of fuel cell caused by phosphoric acid loss from membrane and velocity gradient of the flow at the CL/membrane interface ( $x_{cl} = 1$ ).

$$j_{PA} \propto \tau_x = -\mu \left. \frac{\partial u}{\partial x} \right|_{x_{cl}=1} \quad (4.2)$$

An optimal distribution of the catalyst inside CL changes flow field in such a way that not only velocity, but also its gradient is equal to zero at the interface between CL and membrane.

$$\begin{aligned} u|_{x_{cl}=1} &= 0; \\ \left. \frac{\partial u}{\partial x} \right|_{x_{cl}=1} &= 0; \\ j_{PA} \propto \tau_x = -\mu \left. \frac{\partial u}{\partial x} \right|_{x_{cl}=1} &= 0. \end{aligned} \quad (4.3)$$

This is thought to prevent phosphoric acid loss from membrane and catalyst layer itself due to fluid stress and reagents crossover through membrane.

##### 4.3.3 Theoretical estimation for pulling stress

This section represents a theoretical derivation of the relation between morphological parameters, this is the distribution of catalyst particles inside porous catalyst layer, and the velocity component of flow field. The following main assumption are made: (i) the fluid is one species single phase; (ii) the flow is incompressible; (iii) distribution of catalyst is homogeneous except the the main flow direction (towards membrane); (iv) the activity of catalyst does not depends on location. The final goal of this theoretical analysis is to provide a tool to estimate how different choices of distribution function for catalyst can reduce pulling stress on phosphoric acid in the polymer membrane.

This analysis starts with the continuity equation for incompressible flow, like:

$$\nabla \cdot (\rho \mathbf{u}) = S_m, \quad (4.4)$$

where  $S_m$  is source/sink term.

This equation has to be integrated in order to find the expression for the velocity profile. Let us consider infinitesimally small volume of the system. This extracted

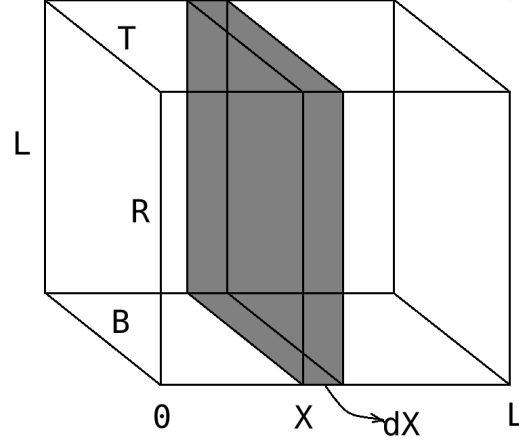


**Figure 4.4:** Considered elementary volume.

$\Delta\Omega \ll \Omega$  volume in Fig. 4.4 is  $\Delta\Omega = A dx$  with surface area  $\delta\Delta\Omega = \Delta A_T + \Delta A_B + \Delta A_L + \Delta A_R + A_x + A_{x+dx}$ .

Integration of this equation (4.4), over this elementary volume yields:

$$\int_{\Delta\Omega} \nabla \cdot (\rho \mathbf{u}) dV = \int_{\Delta\Omega} S_m dV \quad (4.5)$$

Applying Gauss theorem to the left hand side of above equation implies:

$$\int_{\Delta A_T} \rho \mathbf{u} \cdot \mathbf{n} dA + \int_{\Delta A_B} \rho \mathbf{u} \cdot \mathbf{n} dA + \int_{\Delta A_L} \rho \mathbf{u} \cdot \mathbf{n} dA + \int_{\Delta A_R} \rho \mathbf{u} \cdot \mathbf{n} dA + \int_{A_x} \rho \mathbf{u} \cdot \mathbf{n} dA + \int_{A_{x+dx}} \rho \mathbf{u} \cdot \mathbf{n} dA = \int_{\Delta\Omega} S_m dV \quad (4.6)$$

It should be noted that in order to be relevant with realistic system, periodic boundary condition has to be implemented at all lateral sides of a porous catalyst layer (see Fig. 4.5 left). This implies the following, for instance, if there is an incoming flow to left side  $\int_{\Delta A_L} \rho \mathbf{u} \cdot \mathbf{n} dA < 0$  then the same flow has to go out from right side  $\int_{\Delta A_R} \rho \mathbf{u} \cdot \mathbf{n} dA > 0$  in order to satisfy periodicity. On the other word the following relation is true:

$$\int_{\Delta A_R} \rho \mathbf{u} \cdot \mathbf{n} dA + \int_{\Delta A_L} \rho \mathbf{u} \cdot \mathbf{n} dA = 0 \quad (4.7)$$

#### 4. DEGRADATION OF THE HIGH TEMPERATURE POLYMERIC ELECTROLYTE FUEL CELLS

---

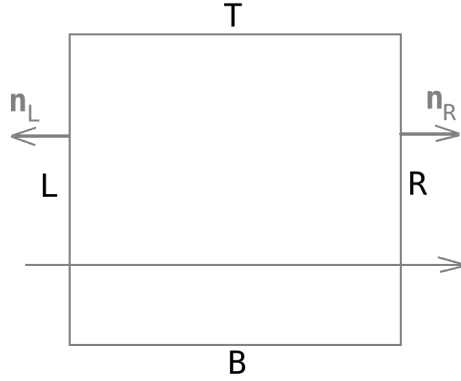


**Figure 4.5:** Periodicity.

The same idea is valid for other sides, namely for the top and the bottom sides.

$$\int_{\Delta A_T} \rho \mathbf{u} \cdot \mathbf{n} dA + \int_{\Delta A_B} \rho \mathbf{u} \cdot \mathbf{n} dA = 0 \quad (4.8)$$

Substituting these into Eq. (4.6) yields:

$$\int_{A_x} \rho \mathbf{u} \cdot \mathbf{n} dA + \int_{A_{x+dx}} \rho \mathbf{u} \cdot \mathbf{n} dA = \int_{\Delta \Omega} S_m dV \quad (4.9)$$

On the other hand, the mean velocities on the surfaces  $A_x$  and  $A_{x+dx}$  are:

$$-u_x = \frac{1}{A} \int_{A_x} \mathbf{u} \cdot \mathbf{n} dA \quad (4.10)$$

$$u_{x+dx} = \frac{1}{A} \int_{A_{x+dx}} \mathbf{u} \cdot \mathbf{n} dA \quad (4.11)$$

Taking advantages of these equations and making simply mathematical manipulations one finally has the following relation of velocity component and the source/sink terms:

$$\rho \frac{\partial u_x}{\partial x} = S_m, \quad (4.12)$$

where  $u_x$  is the  $x$ -component of velocity.

Let us now consider the source/sink terms in details. The electrochemical active surface area (ECSA) is introduced as  $A_{ECSA}$  and  $a(x)$  is ECSA density per unit of volume defined as:

$$a(x) = \frac{\Delta A_{ECSA}}{\Delta \Omega} \quad (4.13)$$

Hence, taking into account that the source/sink term is the function of flow direction only (see assumption made at the beginning of this section), i.e.  $S_m = S_m(x)$  one has:

$$S_m(x) = \rho u_D \frac{\Delta A_{ECSA}}{\Delta \Omega} = \rho u_D a(x), \quad (4.14)$$

where  $u_D$  is Darcy velocity may be defined by Darcy's law as follow:

$$u_D = -\frac{k}{\mu} \nabla p, \quad (4.15)$$

where  $k$  is permeability,  $\mu$  dynamic viscosity and  $\nabla p$  is the pressure gradient. Combining Eq. (4.15), Eq. (4.14) and putting into Eq. (4.12) finally allow one to achieve the expression for the velocity gradient:

$$\frac{\partial u}{\partial x} = -\frac{k}{\nu} a(x) \nabla p. \quad (4.16)$$

In this point, it has to be remarked that, however, the primary quantity of interest is velocity gradient the most simulations provide the results for the flow velocity. To this end, the expression for the velocity component for two different functions of the source/sink terms, which correspond to the homogeneous (conventional way of catalyst deposition) and the exponential decay towards the membrane distributions of catalyst, has the following form:

$$\begin{aligned} u_x &= - \int \frac{k \nabla p}{\mu} a(x) dx = \\ &= \frac{k \nabla p}{\mu} \begin{cases} \alpha^{homo} l_{CL} (1 - x_{cl}); & \text{for } a(x) = \alpha^{homo} \\ (\alpha^{exp}/\beta) (\exp(-\beta l_{CL} x_{cl}) - \exp(-\beta l_{CL})); & \text{for } a(x) = \alpha^{exp} \exp(-\beta x) \end{cases} \end{aligned} \quad (4.17)$$

where  $l_{CL}$  is the length of the catalyst layer, while  $x_{cl} = x/l_{CL}$  is the dimensionless spatial coordinate across the catalyst layer, with the interface GDL/CL is located at  $x_{cl} = 0$  and the interface CL/membrane is at  $x_{cl} = 1$ .

This theoretical result allows one to have an idea of behaviour of flow field throughout the porous catalyst layer. By introducing different functions for distribution of catalyst one can achieve completely different pictures of flow field at



the region of interest. In particular, it is quite relevant for the main goal of this chapter proposing proper catalyst distribution to find optimal mass transport at the interface between catalyst layer and membrane. As can be concluded from Eq. (4.17), even although both distributions of catalyst give the same result for value of velocity at the interface region (approaches to zero as  $x_d \rightarrow 1$ ), completely different behaviours can be observed for velocity gradient which is responsible for the pulling stress to phosphoric acid in membrane. Namely, comparison of the value of velocity gradient shows significant reduction for exponential decay distribution, which allows considering it as one of the optimal distributions for decreasing this stress.

### 4.4 Conclusion

In this chapter, we investigate how a parameter of a morphological model presented in Chapter 3, namely distribution of catalyst (platinum) particles, can affect gas dynamics, electro-chemistry and consequently performance in high temperature proton exchange membrane (HT-PEM) fuel cells. In particular, we propose an optimal mass transport at the interface between the catalyst layers and the membrane and we show how this strategy can be used to mitigate the phosphoric acid loss and the crossover of reagents through membrane. The main idea behind the mitigation strategy is to design the optimal flow field through the catalyst layer by different setups of morphological parameters, like distribution of catalyst particles, clusterization and so on. Because the velocity gradient orthogonal to the interface is directly related to the pulling stress acting on the phosphoric acid inside the membrane, we force it to be equal to zero at the interface between the catalyst layer and the membrane.

## 5

# Simulation setups & results

In this chapter of thesis, we explore some catalyst layer configurations by tuning the distribution of the catalyst platinum (Pt) particles. In particular, we investigate the influence of Pt deposition inside catalyst layer on mass transport by performing both pore-scale modeling of the flow through the porous catalyst layer and macroscopic modeling of single membrane electrode assembly with different distributions of catalyst particles. The main goal is to find an optimal CL by probing different distributions of catalyst particles. The catalyst particle distribution should be optimized in order to improve the performance of the PEMFCs and also to mitigate degradation mechanisms (e.g. loss of phosphoric acid). Optimization of the catalyst layer can be achieved by proper tuning of mass transport properties of CL microstructure with regards to the transport of reactant (hydrogen, oxygen) and product gases (water, vapor). For this goal, the role of the morphological model presented in Chapter 3 (see also Ref. [16]) is essential. Noticeable, it is important from the morphological point of view, to have small platinum particles with large surface area, finely dispersed on the catalyst support surface (typically, carbon powder).

### 5.1 Three-dimensional pore-scale model of a catalyst layer

This section discusses configuration setups for performing pore-scale simulations. In order to fix ideas, let us consider two different configurations: homogeneous and exponential decay towards the polymer membrane, as illustrated in Fig. 5.1. In other words, in homogeneous distribution, the probability to find

## 5. SIMULATION SETUPS & RESULTS

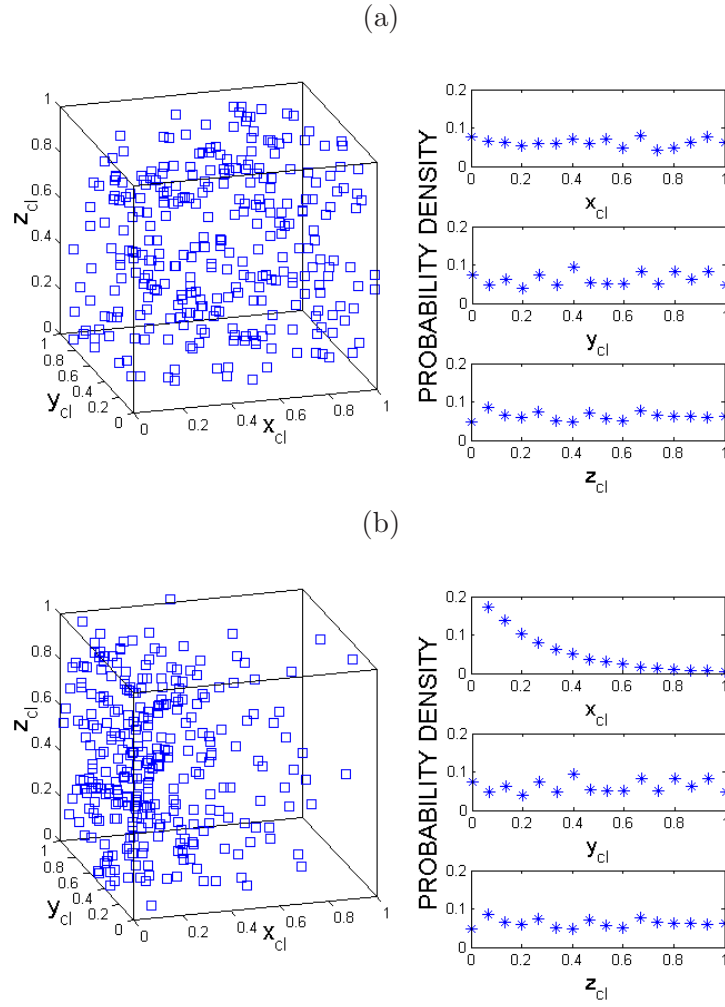


**Figure 5.1:** Left-hand side: Two representative cubic configurations of the CL with (a) homogeneous and (b) exponential decay catalyst particle distributions. Right-hand side: Probability distribution of catalyst particles along  $x, y, z$ -directions. Plots are reported in terms of the following dimensionless coordinates:  $x_{cl} = x/l_{CL}$ ,  $y_{cl} = y/l_{CL}$  and  $z_{cl} = z/l_{CL}$ .

catalyst particle is equal everywhere inside catalyst layer, while in latter case it is less probable towards the membrane. For this purpose, the morphological model of the carbon supported catalyst layer developed in Chapter 3, is adapted for these particular cases. Namely, the configuration now deals with not only complex geometry, but also catalyst deposition, comprising of the following one

dimensional array  $\mathcal{M}$ :

$$\mathcal{M}_{i_x, i_y, i_z} = \begin{cases} 0 & (i_x, i_y, i_z) \in fluid \\ 1 & (i_x, i_y, i_z) \in fluid \cap solid \\ 2 & (i_x, i_y, i_z) \in solid \\ 3 & (i_x, i_y, i_z) \in catalyst\ particles \end{cases} \quad (5.1)$$

All parameters of the porous medium, Lattice Boltzmann method used for pore-scale modeling are presented in Table 5.1.

In this study it is assumed that the catalyst particles are deposited on the surface of carbon support agglomerates. Practically, the catalyst layer has been divided into  $n_p$  number of equal parts in the  $x$ -direction, which is taken as a direction of flow towards the membrane. To obtain quasi-homogeneous distribution of catalyst particles throughout CL the same amount so-called bounce-back nodes ( $\mathcal{M}_{i_x, i_y, i_z} = 1$ ) are randomly switched on to catalyst nodes ( $\mathcal{M}_{i_x, i_y, i_z} = 3$ ) at each parts. Logically, total number of available catalyst nodes  $N_t$  is simply summation of all bounce back nodes. Distribution of interest can be obtained by varying number of catalyst particles only in  $x$ -direction, while in  $y, z$ -directions it is quasi-homogeneous, Hence, the distribution is considered as a tunable parameter of morphological model developed in Ref. [16] and huge number of virtual combinations of distribution, like Gauss, Kronecker-delta and so on, could be realized. To find a link between coefficients of two considered distributions we assume that the catalyst loading coefficient,  $\alpha^{homo}$ , in homogeneous case is given. Conservation of total number of catalyst particles yields:

$$\sum_{i=1}^{n_p} N_t \alpha^{exp} \exp(-\beta x_i) = \sum_{i=1}^{n_p} N_i^{homo} = n_p \alpha^{homo} N_t, \quad (5.2)$$

where  $\alpha^{exp}$  is the loading coefficient in exponential case and

$$\alpha^{exp} = \alpha^{homo} \frac{n_p}{\sum_{i=1}^{n_p} \exp(-\beta x_i)}. \quad (5.3)$$

To this end, the similar procedure is done to find a relation between given parameters of homogeneous distribution and desired other distributions.

As mentioned above, for simplicity,  $x$ -direction is assumed to be the direction along which the main mass transport occurs. In particular, we define  $x = 0$  as the interface between the gas diffusion and the catalyst layers, while  $x = L_{cl}$  as the

## 5. SIMULATION SETUPS & RESULTS

interface between the catalyst layer and the polymeric membrane. Homogeneous distribution can be considered as representative of conventional Pt distribution (see recent tomography data of catalyst layer presented in Ref. [33]).

**Table 5.1:** Setup of the simulations for pore-scale modeling. The parameters of Lattice Boltzmann method and the results are reported in dimensionless units (the so-called lattice units l.u., see [41])

Name	Homogeneous	Exponential decay
Model geometrical parameters		
Considered domain size, $L$	30 $\mu\text{m}$	30 $\mu\text{m}$
Average size of clusters, $L_{av}$	1.5 $\mu\text{m}$	1.5 $\mu\text{m}$
Catalyst loading coefficient, $\alpha$	0.1	0.6
Lattice Boltzmann method parameters		
Relaxation parameter, $\tau_{LB}$	1.1 l.u.	1.1 l.u.
Lattice viscosity, $\nu$	0.136364 l.u.	0.136364 l.u.
Pressure difference, $\delta p$	$3.0 \times 10^{-4}$ l.u.	$3.0 \times 10^{-4}$ l.u.
Domain size, $N$	$256 \times 256 \times 256$	$256 \times 256 \times 256$
Simulation results		
Pore-scale model		
velocity gradient	$1.859 \times 10^{-3}$ l.u.	$0.091 \times 10^{-3}$ l.u.
Macroscopic model		
velocity gradient	$1.453 \times 10^2$ [1/s]	$0.871 \times 10^2$ [1/s]

### 5.2 Three-dimensional macroscopic model of a single membrane electrode assembly

This section reports three-dimensional macroscopic model of the membrane electrode assembly (MEA). It will be used for computing flow field at catalyst layer as well as the performance, i.e. the polarization curve, for different catalyst layer configurations. The three-dimensional model of single MEA is presented in Fig. 5.2. In this model of HTPEMFC, the anode and the cathode catalyst layers are considered as made by multiple sub-layers with different Pt catalyst load inside. In order to consider a smooth profile of Pt particle distribution as has been considered in the previous section 5.1 one needs huge number of sub-layers, which is unpractical for manufacturing. For the sake of simplicity, we have considered the catalyst layer containing three separate sub-layers with different

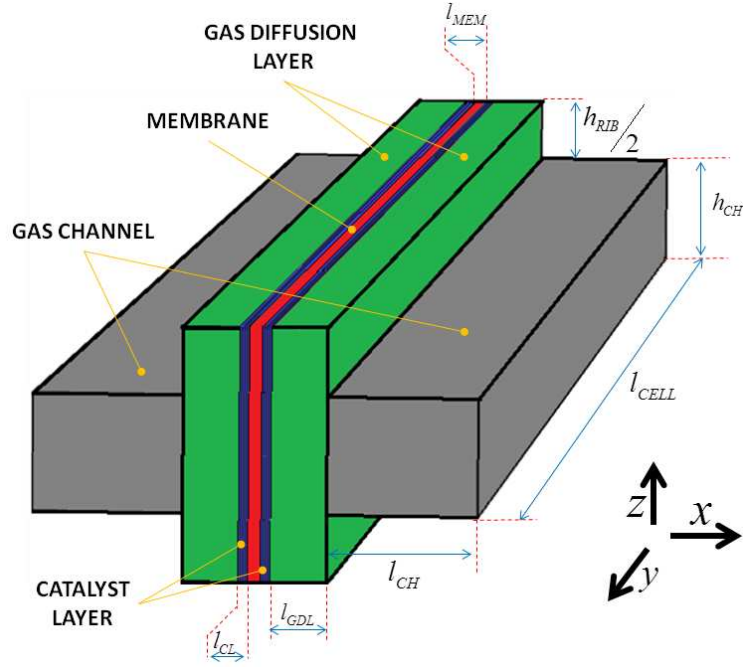


**Figure 5.2:** Single MEA geometry representations with the compartment names.

discrete value of catalyst particles load. The exact spatial dimensions of the MEA compartments can be found in Table 5.2.

**Table 5.2:** Parameters of geometry of the macroscopic model of single MEA in Fig. 5.2.

Parameter	Value	Units
Cell length, $l_{CELL}$	20.0	mm
Channel thickness, $l_{CH}$	1.0	mm
Channel height, $h_{CH}$	0.7874	mm
Rib height, $h_{RIB}$	0.90932	mm
GDL thickness, $l_{GDL}$	0.380	mm
CL thickness, $l_{CL}$	50.0	$\mu\text{m}$
Membrane thickness, $l_{MEM}$	100.0	$\mu\text{m}$

The three-dimensional, single-phase, isothermal, electrochemical-transport coupled HT-PEMFC model is considered. The following assumptions are made for this consideration:

- The fluid flow is incompressible and laminar;
- The gas mixtures obey the ideal gas law;

## 5. SIMULATION SETUPS & RESULTS

---

- Water is present on both anode and cathode sides, however it is produced only in the cathode side;
- Water exists only in the gas phase;
- The membrane is assumed to be impermeable to all gases;
- Resistance of connections between different compartments of MEA is negligible.

Thus, this model treats the steady-state transport of reactants and water in a cell in all compartments of MEA excluding membrane, while charge currents in the GDLs, the porous electrodes and the polymer membrane.

### 5.2.1 Electrochemical reactions

Hydrogen-rich fuel stream containing water is fed in to the anode channel, where part of this travels across the GDL. At the anode CL hydrogen oxidation occurs according to:



Electrons produced within this reaction migrate across the cell through following pathway: carbon support particles embedded in the anode catalyst layer, fibers of GDLs, current collector, external circuit, cathode catalyst layer. While the protons migrate shorter path, across the membrane from the anode towards the cathode catalyst layer. It should be noted here that no water molecules are assumed to be involved in the proton transport.

The local current density for the hydrogen oxidation reaction is expressed by a linearized concentration dependent Butler-Volmer expression:

$$i_a = a_\nu i_{0,a}^{ref} \left( \frac{c_{H_2}}{c_{H_2}^{ref}} \right)^{0.5} \left( \frac{\alpha_a}{RT} F \eta \right), \quad (5.5)$$

where  $i_{0,a}^{ref}$ ,  $c_{H_2}$ ,  $c_{H_2}^{ref}$  are the exchange current density, the local hydrogen and a hydrogen reference concentrations, respectively. The effective surface area,  $a_\nu$ , is defined as the ratio of the total active catalyst surface area to the total CL volume.

The cathode channels are fed by air. At the cathode, oxygen reacts together with the protons to form water according to:



A simplified concentration dependent Butler-Volmer expression, where the anodic term has been omitted, or a concentration dependent Tafel-equation is used as current density expression for the oxygen reduction reaction:

$$i_c = -a_\nu i_{0,c}^{ref} \left( \frac{c_{O_2}}{c_{O_2}^{ref}} \right) \exp \left( \frac{\alpha_c}{RT} F \eta \right), \quad (5.7)$$

where  $i_{0,a}^{ref}$ ,  $c_{O_2}$ ,  $c_{O_2}^{ref}$  are the exchange current density, the local hydrogen concentration and an oxygen reference concentrations, respectively.

### 5.2.2 Governing equations

The global mass-transport process in HTPEMFC takes place in three different media: the gas channels, gas diffusion layer, and catalyst layer. The electrolyte membrane is considered as impermeable of all gases. The corresponding equations are: the momentum-conservation equation and the continuity equation, which for reacting mixtures is extended to the chemical-species conservation equations.

The continuity equation and the incompressible Navier-Stokes equations describe momentum transport of the laminar gas flow and pressure distribution within flow channel of both the anode and cathode sides.

$$\rho \mathbf{u} \cdot \nabla \mathbf{u} = \nabla \cdot [-p\mathbf{I} + \mu(\nabla \mathbf{u} + \nabla \mathbf{u}^T)], \quad (5.8)$$

$$\nabla \cdot \mathbf{u} = 0, \quad (5.9)$$

where  $\rho$ ,  $\mathbf{u}$ ,  $p$ ,  $\mu$  are density, velocity vector, pressure, dynamical viscosity, respectively.

To describe the gas flow within GDL and CL porous media the Brinkman equations can be applied:

$$\begin{aligned} \frac{\rho}{\varepsilon} \left( \mathbf{u} \cdot \nabla \frac{\mathbf{u}}{\varepsilon} \right) = \nabla \cdot \left[ -p\mathbf{I} + \frac{\mu}{\varepsilon} (\nabla \mathbf{u} + \nabla \mathbf{u}^T) - \frac{2\mu}{3\varepsilon} (\nabla \cdot \mathbf{u}) \mathbf{I} \right] \\ - \left( \frac{\mu}{k} + \beta_r |\mathbf{u}| + S_m \right) \mathbf{u}, \end{aligned} \quad (5.10)$$



## 5. SIMULATION SETUPS & RESULTS

---

$$\rho \nabla \cdot \mathbf{u} = S_m, \quad (5.11)$$

where  $\varepsilon, k$  are two parameters of porous medium, namely porosity and permeability.

Mass source/sink term is:

$$S_m = \begin{cases} -M_{H_2} \frac{i_a}{2F}; & \text{at anode CL} \\ M_{O_2} \frac{i_c}{4F} - M_{H_2O} \frac{i_c}{2F}. & \text{at cathode CL} \end{cases} \quad (5.12)$$

The equation for the conservation of the chemical species in the channels is written using the diffusion-convection Stefan-Maxwell equations accounting hydrogen ( $H_2$ ) and water ( $H_2O$ ) species in the anode side, whereas oxygen ( $O_2$ ), water ( $H_2O$ ) and nitrogen ( $N_2$ ) species on the cathode, namely

$$\rho \mathbf{u} \cdot \nabla \omega_i = \nabla \cdot \left[ \rho \varepsilon \omega_i \sum_i D_{ik}^{eff} \left( \frac{M_t}{M_k} \nabla \omega_i + \frac{\omega_k}{p} \left( \frac{M_t}{M_k} - 1 \right) \nabla p \right) \right] + S_{\omega_i}, \quad (5.13)$$

where  $\omega$  is the mass fraction,  $M$  is the molar mass, while  $D_{ik}^{eff}$  is binary diffusion coefficient, and  $M_t$  is:

$$M_t = \left( \sum_i \frac{\omega_i}{M_i} \right)^{-1}. \quad (5.14)$$

Source terms for species have following expression:

$$S_{\omega_i} = \begin{cases} \frac{i_a}{2F}; & \text{for } H_2 \text{ at anode CL} \\ \frac{i_c}{4F}; & \text{for } O_2 \text{ at cathode CL} \\ \frac{i_c}{2F}. & \text{for } H_2O \text{ at cathode CL} \end{cases} \quad (5.15)$$

Noticeably, the Stefan-Maxwell (SM) model for diffusion is the most general approach for describing multicomponent mass transport. In contrast to Ficks model, it allows to reproduce typical diffusive effects of ternary mixtures, which are not present in binary diffusion, such as counter diffusion. In the limit of binary mixtures the Stefan-Maxwell model reduces to the Ficks model. In addition, the derivation of the Stefan-Maxwell model is thermodynamically sound, in comparison to the phenomenological formulation of Ficks equation. The Stefan-Maxwell equation can be moreover formulated to take into account the effect of external body forces, as well as to consider the effect of non-equilibrium behaviors of the fluid, such as rarefaction. Remarkably, SM model for Lattice Boltzmann method has been developed by author of this paper [72].

The transport of charges addresses in the solid and the electrolyte phases. The Poisson equations are used to evaluate transport of electrons in the solid-phase (subscript  $s$ ) within GDL and CL, while in the electrolyte-phase (subscript  $e$ ) within CL and membrane for ion transport.

$$\begin{aligned}\nabla \cdot \mathbf{i}_s &= S_\phi, & \mathbf{i}_s &= -\sigma_s \cdot \nabla \phi_s; \\ \nabla \cdot \mathbf{i}_e &= -S_\phi, & \mathbf{i}_e &= -\sigma_e \cdot \nabla \phi_e.\end{aligned}\tag{5.16}$$

Both equations are coupled through their current source/sink terms:

$$S_\phi = \begin{cases} i_a; & \text{at anode CL} \\ i_c; & \text{at cathode CL} \end{cases}\tag{5.17}$$

### 5.3 Simulation results and discussion

In this study, pore-scale flow simulations are performed based on BGK Lattice Boltzmann method using PALABOS CFD software. Two catalyst layer configurations are realized by morphological model with parameters of carbon support clusterization (agglomeration) and catalyst (Pt) deposition distribution. Namely, the catalyst layers with the same geometry (same clusterization size), but different catalyst distribution are considered. To mimic sink terms, i.e. electrochemical reaction areas, pressure boundary condition is applied at the catalyst nodes. As mentioned in Section 5.1, catalyst nodes are assumed to be deposited on the surface of carbon support agglomerates. Values of the imposed pressure ( $p$ ) are assumed as a function of the distance from the membrane:

$$p = p_0 - x_{cl} \cdot \delta p,\tag{5.18}$$

with  $p_0$  being the pressure at the inlet ( $x_{cl} = 0$ ).

In such a way, the pressure gradient is kept constant, consequently providing equal reaction probability for all catalyst particles, namely

$$\nabla p = \frac{\partial p}{\partial x} = -\delta p.\tag{5.19}$$

We will give a proof, later on, that the choice of this boundary condition is consistent with the results of macroscopic modeling. Noticeable, the laminar flow can be achieved by imposing very small value of pressure difference,  $\delta p$ .

## 5. SIMULATION SETUPS & RESULTS

---

Moreover, to take into account effect of impermeable polymeric membrane on flow field, so-called bounce-back boundary condition, which reproduce free-slip boundary condition at macroscopic level, has been applied at the bottom side of porous medium. All lateral sides are considered as periodic. In Table 5.1, the parameters of porous medium, computational domain, and LBM are reported. The LBM input parameters and results are reported in dimensionless units (the so-called lattice units  $l.u.$ , see [41]).

The module *Batteries & Fuel Cells* by COMSOL<sup>®</sup> Multiphysics software package has been utilized for performing all simulations of the macroscopic approach with the following parameters and conditions. All simulations for single MEA have been running on a Dell Workstation (24 CPU's with 64GB RAM). The convergence criteria for all species and energy calculation residuals are set to  $10^{-8}$ . Fig. 5.3 shows the mesh configuration of the considered single MEA with simple single-straight channel geometry. Table 5.3 represents the physical properties of the gases, mixture, materials of fuel cell and operating conditions. The following initial and boundary conditions have been applied in this model. At the channel inlets the mass fractions are specified, and outflow conditions are used at the channel outlets. All other external boundaries use zero flux conditions. At the flow channel inlet boundaries, laminar inlet flow velocity profiles are specified, whereas a pressure is specified at the flow channel outlet boundaries. To model a multiple parallel channel configuration, symmetry boundary conditions are applied along the long sides of the GDLs and the porous electrodes. All other wall boundaries use no-slip conditions. The mesh of the catalyst layer porous media was refined to account for the expected local quantity gradients, whereas a coarser mesh was used within gas channels and gas diffusion layers. Spatial parameters of cell is presented in Table 5.2. The total number of degrees of freedom for this problem is 111.722.

### 5.3.1 Results for flow velocity

The primary quantity of interest as a result of both pore-scale and macroscopic simulations is velocity  $\mathbf{u}$  component along fluid flow direction, owing to proportionality of pulling stress  $\tau$  acting to phosphoric acid by gases to the velocity gradient. An optimal distribution of the catalyst inside CL changes flow

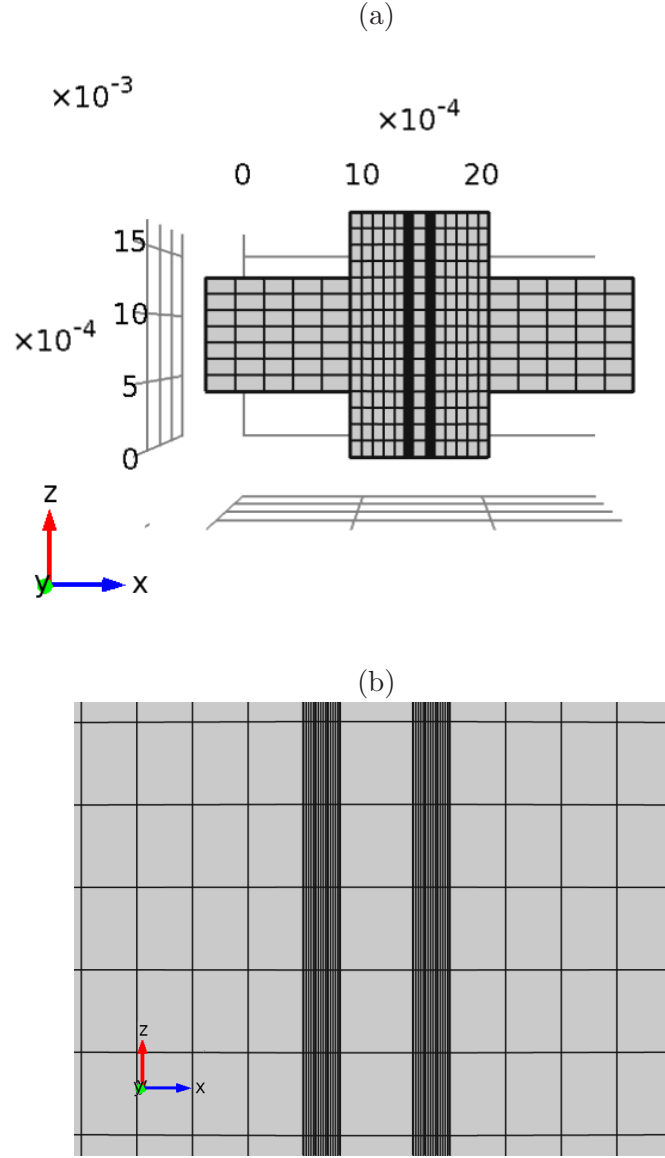


**Figure 5.3:** Mesh configuration of three-dimensional single MEA. (a) coarser mesh for the gas channels and the GDLs, while (b) finer mesh for the CLs are required.

field in such a way that not only velocity, but also its gradient is equal to zero in the interface between CL and membrane.

Let us start discussing first the results of pore-scale simulation. In Fig. 5.4 the plot of velocity along the flow direction is presented for homogeneous case of catalyst particles distribution. Red curve with '+'s represents the result of pore-

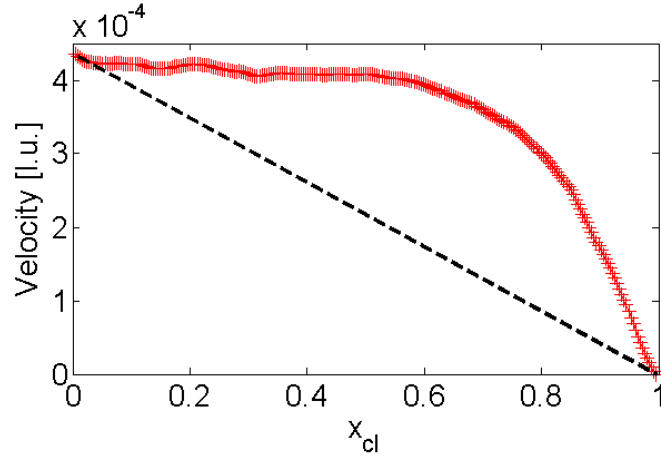


**Figure 5.4:** Profile of the  $x$ -component velocity averaged over the plane orthogonal to main flow direction ( $x$ ). Symbols represent the result of pore-scale simulations for the homogeneous catalyst particle distribution. The straight line is the theoretical prediction. The abscissa indicates the dimensionless spatial coordinate  $x_{cl} = x/l_{CL}$  across the CL, where the interface GDL/CL is located at  $x_{cl} = 0$ , while the interface CL/membrane is at  $x_{cl} = 1$ .

scale simulation, velocity component along catalyst layer averaged over orthogonal planes. As it can be seen, it considerably diverges from analytical expectation, which gives linear behaviour of velocity component, deriving from homogeneous distribution, namely

$$u_x = \frac{k \nabla p}{\mu} \alpha^{homo} l_{CL} (1 - x_{cl}) \quad (5.20)$$

The derivation of this analytical expression is presented in 4.3.3.

Several ideas to find out possible sources of the mismatching of the theoretical prediction presented in Eq. (5.20) and numerical results shown in Fig. 5.4 has been considered. It was found that the value of permeability is quite sensitive to the catalyst loading level of porous medium. Moreover, it is a function of porous medium length.

As it was established, the main reason of this kind of behavior of flow field is that catalyst particles activity highly depends on the location. Indeed, as it can be seen from Fig. 5.4 (curved line), the flow field is quasi-constant (catalyst particles is less active) at the region close to gas diffusion layer, and a sharp drop (high activity) can be observed as approaching to the membrane area. In pore-scale model, the value of difference between imposed pressure at the catalyst area

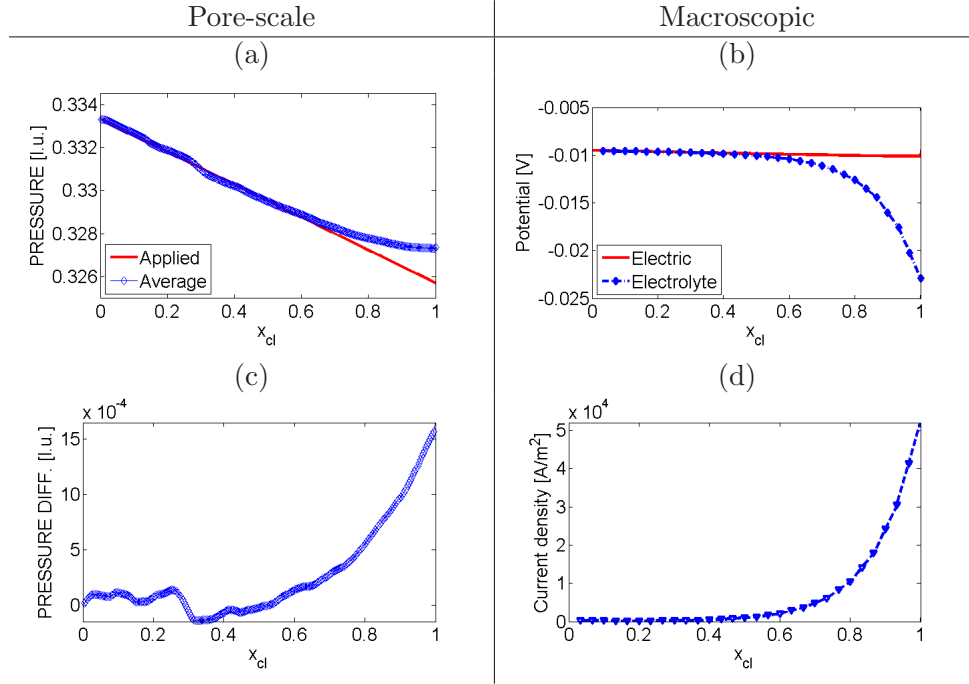


**Figure 5.5:** Left ((a) and (c)): Results of pore-scale simulations for  $\delta p = 3.0 \times 10^{-4}$  l.u. Right ((b) and (d)): Results of macroscopic model simulations with  $V_{cell} = 0.6V$ . (a): Average flow pressure (curved line) and imposed pressure at the catalyst nodes (straight line as dictated by (5.18)). (c): Difference of the above two pressures. (b): Electric and electrolyte potentials across the catalyst layer. (d): Electrode reaction current density inside the catalyst layer. Abscissas indicate the dimensionless spatial coordinate  $x_{cl} = x/l_{CL}$  across the CL, where the interface GDL/CL is located at  $x_{cl} = 0$ , while the interface CL/membrane is at  $x_{cl} = 1$ .

and average pressure of surrounding flow indicates the level of activity. To check this idea the profile of pressure averaged over orthogonal planes perpendicular to flow direction has been plotted in Fig. 5.5 (a). Curved line is result of pore-scale simulation and straight line is imposed pressure. Clearly, the value for pressure difference considerably increases at the regions close to membrane (see Fig. 5.5 (c)).

At the macroscopic level the activity of catalyst refers to reaction current density, which generally is the function of the reagent concentration,  $c$ , and the local overpotential,  $\eta$  (see Eq. (5.5)). These quantities may change with the distance. The local overpotential of the porous electrode can be defined as

$$\eta(x) = \phi_s(x) - \phi_l(x) - \Delta\phi_{ref} - E_{th}, \quad (5.21)$$

## 5. SIMULATION SETUPS & RESULTS

where  $\phi_s$  and  $\phi_e$  are the potentials in the solid and electrolyte phases, respectively, while  $\phi_{ref}$  is the potential difference across the interface for a reference electrode (it is a constant and could be set to be zero). Figure 5.5 (b) represents the curves of electric and electrolyte potentials along the line of cut plane at the center of considered MEA. Thus as lower the local overpotential  $\eta(x)$  is, larger is the current density of electrode,  $i$ , the corresponding profile of which is shown in Fig. 5.5 (d). Numerical results of macroscopic model for flow field are presented

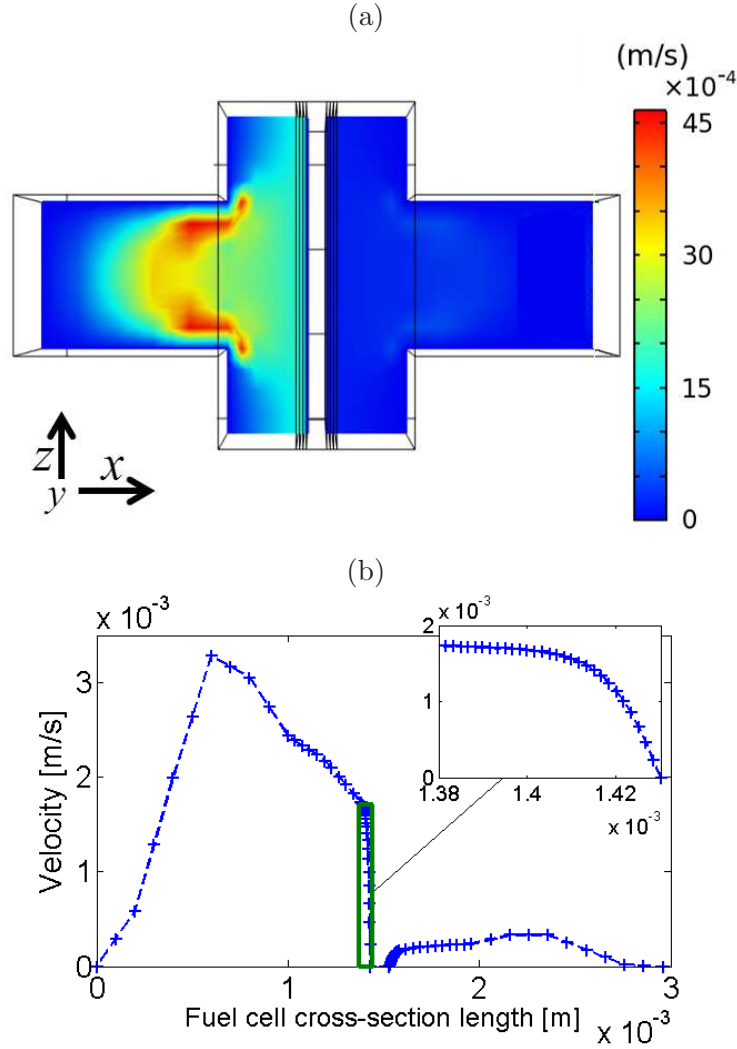


**Figure 5.6:**  $x$ -component velocity as derived by the macroscopic model at  $V_{cell} = 0.6V$  with homogeneous catalyst loading: (a) on the middle plane of the MEA ( $y = l_{CELL}/2$ ); (b) along the center line ( $z = (h_{RIB} + h_{CH})/2$ ) of the above plane. Inset: zoom of the velocity profile within the CL.

in Fig. 5.6. 2D slice of the  $x$ -component velocity (see (a)) is depicted at the orthogonal plane (MEA cross-section) cutted at the position  $y = L_{cell}/2$ , while the line graph (see (b)) is the result across the line  $z = (h_{RIB} + h_{CH})/2$  at this cut plane. In order to compare with pore-scale model inset of plot, which presents the value of velocity component in the catalyst layer is plotted.

The comparison of obtained catalyst activity curves for pore-scale and macroscopic models shows that the choice of pressure boundary condition in pore-scale simulation is feasible to mimic macroscopic reaction sides.

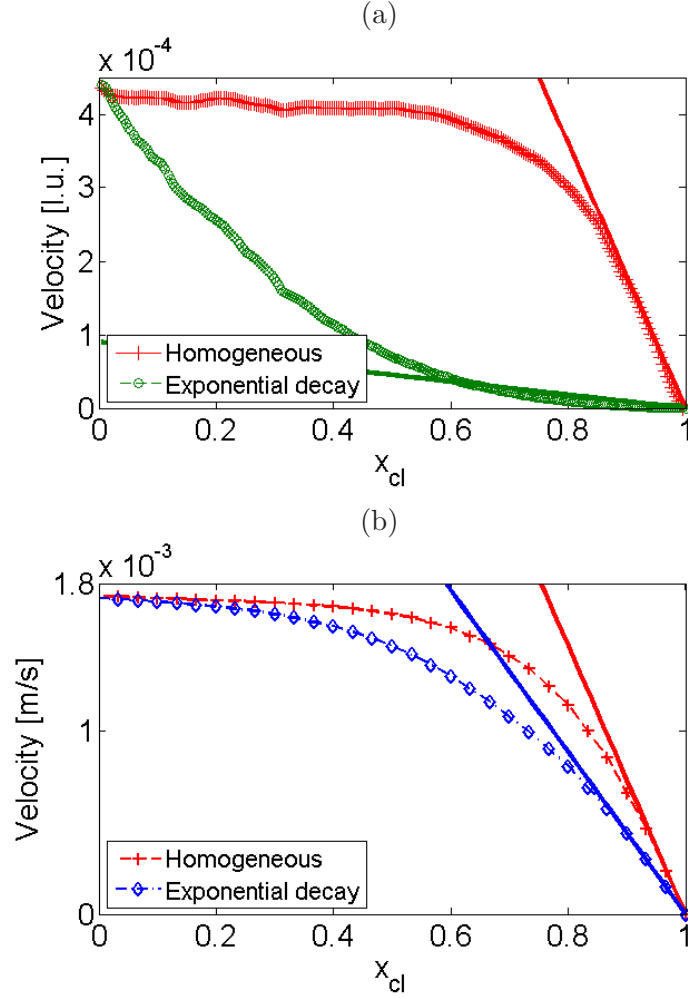


**Figure 5.7:** Velocity profiles corresponding to homogeneous and exponential decay catalyst particle distributions. (a): results of the pore-scale model with  $\delta p = 3.0 \times 10^{-4}$  l.u. (b): results of the macroscopic model with a current density  $j = 0.6 A/m^2$ . Slopes of those profiles are also reported by straight lines.



## 5. SIMULATION SETUPS & RESULTS

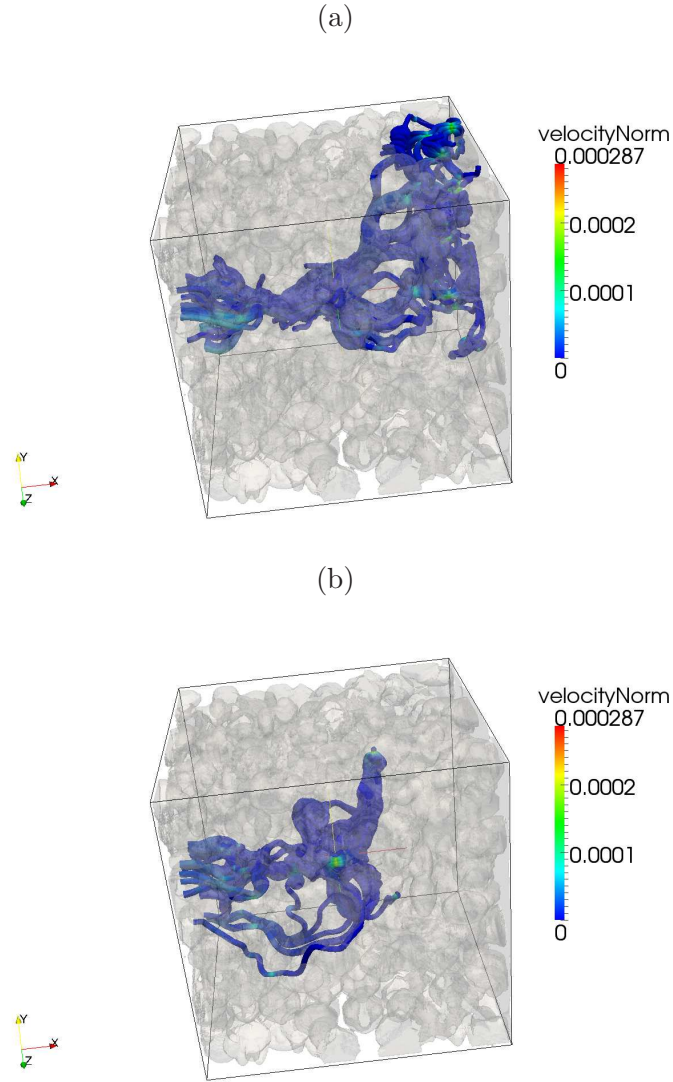
---

Fig. 5.7 shows the plots of velocity profile along catalyst layer. As can be seen, although the value of velocity (curved line) in the interface region approaches to zero in both cases of catalyst distribution, completely different behaviour of velocity gradient (straight line) can be observed. Noticeable, for homogeneous case both models give similar results for velocity field. Redistribution of catalyst from homogeneous to exponential decay distribution reduces pulling stress more than one order of magnitude, whereas approximately 67 % in pore-scale and macroscale models, respectively (see Table 5.1). Moreover, the result of pore-scale simulation for exponential decay distribution can be considered as a limit for macroscopic results due to simplified consideration of catalyst layer. Namely, as it is mentioned in Section 5.2, the catalyst layer contains with only three separate sublayers with different discrete value of catalyst particles load.

It is worth to emphasis that for the case where catalyst particles distributed with exponential decay towards membrane, the desired profile of velocity gradient has been achieved, which provides considerable reduction of fluid stress in area near membrane. Consequently, the manipulation by catalyst distribution may significantly prevent degradations with regards to PA loss and improve durability of HTPEMFC.

Additional information, how the flow field changes in case of catalyst distribution with exponential decay towards membrane can be taken from Fig. 5.8. Main flow rate changes, but also fluid flow streamlines change. This means that there are quantitative changes (scale factor), but also qualitative changes in the flow field. As it can be seen from Fig. 5.8 (a), when a homogeneous catalyst distribution is adopted in the CL, a considerable number of flow streamlines with non-negligible velocity magnitude can be observed at the CL/membrane interface. On the other hand, much fewer streamlines are able to reach the same interface when an exponential decay distribution of the catalyst is adopted in the CL. In fact, in Fig. 5.8 (b), we report the flow streamlines for the exponential decay distribution stemming from the same points as in Fig. 5.8 (a). As a result, the latter distribution ensures a significant reduction of the pulling stress on the PA contained within the polymeric membrane.

Taking into account aforementioned facts, the advantage of having exponential decay distribution of catalyst is twofold. The first is the degradations due to



**Figure 5.8:** A cubic representative configuration of the CL of a HT-PEM fuel cell is reconstructed by the method proposed in Section 3. Fluid flow streamlines through the reconstructed CL porous medium (semi-transparent) corresponding to homogeneous distribution (a) and exponential decay profile (b). Streamline colors indicate the velocity magnitude in dimensionless lattice Boltzmann units.

phosphoric acid loss and crossover of gases through membrane are mitigated. The second is owing to the enhanced flow rate the increase of the threshold for mass transport overpotential at high current density can be expected, which increases overall efficiency (peak value for performance) of fuel cell.

### 5.3.2 Single membrane electrode assembly performance simulation

Fig. 5.9 displays the simulated HTPEMFC overall performance in terms of the polarization curves at the base case operating conditions which can be found in Table 5.3. Three different cases were analyzed concerning the distribution of Pt catalyst particles inside catalyst layer both anode and cathode sides:

- (c1) homogeneous;
- (c2) exponential decay towards the polymeric membrane;
- (c3) exponential increase towards the polymeric membrane.

It should be noted that quasi-homogeneous distribution of catalyst particles used for conventional CL, while an exponential decay is thought be a case with optimal distribution to mitigate the phosphoric acid loss caused by pulling stress of reactants flow (see previous Section 5.1). In the latter case high performance is expected due to location of reaction layers very close to membrane. As it was mentioned before, for the sake of simplicity, the minimal number of discrete values of Pt catalyst loading has been taken to mimic continuous distribution, which allows to achieve only rough qualitative analysis.

The polarization curves presented in Fig. 5.9 shows typical HTPEMFC behavior. However, present consideration could not take into account one of the fundamental parts of polarization curve, mass transport overpotential in high current density region. The plot of the polarization curves can be divided into two regions. The first region corresponds to low current density region ( $j \in (0., 0.1) \text{ A/m}^2$ ), which includes a sharp voltage drop due to activation losses (kinetics). The curves show different decay slopes in the region where overpotential mainly due to Ohmic resistance, which basically consists with ionic resistance of membrane and ionomer of CL and electronic resistance of carbon support of catalyst (carbon black) and fibers of gas diffusion layer, while resistance of gas channel has been considered as negligible.

As it can be seen from Fig. 5.9 the highest decay slope was observed for the case (c2), while the smallest one for case (c3). It could be explained as follows. In the case (c2), majority of  $\text{H}^+$  ions is produced in the sublayer of CL, which is located far away from polymeric membrane. Generally,  $\text{H}^+$  ions pass much longer

**Table 5.3:** Physical parameters and operating conditions.

Parameter	Value	Units
Porous media parameters		
GDL porosity, $\varepsilon_{GDL}$	0.4	
CL porosity, $\varepsilon_{CL}$	0.3	
GDL permeability, $k_{GDL}$	$1.0 \times 10^{-11}$	$m^2$
CL permeability, $k_{CL}$	$2.0 \times 10^{-12}$	$m^2$
Fluid flow parameters		
Inlet $H_2$ mass fraction (anode), $\omega_{H_2}$	0.743	
Inlet $H_2O$ mass fraction (cathode), $\omega_{H_2O}$	0.023	
Inlet $O_2$ mass fraction (cathode), $\omega_{O_2}$	0.228	
Anode inlet flow velocity, $u_{in}^a$	0.2	m/s
Cathode inlet flow velocity, $u_{in}^c$	0.5	m/s
Anode mixture viscosity, $\mu^a$	$1.19 \times 10^{-5}$	Pa·s
Cathode mixture viscosity, $\mu^c$	$2.46 \times 10^{-5}$	Pa·s
Hydrogen molar mass, $M_{H_2}$	0.002	kg/mol
Nitrogen molar mass, $M_{N_2}$	0.028	kg/mol
Water molar mass, $M_{H_2O}$	0.018	kg/mol
Oxygen molar mass, $M_{O_2}$	0.032	kg/mol
$H_2 - H_2O$ binary diffusion coefficient	$1.81 \times 10^{-4}$	$m^2/s$
$N_2 - H_2O$ binary diffusion coefficient	$0.51 \times 10^{-4}$	$m^2/s$
$O_2 - N_2$ binary diffusion coefficient	$0.47 \times 10^{-4}$	$m^2/s$
$O_2 - H_2O$ binary diffusion coefficient	$0.55 \times 10^{-4}$	$m^2/s$
Oxygen reference concentration, $c_{O_2}^{ref}$	40.88	mol/m <sup>3</sup>
Hydrogen reference concentration, $c_{H_2}^{ref}$	40.88	mol/m <sup>3</sup>
Electric parameters		
GDL electric conductivity, $\sigma_s$	222	S/m
Membrane conductivity, $\sigma_e$	9.825	S/m
Exchange current density (anode), $i_{0,a}^{ref}$	$1.0 \times 10^5$	A/m <sup>2</sup>
Exchange current density (cathode), $i_{0,c}^{ref}$	1.0	A/m <sup>2</sup>
Operating conditions		
Cell temperature, $T$	453.15	K
Reference pressure, $P$	101	kPa
Cell voltage, $V_0$	0.9	V

pathway to reach membrane compared to other cases. Consequently, it increases average ionic resistance of CL. On the other hand, in this case, obvious decrease of electronic resistance is expected. However, owing to the fact that conductivity of carbon black is much higher than conductivity of the electrolyte,  $\sigma_s \gg \sigma_e$  (see Table 5.3), overall increase in Ohmic voltage drop can be observed. This led to

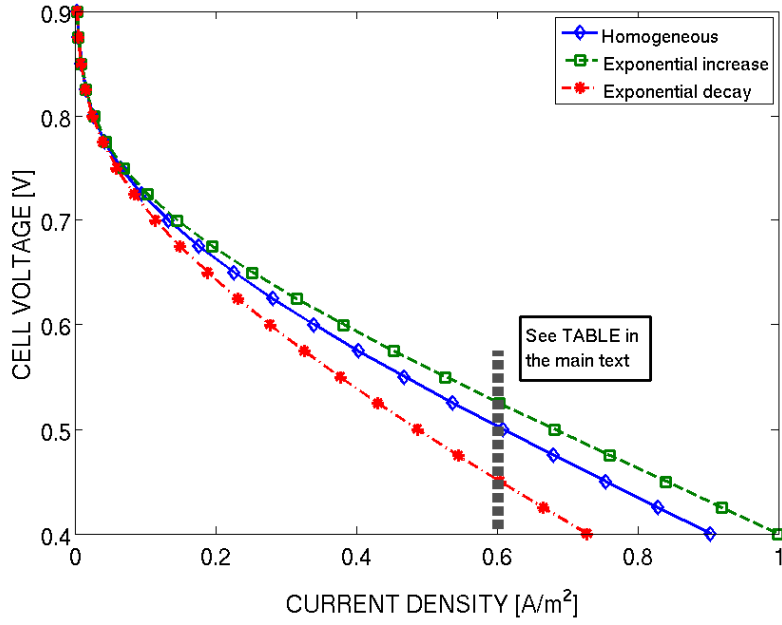


**Figure 5.9:** Polarization curves for three different configurations of catalyst particles distribution. The values of cell voltage at  $j = 0.6 \text{ A/m}^2$  current density are presented in Table 5.4.

9.3% difference in performance in high current density region in the case with exponential decay compared to homogeneous one.

Finally, it should be noted that during cell operation the dynamic change of catalyst particle distribution has been observed in real experiments [2]. Starting with quasi-homogeneous distribution of Pt catalyst for virgin fuel cell redistribution of catalyst towards membrane occurred. Namely, at the end of life-time of cell a huge amount of catalyst particles has been detected in the area near polymeric membrane. This fact justify our choice of distribution of catalyst particles inside CL of virgin HTPEMFC.

### 5.4 Conclusion

This chapter represents a final step of this thesis comprising of the setups and numerical results of both pore-scale and macroscopic simulations based on the application of the proposed mitigation design strategy in Chapter 4 to the reliable

**Table 5.4:** Results of macroscopic modeling simulation. Cell voltage at  $j = 0.6 \text{ A/m}^2$  current density for different cases of catalyst loading distribution.

Homogeneous	Exponential decay	Exponential increase
The effective surface area, $a_\nu$ for the anode catalyst sub-layers, $[1/\text{m}]$		
$1.0 \times 10^4$	$2.0 \times 10^4$	$0.27 \times 10^4$
$1.0 \times 10^4$	$0.73 \times 10^4$	$0.73 \times 10^4$
$1.0 \times 10^4$	$0.27 \times 10^4$	$2.0 \times 10^4$
The effective surface area, $a_\nu$ for cathode catalyst sub-layers, $[1/\text{m}]$		
$1.0 \times 10^4$	$2.0 \times 10^4$	$0.27 \times 10^4$
$1.0 \times 10^4$	$0.73 \times 10^4$	$0.73 \times 10^4$
$1.0 \times 10^4$	$0.27 \times 10^4$	$2.0 \times 10^4$
Cell voltage at $j = 0.6 \text{ A/m}^2$ current density, $[\text{V}]$		
0.495	0.447	0.522

morphological model developed in Chapter 3 using the numerical machinery, i.e. Lattice Boltzmann method, introduced in Chapter 2. The main outcome of the pore-scale model of the fluid flow through CL is that redistribution of catalyst from homogeneous, which is conventional catalyst distribution, to exponential decay distribution reduces pulling stress more than one order of magnitude, providing the mitigation of the fuel cell degradations with regards to phosphoric acid loss and crossover of gases through membrane. Single MEA macroscopic model shows that feasible mitigation strategy in 67% diminishes phosphoric acid loss due to pulling stress at the price of only 9.3% reduction in efficiency at high current densities.

## 5. SIMULATION SETUPS & RESULTS

---

## 6

# Conclusions & Perspectives

*‘We shall not cease from exploration,  
and the end of all our exploring will  
be to arrive where we started and  
know the place for the first time.’*

---

— T. S. Eliot

Operating PEM fuel cells at high temperature is definitively a promising technology, because of enhanced electrochemical kinetics, a simplified water management and cooling and the enhanced carbon monoxide tolerance. However the degradation phenomena of the membrane electrode assembly (MEA) represents one of the major issues that must be addressed for their commercialization and widespread use. There are two main degradation phenomena which are responsible for these issues: agglomeration of catalyst particles and phosphoric acid loss from membrane. Understanding detailed degradation phenomena will require a huge community effort.

Deep insight into understanding detailed degradation phenomena comes from multi-scale modeling. Namely, pore-scale modeling of transport mechanisms of the gases inside different compartments of fuel cell can be definitively powerful tools towards this goal. Moreover, it allows to design the mitigation strategies for specific degradation phenomenon. Pore-scale modeling has already boosted the technological development of other types of fuel cells, e.g. solid oxide fuel cells, where many contributions have been observed in recent years. Moreover, this kind of modeling techniques can take strong advantage by recent progresses in dual-beam focused ion beam scanning electron microscopy (FIB-SEM). However,



## 6. CONCLUSIONS & PERSPECTIVES

---

it must be pointed out that developing reliable morphological models is essential for interpreting the morphological data by FIB-SEM.

The first main focus of present thesis was development of reliable algorithms for reconstructing micro-morphology of HTPEM electrodes. Two fundamental regions of HTPEM electrodes, namely fiber-based (woven and non-woven) gas diffusion and carbon-supported catalyst layers are considered. The considered woven GDL is characterized by a regular micro-structure, where morphological models depend on few parameters that can be set by inspection of images obtained by scanning electron microscopy, whereas completely different micro-structure can be observed for non-woven one. On the other hand, permeability through CL is highly sensible to clusterization of carbon particles, which can be modeled by stochastic algorithms. Hence these examples are representative of two wide classes of materials, which differ for manufacturing processes and operating conditions. It is important to point out that the proposed micro-morphology techniques accurately recover the experimental values of permeability, without any special *ad-hoc* tuning. However, it must be recognized that the degree of clusterization in CL may depend on the assumptions made about the distribution of catalyst. For this reason, different catalytic distributions have been explored, in order to suggest that more realistic assumptions must be taken into account when dealing with CL, beyond standard approaches (simply based on Darcy's law).

The developed morphological model is used for investigation how distribution of catalyst inside catalyst layer of fuel cell can change flow field and how this manipulation by flow field near membrane can be used as a mitigation strategy for phosphoric acid loss and crossover of reagents through membrane. Pore-scale model of the fluid flow through CL shows that redistribution of catalyst from homogeneous, which is conventional catalyst distribution, to exponential decay distribution reduces pulling stress more than one order of magnitude. This provides twofold advantage: first, mitigation of the degradations with regards to phosphoric acid loss and crossover of gases through membrane is achieved; second, enhancement of overall fuel cell performance is expected owing to the increase of flow rate, which increases the threshold for mass transport overpotential at high current density. Single MEA macroscopic model shows that feasible mitigation

---

strategy in 67% diminishes PA loss due to pulling stress at the price of only 9.3% reduction in efficiency at high current densities.

It is worth emphasise that the proposed in this work phosphoric acid confinement strategy could allow one to increase phosphoric acid as far as materials are compatible. Furthermore, recent experimental data [2] of the dynamic change of catalyst particle distribution during cell operation, where at the end of life-time of cell a huge amount of catalyst particles has been detected in the area near polymer membrane, can justify our choice of distribution of catalyst particles inside CL for virgin HTPEMFC.

The following practical tasks are done within the scope of this thesis:

- ‡ Reliable morphological models of the electrodes, a woven and a non-woven fiber-based gas diffusion and a carbon agglomerates based catalyst layers, are developed;
- ‡ The additional tunable parameters of morphological models, like catalyst distribution, clusterization/agglomeration size, are introduced;
- ‡ Influences of the developed morphological model parameters on mass transport properties of porous electrodes are investigated;
- ‡ The main triggers of degradation phenomena for specific kind of PEMFCs are highlighted;
- ‡ An innovative idea of mitigation of specific degradation processes of PBI-based PA-doped HTPEMFC is proposed;
- ‡ Pore-scale and macroscopic models with different catalyst layer configuration setups are built;
- ‡ Feasibility of the proposed design strategy of catalyst layer is proven by performing pore-scale as well as macroscopic simulations;
- ‡ Single MEA macroscopic performance analysis is done to study the effect of mitigation strategy on the polarization curve.

## 6. CONCLUSIONS & PERSPECTIVES

---

Summarizing, this work represents a complete chain for modeling a specific degradation mechanism of HTPEMFC. It starts with collecting available micro-morphology data from the experiments. Reliable morphologic models of the electrodes, namely gas diffusion and catalyst layers, are developed based on the analysis of collected data. Challenges of finding appropriate numerical machinery/tools is also one of the important steps of this chain. This machinery is used for not only all pore-scale simulations, but also for checking feasibility and reliability of the proposed reconstruction algorithms of morphological model. Degradation phenomena are analysed in details in order to highlight the main triggers. This analysis is used for generating the mitigation ideas with final target to suggest a faithful design strategy of improving the MEA materials.

# References

- [1] J. Zhang, Z. Xie, J. Zhang, Y. Tang, C. Song, T. Navessin, Z. Shi, D. Song, H. Wang, D.P. Wilkinson, Z.-S. Liu, S. Holdcroft, High temperature PEM fuel cells, *Journal of Power Sources*, 2006, 160, 872-891 [1](#), [7](#)
- [2] Y. Oono, A. Sounai, M. Hori, Long-term cell degradation mechanism in high-temperature proton exchange membrane fuel cells, *Journal of Power Sources*, 2012, 210, 366373 [1](#), [62](#), [92](#), [97](#)
- [3] A.B. LaConti, M. Hamdan, R.C. McDonald, in: W. Vielstich, H. Gasteiger, A. Lamm (Eds.), *Handbook of Fuel Cells Fundamentals, Technology and Applications*, vol. 3, John Wiley & Sons, New York, 2003. [1](#)
- [4] M.F. Mathias, R. Makharia, H.A. Gasteiger, J.J. Conley, T.J. Fuller, C.J. Gittleman, S.S. Kocha, D.P. Miller, C.K. Mittelsteadt, T. Xie, S.G. Yan, P.T. Yu, Two fuel cell cars in every garage, *Electrochem. Soc. Interface*, 2005, 14, 2436 [1](#)
- [5] Q. Li, J.O. Jensen, R.F. Savinell, N.J. Bjerrum, High temperature proton exchange membranes based on polybenzimidazoles for fuel cells, *Prog. Polym. Sci.*, 2009, 34, 449-477 [1](#)
- [6] A.R. Korsgaard, R. Refshauge, M.P. Nielsen, M. Bang, S.K. Kær, Experimental characterization and modeling of commercial polybenzimidazole-based MEA performance, *Journal of Power Sources*, 2006, 162, 239 [1](#)
- [7] Y.-L. Ma, J.S. Wainright, M.H. Litt, R.F. Savinell, Conductivity of PBI membranes for high-temperature polymer electrolyte fuel cells, *Journal of Electrochem. Soc.*, 2004, 151, A8 [1](#)

## REFERENCES

---

- [8] J.A. Asensio, S. Borros, P.G. Romero, Enhanced Conductivity in Polyanion-Containing PBIs. Improved materials for PEM membranes and Fuel Cells, *Journal of Electrochem. Soc.*, 2004, 151, A304 [2](#)
- [9] J.R.P. Jayakody, S.H. Chung, L. Durantio, H. Zhang, L. Xiao, B.C. Benicewicz, S.G. Greenbaum, NMR Studies of Mass Transport in High-Acid-Content Fuel Cell Membranes Based on Phosphoric Acid and Polybenzimidazole, *Journal of Electrochem. Soc.*, 2007, 154, B242 [2](#)
- [10] J. Parrondo, F. Mijangos, B. Rambabu, Platinum/tin oxide/carbon cathode catalyst for high temperature PEM fuel cell, *Journal of Power Sources*, 2010, 195, 3977 [2](#)
- [11] J. Lobato, P. Cañizares, M.A. Rodrigo, F.J. Pinar, D. Ûbeda, Study of flow channel geometry using current distribution measurement in a high temperature polymer electrolyte membrane fuel cell, *Journal of Power Sources*, 2011, 196, 4209-4217 [2](#)
- [12] J. Zhang, Y. Tang, C. Song, J. Zhang, Polybenzimidazole-membrane-based PEM fuel cell in the temperature range of 120-200 °C, *Journal of Power Sources*, 2007, 172, 163-71 [2](#)
- [13] A. Sounai, K. Sakai, Proceedings of the 13th Fuel Cell FCDIC Symposium, 2006, p. 125. [2](#)
- [14] J. Baurmeister, T. Kohno, Proceedings of the 13th Fuel Cell FCDIC Symposium, 2006, p. 122. [2](#)
- [15] J. Lobato, P. Canizares, M.A. Rodrigo, J.J. Linares, D. Ubeda, F.J. Pinar, Study of the catalytic layer in polybenzimidazole-based high temperature PEMFC: Effect of platinum content on the carbon support, *Fuel Cells*, 2010, 10:2, 312-319 [4](#), [33](#), [65](#)
- [16] U. R. Salomov, E. Chiavazzo, P. Asinari, Pore-scale modeling of fluid flow through gas diffusion and catalyst layers for high temperature proton exchange membrane (HT-PEM) fuel cells, *Computers and Mathematics with Applications*, 2014, 67, 393-411 [xi](#), [xii](#), [xiii](#), [5](#), [32](#), [40](#), [41](#), [44](#), [51](#), [63](#), [73](#), [75](#)

- 
- [17] T.J. Schmidt, J. Baurmeister, Properties of high-temperature PEFC Celtec-P 1000 MEAs in start/stop operation mode, *Journal of Power Sources*, 2008, 176, 428-434 [6](#), [8](#), [58](#), [61](#)
- [18] R.A. Silva, T. Hashimoto, G.E. Thompson, C.M. Rangel, Characterization of MEA degradation for an open air cathode PEM fuel cell, *Int. J. Hydrogen Energy*, 2012, 37, 7299-7308 [7](#), [58](#)
- [19] A. Loselevich, A.A. Kornyshev, W. Lehnert, Degradation of solid oxide fuel cell anodes due to sintering of metal particles, *Journal of Electrochem. Soc.*, 1997, 144, 3010-3030 [7](#), [58](#)
- [20] S. Ma, Q. Chen, F.H. Jørgensen, P.C. Stein, E.M. Skou,  $^{19}\text{F}$  NMR studies of Nafion ionomer adsorption on PEMFC catalysts and supporting carbons, *Solid State Ion*, 2007, 178, 1568-1578 [7](#), [58](#)
- [21] T.J. Schmidt. Durability and degradation in high-temperature polymer electrolyte fuel cells, *ECS Transactions*, 2006, 1(8), 19-31 [7](#), [59](#)
- [22] S. Yu, L. Xiao, B.C. Benicewicz, Durability Studies of PBI-based High Temperature PEMFCs, *Fuel Cells*, 2008, 8, 165-174. [7](#), [59](#), [63](#)
- [23] C. Yang, S. Srinivasan, A.B. Bocarsly, S. Tulyani, J.B. Benziger, A comparison of physical properties and fuel cell performance of Nafion and zirconium phosphate/Nafion composite membranes, *J. Membr. Sci.*, 2004, 237, 145-161 [7](#)
- [24] Y.S. Kim, F. Wang, M. Hickner, T.A. Zawodzinski, J.E. McGrath, Fabrication and characterization of heteropolyacid (H<sub>3</sub>PW<sub>12</sub>O<sub>40</sub>)/directly polymerized sulfonated poly(arylene ether sulfone) copolymer composite membranes for higher temperature fuel cell applications, *Journal of Membr. Sci.*, 2003, 212, 263-282 [7](#)
- [25] F.N. Buchi, B. Gupta, O. Haas, G.G. Scherer, Study of radiation-grafted FEP-G-polystyrene membranes as polymer electrolytes in fuel cells, *Electrochim. Acta*, 1995, 40, 345-353 [7](#)

## REFERENCES

---

- [26] H. Wang, G.A. Capuano, Behavior of Raipore Radiation-Grafted Polymer Membranes in H<sub>2</sub>/O<sub>2</sub> Fuel Cells, *Journal of Electrochem. Soc.*, 1988, 145, 780-784 [7](#)
- [27] D.A. Stevens, J.R. Dahn, Thermal degradation of the support in carbon-supported platinum electrocatalysts for PEM fuel cells, *Carbon*, 2005, 43, 179-188 [7](#)
- [28] M.S. Wilson, F.H. Garzon, K.E. Sickafus, S. Gottesfeld, Surface Area Loss of Supported Platinum in Polymer Electrolyte Fuel Cells, *Journal of Electrochem. Soc.*, 1993, 140, 2872-2877 [7](#)
- [29] T. Tada, High dispersion catalysts including novel carbon supports, in: Wolf Vielstich, Hubert, A. Gasteiger, Arnold Lamm (Eds.), *Handbook of Fuel Cells - Fundamentals, Technology and Applications: Fuel Cell technology and Application*, vol. 3, John Wiley and Sons, Ltd., 2003 [7](#)
- [30] R.M. Darling, J.P. Meyers, Kinetic Model of Platinum Dissolution in PEM-FCs, *Journal of Electrochem. Soc.*, 2003, 150, A1523-A1527 [8](#)
- [31] H. Uchida, J.M. Song, S. Suzuki, E. Nakazawa, N. Baba, M. Watanabe, Electron Tomography of Nafion Ionomer Coated on Pt/Carbon Black in High Utilization Electrode for PEFCs, *Journal of Physical Chemistry B*, 2006, 110(27), 13319-13321 [9](#)
- [32] T. Ito, U. Matsuaki, Y. Otsuka, G. Katagiri, M. Kato, K. Matsubara, Y. Aoyama, H. Jinnai, Direct Three-dimensional Visualization and Morphological Analysis of Pt Particles Supported on Carbon by Transmission Electron Micro-tomography, Wiley Online Library, 2010. [9](#)
- [33] S. Thiele, T. Fürstenhaupt, D. Banham, T. Hutzenlaub, V. Birss, Ch. Ziegler, R. Zengerle, Multiscale tomography of nanoporous carbon-supported noble metal catalyst layers, *Journal of Power Sources*, 2013, 228, 185-192 [9](#), [49](#), [64](#), [76](#)
- [34] Y. Gao, X. X. Zhang, P. Rama, Y. Liu, R. Chen, H. Ostadi, K. Jiang, Modeling Fluid Flow in the Gas Diffusion Layers in PEMFC Using the Multiple

- Relaxation-time Lattice Boltzmann Method, *Fuel Cells*, 2012, 12:3, 365-381  
[9](#), [10](#), [25](#), [28](#), [47](#)
- [35] <http://www.math2market.de> [10](#)
- [36] L. Cindrella, A.M. Kannan, J.F. Lin, K. Saminathan, Y. Ho, C.W. Lin, J. Wertz, Gas diffusion layer for proton exchange membrane fuel cells: A review, *Journal of Power Sources*, 2009, 194, 146-160 [10](#)
- [37] F. J. Higuera, S. Succi, R. Benzi, Lattice Gas Dynamics with Enhanced Collisions, *EuroPhys. Lett.*, 1989, 9, 345-349 [10](#)
- [38] F. J. Higuera, J. Jimenez, Boltzmann approach to lattice gas simulations, *EuroPhys. Lett.*, 1989, 9, 663-668 [10](#)
- [39] H. Chen, S. Chen, H. W. Matthaeus, Recovery the Navier-Stokes equations using lattice gas Boltzmann method, *Phys. Rev. A*, 1992, 45, R5339-R5342  
[10](#)
- [40] Y. Qian, D. d'Humières, P. Lallemand, Lattice BGK models for Navier-Stokes equation, *Europhys.Lett.*, 1992, 17, 479-484 [10](#), [17](#)
- [41] S. Succi, The lattice Boltzmann equation for fluid dynamics and beyond, 2nd ed. Oxford University Press, New York, 2001 [xvii](#), [xviii](#), [10](#), [15](#), [18](#), [21](#), [27](#),  
[28](#), [29](#), [48](#), [50](#), [76](#), [82](#)
- [42] X. He, L. S. Luo, Theory of lattice Boltzmann method: from the Boltzmann equation to the lattice Boltzmann equation, *Phys. Rev. E*, 1997, 56, 6811-6817  
[10](#), [15](#), [17](#)
- [43] M. Sbragaglia, S. Succi, A note on the lattice Boltzmann method beyond the Chapman-Enskog limits, *Europhys. Lett.*, 2006, 73:3, 370-376 [10](#)
- [44] D. Raabe, Overview of the lattice Boltzmann method for nano- and microscale fluid dynamics in materials science and engineering, *Modelling Simul. Mater. Sci. Eng.*, 2004, 12, 77661-77665 [10](#)
- [45] T. Inamuro, T. Ogata, S. Tajima, S. Konishi, *J. Comput. Phys.*, 2004, 198, 628-644 [10](#)



## REFERENCES

---

- [46] P. Asinari, M. R. von Spakovsky, M.Q. Calí, V.B. Kasula, Direct numerical calculation of the kinematic tortuosity of reactive mixture flow in the anode layer of solid oxide fuel cells by the Lattice Boltzmann Method, *Journal Of Power Sources*, 2007, 170, 359-375 [10](#), [53](#)
- [47] P. P. Mukherjee, Q. Kang and C.-Y. Wang, Pore-scale modeling of two-phase transport in polymer electrolyte fuel cells: progress and perspective, *Energy Environ. Sci.*, 2011, 4, 346-369 [11](#)
- [48] D.F. Cheddle, N.D.H. Munroe, Three dimensional modeling of high temperature PEM fuel cells, *Journal of Power Sources*, 2006, 160, 215-223 [11](#)
- [49] P. J. Dellar, An interpretation and derivation of the lattice Boltzmann method using Strang splitting, *Computers and Mathematics with Applications*, 2013, 65, 1291-1311 [16](#)
- [50] C. Cercignani, The Boltzmann Equation and Its Applications, New York, Springer-Verlag, 1988. [16](#), [52](#)
- [51] P. Bhatnagar, E. P. Gross, and M. K. Krook, A model for collision process in gases: i. small amplitude processes in charged and neutral one-component system, *Phys. Rev*, 1954, 94, 511 [17](#)
- [52] S. Chapman and T. G. Cowling, The Mathematical Theory of Non-Uniform Gases, Cambridge University Press, 1970 [20](#)
- [53] M. Junk, A. Klar, L.-S. Luo, Asymptotic analysis of the lattice Boltzmann equation, *J. Comput. Phys.*, 2005, 210:2, 676-704 [20](#)
- [54] P. Asinari, T. Ohwada, Connection between kinetic methods for fluid-dynamic equations and macroscopic finite-difference schemes, *Computers and Mathematics with Applications*, 2009, 58, 841-861 [20](#)
- [55] Ch. Pan, L. Lou, C.T. Miller, *Computers and Fluids*, 2006, 35, 898-909 [22](#), [24](#), [28](#), [47](#)
- [56] D. P. Ziegler, (1993). Boundary conditions for the lattice Boltzmann simulations. *J. Stat. Phys.*, 1993, 71:1171 [22](#)

- 
- [57] M. Bouzidi, M. Firdaouss and P. Lallemand, Momentum transfer of a Boltzmann-lattice fluid with boundaries, *Physics of fluids*, 2001, 13:11, 3452-3459 [22](#)
- [58] T. Inamuro, M. Yoshino and F. Ogino, A nonslip boundary condition for lattice Boltzmann simulations, *Phys. Fluids*, 1995, 7, 2928-2930. [22](#)
- [59] Q. Zou and X. He, On pressure and velocity boundary conditions for the lattice Boltzmann BGK model, *Phys. Fluids*, 1997, 9, 1592-1598. [22](#)
- [60] J. Latt, Hydrodynamic limit of lattice Boltzmann equations, PhD thesis, 2007. [22](#)
- [61] <http://www.palabos.org> [24](#), [28](#)
- [62] <http://www.ansys.com> [24](#), [28](#)
- [63] G.K. Batchelor, An Introduction to Fluid Dynamics, Cambridge University press, Cambridge, 1967 [25](#), [53](#)
- [64] A.S. Sangani, A. Acrivos, Slow flow through a periodic array of spheres, *Int. J. Multiph. Flow*, 1982, 8, 343-360 [25](#), [26](#)
- [65] M.L.Stewart, A.L.Ward, D.R.Rector, A study of pore geometry effects on anisotropy in hydraulic permeability using lattice-Boltzmann method, *Advances in Water Resources*, 2006, 29, 1328-1340 [xvii](#), [25](#), [26](#), [27](#), [28](#)
- [66] H. Hasimoto, On the periodic fundamental solutions of the Stokes equations and their application to viscous flow past a cubic array of spheres, *J. Fluid Mech.*, 1959, 5, 317-328 [25](#), [26](#)
- [67] K. Yazdchi, S. Srivastava, S. Luding, Microstructural effects on the permeability of periodic fibrous porous media, *Int. J. of Multiphase Flow*, 2011, 37, 956-966 [26](#)
- [68] J. Kozeny, Ueber kapillare Leitung des Wassers im Boden, *Sitzungsber Akad. Wiss.*, Wien, 1927, 136:2a, 271-306 [26](#)

## REFERENCES

---

- [69] P.C. Carman, Fluid flow through granular beds, Transactions, Institution of Chemical Engineers, London, 1937, 15, 150-166 [26](#)
- [70] D. d'Humières. Generalized lattice Boltzmann equations, *Prog. Astronaut. Aeronaut.*, 1992, 159:450 [28](#), [47](#)
- [71] P. Asinari, Viscous coupling based lattice Boltzmann model for binary mixtures. *Phys. Fluids*, 2005, 17, 067102 [30](#)
- [72] P. Asinari, Lattice Boltzmann scheme for mixture modeling: Analysis of the continuum diffusion regimes recovering Maxwell-Stefan model and incompressible Navier-Stokes equations. *Phys. Rev. E*, 2009, 80, 056701 [30](#), [80](#)
- [73] A. Atkinson, S. Barnett, R.J. Gorte, J.T.S. Irvine, A.J. McEvoy, M. Mogenssen, S.C. Singhal, J. Vohs, Advanced anodes for high-temperature fuel cells, *Nature Materials*, 2004, 3, 17-27 [32](#)
- [74] A. Lanzini, P. Leone, P. Asinari, Microstructural characterization of solid oxide fuel cell electrodes by image analysis technique, *Journal of Power Sources*, 2009, 194, 408-422 [32](#)
- [75] C. Siegel, G. Bandlamudi, A. Heinzl, Systematic characterization of a PBI/H<sub>3</sub>PO<sub>4</sub> sol-gel membrane: Modeling and simulation, *Journal of Power Sources*, 2011, 196, 2735-2749 [33](#), [43](#)
- [76] M. Kvesic, U. Reimer, D. Froning, L. Luke, W. Lehnert, D. Stolten, 3D modeling of a 200 cm<sup>2</sup> HT-PEFC short stack, *International Journal of Hydrogen Energy*, 2012, 37, 2430-2439 [33](#), [43](#)
- [77] E. Antolini, Carbon supports for low-temperature fuel cell catalysts, *Applied Catalysis B: Environmental*, 2009, 88, 1-24 [33](#)
- [78] <http://www.freudenberg-nw.com> [34](#)
- [79] <http://www.avcarb.com/product/carbon-paper> [34](#)
- [80] D.M. Gattia, M.V. Antisari, L. Giorgi, R. Marazzi, E. Piscopiello, A. Montone, S. Bellitto, S. Licoccia, E. Traversa, Study of different nanostructured

- carbon supports for fuel cell catalysts, *Journal of Power Sources*, 2009, 194, 243-251 [43](#), [44](#)
- [81] D. Stauffer, A. Aharony, Introduction to Percolation Theory, second ed., Taylor and Francis, London, 1994, 89-103 [45](#)
- [82] G. Wellein, T. Zeiser, G. Hager, S. Donath, On the single processor performance of simple lattice Boltzmann kernels, *Computers and Fluids*, 2006, 35, 910919 [49](#)
- [83] D. Groen, J. Hetherington, H.B. Carver, R.W. Nash, M.O. Bernabeu, P.V. Coveney, Analysing and modelling the performance of the HemeLB lattice-Boltzmann simulation environment, *Journal of Comput. Sci.*, 2013, 4, 412422 [49](#)
- [84] S. Rief, E. Glatt and A. Wiegmann: Microstructure Simulation of Virtual Woven Filter Media, Filtech, Wiesbaden, Deutschland, Vol. 1, 2009, pp 231-238. [56](#)
- [85] E. Glatt, S. Rief, A. Wiegmann, M. Knefel and E. Wegenke. Structure and pressure drop of real and virtual metal wire meshes, *Fraunhofer ITWM*, 2009, 157 [56](#)
- [86] Y. Sone, Kinetic Theory and Fluid Dynamics, second ed., Birkhäuser, Boston, 2002 [51](#), [52](#)
- [87] H. Struchtrup, Macroscopic Transport Equations for Rarefied Gas Flows: Approximation Methods in Kinetic Theory, Interaction of Mechanics and Mathematics Series, Springer, Heidelberg, 2005. [51](#)
- [88] G. Karniadakis, A. Beskok, N. Aluru, Microflows and Nanoflows: Fundamentals and Simulation, Springer, 2005. [52](#)
- [89] R.B. Bird, E. Lightfoot, Transport Phenomena, John Wiley and Sons, New York, 1960. [52](#)
- [90] E.W. Lemmon, M.O. McLinden, D.G. Friend, Thermophysical properties of fluid systems, in: P.J. Linstrom, W.G. Mallard (Eds.), NIST Chemistry WebBook, National Institute of Standards and Technology, 2003. [xvii](#), [52](#), [53](#)

## REFERENCES

---

- [91] R.J.M. De Wiest, Flow through porous media, Academic Press, New York and London, 1969. [53](#)
- [92] E.B. Arkilic, M.A. Schmidt, and K.S. Breuer, Gaseous slip flow in long microchannels, *Journal of Micromechanical Systems*, 1997, 6, 167-178 [54](#)
- [93] A.Z. Weber, Gas-Crossover and Membrane-Pinhole Effects in Polymer-Electrolyte Fuel Cells, *Journal of Electrochem. Soc.*, 2008, 155, B521-B531 [59](#)
- [94] W. Liu, K. Ruth, and G. Rusch, Membrane durability in PEM fuel cells, *Journal of New Mater. Electrochem. Syst.*, 2001, 4, 227-232 [59](#)
- [95] M. Pianca, E. Barchiesi, G. Esposto, and S. Radice, End groups in fluoropolymers, *Journal of Fluorine Chem.*, 1999, 95, 71-84 [59](#)
- [96] Q. Guo, P.N. Pintauro, H. Tang, S. O'Connor, Sulfonated and crosslinked polyphosphazene-based proton-exchange membranes, *Journal of Membrane Science*, 1999, 154, 175-81 [59](#)
- [97] S. Bose, T. Kuila, T.X.H. Nguyen, N.H. Kim, Kin-tak Lau, J.H. Lee, Polymer membranes for high temperature proton exchange membrane fuel cell: Recent advances and challenges, *Progress in Polymer Science*, 2011, 36, 813-843 [59](#)
- [98] F.N. Buchi, B. Gupta, O. Haas, G.G. Scherer, Study of radiation grafted FEP-G-polystyrene membranes as polymer electrolytes in fuel cells, *Electrochim. Acta*, 1995, 40, 345-353 [59](#)
- [99] J. Xie, D.L. Wood, D.M. Wayne, T.A. Zawodzinski, P. Atanassov, R.L. Borup, Durability of PEFCs at high humidity conditions, *Journal of Electrochem. Soc.* 152 (2005) A104-A113. [59](#)
- [100] S. Kundu, M.W. Fowler, L.C. Simon, R. Abouatallah, N. Beydokhti, Degradation analysis and modeling of reinforced catalyst coated membranes operated under OCV conditions, *Journal of Power Sources*, 2008, 183, 619-628 [59](#), [60](#)

- 
- [101] M. Aoki, H. Uchida, M. Watanabe, Decomposition Mechanism of Perfluorosulfonic Acid Electrolyte in Polymer Electrolyte Fuel Cells, *Electrochem. Commun.*, 2006, 8, 1509-1513 [59](#)
- [102] M.W. Fowler, R.F. Mann, J.C. Amphlett, B.A. Peppley, P.R. Roberge, Incorporation of voltage degradation into a generalised steady state electrochemical model for a PEM fuel cell, *Journal of Power Sources*, 2002, 106, 274-283 [59](#)
- [103] K. Teranishi, K. Kawata, S. Tsushima, S. Hirai, Degradation mechanism of PEMFC under open circuit operation, *Electrochem. Solid-State Lett.*, 2006, 9, 475-477 [60](#)
- [104] A.A. Franco, and M. Gerard, Multiscale Model of Carbon Corrosion in a PEFC: Coupling with Electrocatalysis and Impact on Performance Degradation, *Journal of Electrochem. Soc.*, 2008, 155, B367-B384 [60](#), [62](#)
- [105] K. Malek and A.A. Franco, Microstructure-Based Modeling of Aging Mechanisms in Catalyst Layers of Polymer Electrolyte Fuel Cells, *Journal of Phys. Chemistry B*, 2011, 115, 8088-8101 [60](#)
- [106] Y. Shao-Horn, W.C. Sheng, S. Chen, P.J. Ferreira, E.F. Holby, and D. Morgan, Instability of supported platinum nanoparticles in low-temperature fuel cells, *Topics in Catalysis*, 2007, 46, 285-305 [60](#)
- [107] R.M. Darling, and J.P. Meyers, Kinetic Model of Platinum Dissolution, *Journal of Electrochem. Soc.*, 2003, 150, A1523-A1527 [60](#)
- [108] H. Wendt, T. Brenscheidt, A. Fischer, Optimisation and modelling of fuel cell electrodes with emphasis upon catalyst utilization, ageing phenomena and ageing prevention, *Phil. Trans Royal Soc. Lond. A*, 1996, 354, 1-15 [60](#)
- [109] R.M. Darling, and J.P. Meyers, Mathematical Model of Platinum Movement in PEM Fuel Cells, *Journal of Electrochem. Soc.*, 2005, 152, A242-A247 [60](#)
- [110] E.F. Holby, and D. Morgan, Application of Pt Nanoparticle Dissolution and Oxidation Modeling to Understanding Degradation in PEM Fuel Cells, *J. Electrochem. Soc.*, 2012, 159, B578-B591 [61](#)

## REFERENCES

---

- [111] K. Kinoshita, J.A.S. Bett, Potentiodynamic analysis of surface oxides on carbon blacks, *Carbon*, 1973, 11, 403-411 [61](#)
- [112] P.L. Antonucci, F. Romeo, M. Minutoli, E. Alderucci, N. Giordano, Electrochemical corrosion behavior of carbon black in phosphoric acid, *Carbon*, 1988, 26, 197-203 [61](#)
- [113] P. Stonehart, D. Wheeler, in: B.E. Conway, C.G. Vayenas, R.E. White, M.E. Gamboa-Adelco (Eds.), *Modern Aspects of Electrochemistry*, vol. 38, Kluwer Academic Publishers, New York, 2005 (Chapter 4). [61](#)
- [114] A.D. Modestov, M.R. Tarasevich, V.Ya. Filimonov, N.M. Zagudaeva, Degradation of high temperature MEA with PBI- $H_3PO_4$  membrane in a life test, *Electrochimica Acta*, 2009, 54, 7121-7127 [61](#)
- [115] P. Stonehart, Carbon substrates for phosphoric acid fuel cell cathodes, *Carbon*, 1984, 22, 423-431 [61](#)
- [116] C.A. Reiser, L. Bregoli, T.W. Patterson, J.S. Yi, D. Yang, M.L. Perry, and T.D. Jarvi, A Reverse-Current Decay Mechanism for Fuel Cells, *Electrochem. Solid-State Lett.*, 2005, 8, A273 [61](#)
- [117] J.P. Meyers, and R.M. Darling, Model of Carbon Corrosion in PEM Fuel Cells, *Journal of Electrochem. Soc.*, 2006, 153, A1432-A1442 [62](#)
- [118] T. Sousa, M. Mamlouk, K. Scott, A dynamic non-isothermal model of a laboratory intermediate temperature fuel cell using PBI doped phosphoric acid membranes, *Int. J. Hydrogen Energy*, 2010, 35, 12065-12080 [63](#)

## **Declaration**

I herewith declare that this dissertation is my own work and contains nothing which is the outcome of work done in collaboration with others, except as specified in the text and Acknowledgements. This dissertation contains 135 pages, 30 figures and 14 tables. This manuscript has not previously been submitted in identical or similar form for a degree or diploma or other qualification at any other University examination board. The thesis work was conducted from June 2011 to December 2013 under the supervision of Prof. Pietro Asinari and Dr. Eliodor Chiavazzo at Politecnico di Torino.

10 April, 2014, Torino

Uktam Salomov